PhD thesis

Exploring the halo structure via near-barrier scattering on ^{208}Pb: the cases of ^{15}C and ^{17}Ne

Tesis doctoral

Explorando la estructura de halo a través de la dispersión en torno a la barrera en ^{208}Pb: los casos de ^{15}C y ^{17}Ne

Memoria para optar al grado de doctor

Presentada por:
Javier Díaz Ovejas

Dirigida por:
Olof Tengblad
María José García Borge
Ismael Martel

Facultad de Ciencias Físicas
Universidad Complutense de Madrid
◊
Instituto de Estructura de la Materia
Consejo Superior de Investigaciones Científicas

Madrid, Oct 2021

Acknowledgements

Reaching this point I can say that doing a PhD has been one the best choices I have ever taken. And when I say this I'm not thinking about the specific knowledge you earn in a given field; I'm thinking more about communication and reasoning skills, about working and cooperation capabilities, about learning to cope with tough circumstances, but way more important: about life experiences. For all this and, of course, for being by my side during the past almost five years, I have to thank many people without whom this work wouldn't have been the same.

I need to start with Olof giving me this chance after our interview in September 2016, thanks for trusting in me and encouraging me to apply for the fellowship. To María for caring about me through all this process and to Ismael, for his guidance and for providing me all-type-of-quality data, so I could see the different faces of this profession. To Kike for his amazing Geant4 code and to Angel for solving all technical issues in the lab. To Briz for so many fruitful discussions and for being the fun touch at work. Also to the Aarhus group, for their help in my early experiments.

To my *primos en "Madrid"* Elia, Juancho, Fla y Viru, for all the company in my arrival to this city and for always being the best reference for me. To my *fisiamigos*, for that special friendship we built despite distances and time. If I'm thankful to physics for anything is for having placed you in my way. To my *nucelares* Pablo y Pati, for all great times from festival to festival, and to all *gfnitos*, for all those necessary after-work beers ending up in improvised parties. To *el Riesgo & co*, for always welcoming me with open arms. To Juanjo, the best roommate one could have during a lockdown. To my *Slap!* crew, *skate* mates and *Detailors* people, for always being a source of disconnection and laughter. Definitely you all made everyday life worthwhile.

To my mother, my unconditional support, sometimes the only reason why I kept up with this til the end.

And lastly, a million thanks to Silvia, probably the person I've put up with the most this time. For all the good moments inside and outside our office. Having you close made this time way easier.

Abstract

This thesis intends to reflect the work I've performed as a PhD student during the last four years and a half at IEM-CSIC, Madrid, which is the time dedicated to the preparation, development and analysis of the IS619 and E788S experiments.

These experiments can be located in a research framework of weakly-bound light nuclei whose so-called *halo* structure manifests on their scattering dynamics at energies near the Coulomb barrier. A series of similar studies began in the early 2000s and extends to the present day, gradually reaching more exotic and heavier nuclei as facilities are able to provide better quality and wider variety of beams. Furthermore, detection systems become more sophisticated and theoretical models gain accuracy.

The IS619 experiment, proposed in mid-2016 and carried out in August 2017 at the ISOLDE facility of CERN (Geneva, Switzerland), aims to probe the structure of the neutron-rich nucleus ^{15}C through its differential elastic cross section at 4.37 MeV/u on a ^{208}Pb target. The completion of the HIE post-acceleration line of ISOLDE left a door open to perform this measurement with a ^{15}C beam, being IS619 the first experimental study of this nucleus at energies near the Coulomb barrier.

The weakly bound nucleus ^{15}C ($S_n = 1218.1(8)$ keV, $S_{2n} = 9394.5(8)$ keV) has been investigated in several experiments at higher energies. Its total interaction cross section is larger than that of the neighboring ^{14,16}C and its momentum distributions for the one-neutron breakup are

much narrower than for the rest of the isotopes in the carbon chain. These features suggest the presence of a halo configuration that would be unique, according to its spectroscopic factors, due to the almost pure $s_{1/2}$ single neutron wave function in the ground state, which could partially compensate the relatively large S_n value for a halo structure.

The E788S experiment, proposed in late 2019 and carried out in February 2020 at SPIRAL, GANIL (Caen, France), is an analogous study at the proton-rich side of the nuclear chart: with a ^{17}Ne beam at 8 MeV/u on a ^{208}Pb target and a very similar experimental setup. Despite the availability of this beam in the facility for years, it also happens to be the first experimental study of ^{17}Ne dynamics near the barrier ever.

The Borromean structure of ^{17}Ne and the difference between its single-proton and its two-proton separation energies (S_p=1469(8) keV, S_{2p}=933.1(6) keV) create a clear similarity with the ^{11}Li two-neutron halo. This fact, together with the large matter radius, which is deduced from high energy measurements of the interaction cross section, and the momentum distributions from the breakup to ^{15}O, have given evidence of a two-proton halo since long ago. However, the effects of such structure at low-energies remained untested.

A complete description of how these studies arise, are experimentally planned and carried out, and how results are obtained will be detailed throughout this thesis. Firstly, a general overview about the aspects of nuclear physics related to this research will be given in chapter one. In the second chapter, the most commonly used theories to describe direct nuclear reactions will be introduced. The third chapter will be focused on the experimental technique. Then, in the fourth chapter, the development of the Monte Carlo simulations will be presented. The analysis methods used to treat IS619 and E788S data will be described in chapters fifth and sixth respectively. The results and their theoretical interpretation will be discussed in chapter seventh. A general summary of the conclusions (in English in chapter eighth and Spanish in chapter ninth) will put an end to the present work.

Contents

1
Introduction

The atomic nucleus is a bound physical system made of protons and neutrons interacting mutually through the strong, electromagnetic and weak forces.

In physics, the dynamical study of more than two bodies interacting with each other through one force is, generally, not analytically solvable, and neither is the strong interaction. This makes thinking of an exact theory of the atomic nucleus not possible and that is why, since its discovery in 1911 by E. Rutherford, scientists have been trying to understand the behavior and features of such a complex system.

Many theoretical models have provided good approaches to describe the structure, decay and reactions occurring in vast regions of the nuclear chart but, so far, experimental observation is the only method from which we can obtain real accurate information of exotic nuclei.

Nowadays, a large part of nuclear research is carried out as a basic science with no direct applications and mainly focused on getting a better understanding of nature, which is already valuable, but only time can tell us whether society will benefit from it for other purposes, as it happened with its many medical applications or its energy production possibilities.

1.1 Halo structure

Nuclides can be organized in the so-called Segrè chart according to their number of protons (Z) and neutrons (N), as seen in Fig. 1.1. These particles are indistinctly called nucleons, and the total number of them is denoted as A.

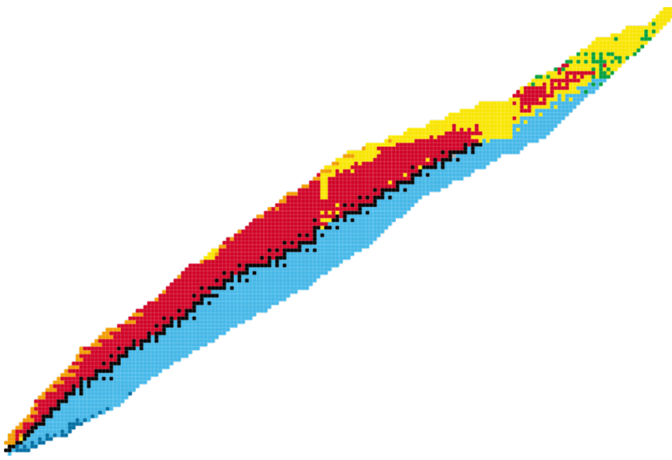

Figure 1.1: Segrè chart of nuclides. Two dimension plot with the number of protons Z in the $y-axis$ and number of neutrons N in the $x-axis$. Black squares are stable nuclei and colors depict the favored decay mode; being blue β^-, red β^+, yellow α and green spontaneous fission.

In this representation, one finds that light stable nuclei lie close to the $Z = N$ line and, for heavier elements, stability needs more and more number of neutrons. Out of the line of stability, nuclides are radioactive and decay with shorter half lives the further they are from it. Going into the proton-rich and neutron-rich zones, nuclei are said to be more exotic and the limits beyond which they are no longer bound are known as drip lines. It is close to these drip lines, in some of the most exotic nuclei with shortest half lives, where unusual phenomena, such as the halo structure, occur.

It was in 1985, at Berkeley, when accelerated radioactive ion beams could be produced in a laboratory for the first time, that the total interaction cross section for several isotope chains of light elements were measured. Their root mean square radii could then be deduced and remarkably large nuclear sizes disagreeing with the empirical $r \propto A^{1/3}$ trend (see Fig. 1.2) were found next to the neutron drip line, suggesting either strong deformations or long tails in the matter distributions [1].

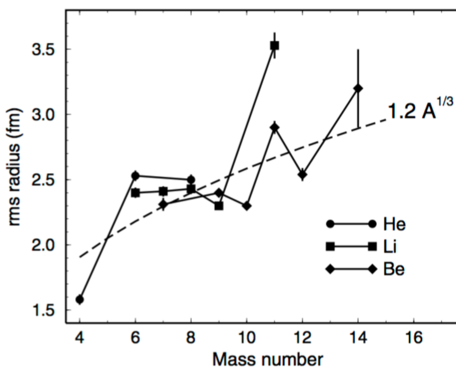

Figure 1.2: Root mean square (rms) radii of several light isotopic chains. In dashed line the empirical tendency proportional to the cube root of the mass number is plotted. The nuclear systems ^{6}He, ^{11}Li and ^{11}Be showed an anomalously large rms radii disagreeing with the empirical curve.

Two years later, in 1987, P. G. Hansen and B. Jonson gave a phenomenological explanation to understand this characteristic feature in terms of a reduced binding energy of some nucleons, leading to an enhancement of the tunneling through the nuclear potential and resulting in an exceptionally diffuse nuclear surface and extended wave functions reaching large distances [2]. The term *halo* was then coined and pictured as a compact *core* surrounded by one (or two) weakly bound valence nucleon(s) with a long-tailed wave function.

1.1.1 Momentum distributions

Shortly after the discovery of halos, in 1988, the fragmentation of these nuclei was studied at high energies (from tens of MeV/u to GeV/u) and hints of deformation in the structure were found. The transverse (referred to the beam direction) momentum distribution of the fragments produced in the reaction showed a two-gaussian shape whose widths could be directly related to the two different separation energies of the possible particles removed in the process: the ones in the core and the ones in the halo [3]. The removal of the tightly bound nucleons leads to a broad momentum distribution, while the weakly bound ones produce a narrower gaussian shape, what is interpreted as a consequence of the uncertainty principle $\Delta p \cdot \Delta x \geq \hbar/2$ together with the delocation of the halo.

Later, in 1992, the longitudinal momentum could also be measured at a lower energy ($\sim$ 100 MeV/u). Several low-Z targets were used in order to ensure that the breakup was produced by nuclear interactions and not Coulomb-induced ones, avoiding influences from electromagnetic deflection and multiple scattering that heavy targets might introduce. Furthermore, the longitudinal momentum distribution is not sensitive to diffractive broadening effects. A similar distribution consisting of two overlapped gaussians was found and an estimation of the projectile radius was calculated from the width of the narrow component [4]. Both transverse and longitudinal momentum distributions of ^{9}Li fragments from the ^{11}Li breakup are shown in Fig. 1.3.

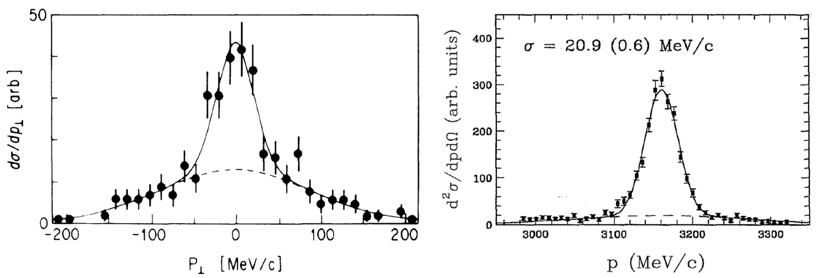

Figure 1.3: Transverse (to the left) and longitudinal (to the right) momentum distributions of ^{9}Li fragments following the ^{11}Li breakup on light targets at 0.79 GeV/u and 66 MeV/u respectively. A two-gaussian peak structure is observed in both cases. The widths of the narrow components are $\Gamma_{\perp}$=23±5 MeV/c and $\Gamma_{\|}$=20.9±0.6 MeV/c. Pictures from [3] and [4].

1.1.2 Beta decay

An alternative probe to halo states was also provided in the early 90s by beta-decay studies [5]. The usual large β-decay rate of halo nuclei is a clear advantage versus the typical low cross-sections for nuclear reactions when a low production of the exotic nucleus to study is achieved. Weak interaction is also well understood, meanwhile uncertain reaction mechanisms may lead to systematic errors. The Q-value of light exotic nuclei is up to 20 MeV feeding states in the daughter nucleus, which are often particle unbound, allowing for the detection of delayed nucleons emitted in the decay making possible correlation studies.

Beta decay probability depends on the overlap between initial and final state wavefunctions, and can bring information about nuclear halos in different ways. For ^{11}Li, its half-life indicates that the valence neutrons must occupy a mixture of the predicted p-shell but with a large contribution of the s-wave in next sd-shell [6]. Also, core and halo decay are found to decouple in some cases, such as that of ^{14}Be and its core ^{12}Be, both mostly decaying into a 1^+ state in ^{14}C and ^{12}B respectively [7]. Even decay into the continuum leaving the core unexcited may occur. For the 2n-halo paradigms ^{6}He [8] and ^{11}Li [9], the decay to the continuum freeing deuterons (βd) was predicted and measured, being another manifestation of their weakly bound structure.

1.1.3 Near-barrier scattering

The Coulomb barrier is defined as the energy due to the electrostatic repulsion that two nuclei need to exceed in order to undergo a nuclear reaction, *i.e.* reach the other nucleus surface. This, of course, depends on the atomic numbers of the two nuclei (projectile + target in a reaction) and can be then calculated as

$$V_C = \frac{1}{4\pi\epsilon_0}\frac{Z_p Z_t e^2}{r_C} \tag{1.1}$$

being $e^2/4\pi\epsilon_0$=1.44 MeV·fm and r_C the sum of the radii of the two nuclei, which is approximated by

$$r_C \simeq 1.2 \cdot \left(A_p^{1/3} + A_t^{1/3}\right) \mathrm{fm} \tag{1.2}$$

This calculation leads to a Coulomb barrier height of 4.7 MeV/u for the system ^{15}C+^{208}Pb and of 6.8 MeV/u for the system ^{17}Ne+^{208}Pb. Nonetheless, this r_C estimation is not good for halo nuclei, which precisely are characterized by a larger radius that deviates from this empirical trend.

Matter and charge distributions usually are the same for well-bound nuclei, but this is not so for halo or skin nuclei. The weak binding energy of some of the nucleons stands out differences in them and creates a dipole polarizability of the nucleus in the presence of an intense electric field. This dynamical effect arises in interactions with high-Z targets. Meanwhile the core feels certain Coulomb repulsion due to the target, the neutron halo does not (the proton halo does differently), keeping its inertia and differing from the core motion thanks to the weak binding energy. This polarization, depending on the energy of the projectile and the impact parameter of the reaction, might lead to the complete dissociation of the halo: the Coulomb breakup.

In 1997 the $B(E1)$ distribution for ^{11}Li was measured. Two years later, an evaluation of the effects of its dipole polarizability in the elastic scattering could be made [10]. This study predicted an important reduction compared to the Rutherford cross section at backward angles when the reaction energy is slightly below the Coulomb barrier. At these energies, when nuclear effects don't play an important role, the dipole polarizability of the halo nuclei strongly affects its elastic cross section. The possible Coulomb dissociation means that absorption channels are opened and the angular distribution deviates from the Rutherford trend at large angles.

1.1.3.1 Experimental antecedents

Once the dipole polarizability of halo nuclei was theoretically described and its effects in the reaction cross section below the Coulomb barrier were predicted by the end of the 90s, an experimental campaign to study nuclear halos via this method began in a collaboration between several Spanish research groups: CSIC, University of Huelva and University of Seville.

It started in November 2002, with the lightest halo case ^{6}He, as it was the most intense radioactive beam produced among the halo candidates. Its scattering on ^{208}Pb at 5 different energies above and below the Coulomb barrier ($\sim$ 20 MeV) was measured at *Centre de la Recherche du Cyclotron* in Louvaine-la-Neuve (Belgium) [11]. In this experiment, PH189, the breakup fragments were measured and theoretically described with a DWBA calculation, modeling the 2-n halo as a dineutron cluster with no inner structure but with internal energy. This experiment was improved in December 2005 (PH215) in the same facility and with the same target at one single energy of 22 MeV, using a setup with wider angular coverage, in order to get the differential elastic cross-section in the full angular range [12][13]. It was found trace of the exotic structure in the lack of a Fresnel-like interference pattern, which is typical in non-halo nuclei, as seen in Fig. 1.4.

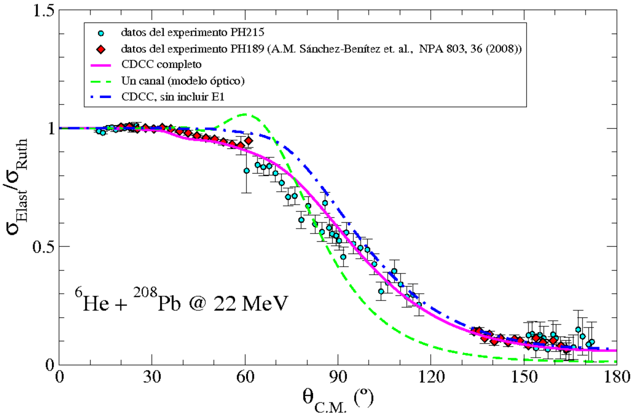

Figure 1.4: Angular distribution of the elastic cross for ^{6}He+^{208}Pb at 22 MeV measured in the PH189 and PH215 experiments plus theoretical calculations for its description. Picture from [13].

In November 2006, the ^{11}Be scattering on ^{120}Sn at 32 MeV was measured at REX-ISOLDE, CERN (Geneva, Switzerland) in the IS444 experiment [13]. Clear analogies with the ^{6}He elastic scattering above the Coulomb barrier were found in the deviation from the Rutherford cross-section. Nonetheless, the results of other reaction channels showed that the dynamics were somewhat more complicated than in the helium case, due to a competition between the direct breakup and the one-neutron transfer, channels that turned out to have comparable intensities. CDCC calculations were required, being essential a deformation in the ^{10}Be core.

In October 2008, the ^{11}Li + ^{208}Pb reaction was measured at ISAC II-TRIUMF (Vancouver, Canada). This E1104 experiment was carried out at two different energies: 24.3 MeV, i.e. below the barrier, and 29.8 MeV, i.e. above the barrier [14]. In order to determine the halo effect in ^{11}Li scattering, identical measurements with its core ^{9}Li were performed so their cross sections could be compared, minimizing the systematical errors from the potential of the ^{9}Li case. A theoretical 4-body CDCC model using nuclear and Coulomb couplings satisfactorily reproduced the differential cross section. The low-energy resonant state and a strong dipolar coupling between the ground state and the continuum were key points in reproducing the data, shown in Fig. 1.5.

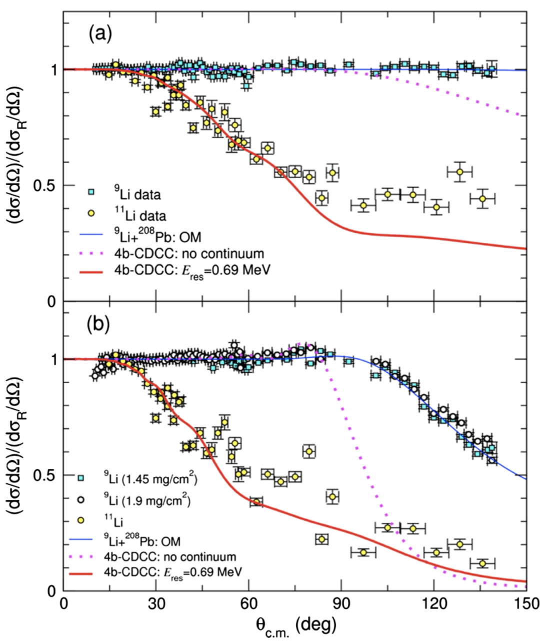

Figure 1.5: Angular distribution of the elastic cross sections for ^{9}Li (blue and white circles) and ^{11}Li (yellow circles) on ^{208}Pb at 24.3 MeV (in the top figure) and 29.8 MeV (in the bottom figure), measured in the E1104 experiment. Picture from [15].

Two years later, in 2010, the E587S experiment in GANIL (Caen, France) measured the angular distribution of the fragments produced in the ^{8}He + ^{208}Pb reaction at 16 and 22 MeV (below and above the barrier, respectively). In this case the projectile was not strictly a halo nucleus but a neutron skin one, however, its 4 loosely bound outer neutrons lead to a similar polarizability. The high beam intensity, close to 10^5-10^6 ions per second, together with the small thickness of the lead target and the optimized Global Reaction Array (GLORIA) setup, used for the first time, resulted in a very accurate elastic curve. The fact of ^{5,7}He being resonant nuclei eased the identification of the two ^{4,6}He breakup fragments. The neutron stripping reactions were modeled with DWBA and CRC calculations. A breakup description was not even attempted since there is no suitable model available [16][17].

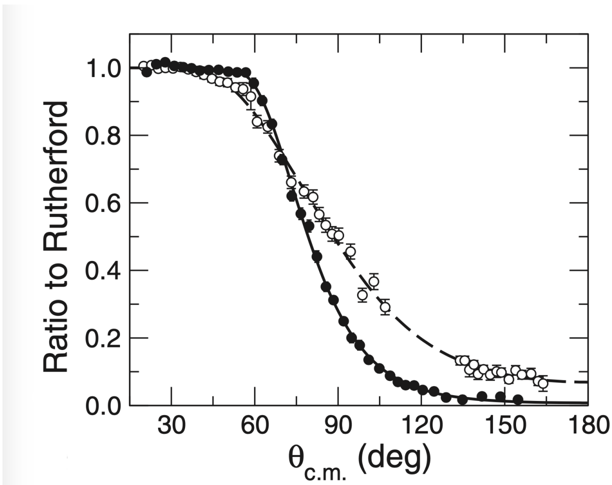

Figure 1.6: Angular distribution of the elastic cross section for ^{6}He (empty circles) and ^{8}He (filled circles) on ^{208}Pb near the Coulomb barrier. Picture from [17].

At TRIUMF, in July 2012 and June 2013, ^{11}Be+^{197}Au reaction was measured during the S1202 experiment at 31.9 MeV (below barrier) and 39.6 MeV (barrier limit). The charged particle detectors were placed inside the TIGRESS HPGe array in order to obtain information about the inelastic channel arising from the first excited state, at 320 keV, of ^{11}Be, besides the elastic (see Fig. 1.7) and breakup channels as well. XCDCC calculations, taking into account the excited structure of the core, reproduced all the measured observables [18].

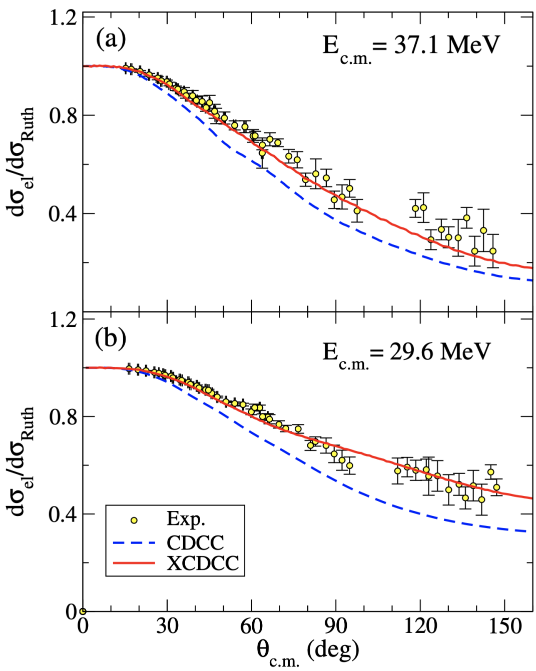

Figure 1.7: Angular distribution of the elastic cross for ^{11}Be+^{197}Au at 39.6 MeV (top figure) and 31.9 MeV (bottom figure) measured in the S1202 experiment plus theoretical calculations. Picture from [19].

The evolution of these experiments over two decades has given a tremendous push to the reaction theory challenge by the experimental results that gradually provided more and more information about nuclei structure and dynamics.

1.2 The ^{15}C nucleus

The long isotopical chain of carbon ($A = 9$ to $A = 22$) features interesting phenomena in terms of structure; from the Hoyle state of the stable ^{12}C, whose description was a milestone in the understanding of stellar evolution, to the most exotic, loosely bound and borromean configuration of ^{19,22}C. Relatively small separation energies S_n for ^{15,17,19}C of 1218.1(8), 734(18), 580(90) keV respectively, suggest halo structures, however, radii data show certain increase in ^{15,19}C but not in ^{17}C, what could be considered contradictory.

Two neutrons away from stability, ^{15}C is a neutron-rich nucleus with $J^{\pi} = 1/2^{+}$ and a 100% β^{-} decay mode of $T_{1/2} = 2.449$ s. The amount of energy available in the decay is $Q_{\beta} = 9771.7$ keV. Its first excited level, only 740 keV above the ground state, has spin and parity of $5/2^{+}$ and a half life of 2.61 ns. The separation energy for one single neutron $S_n = 1218.1(8)$ keV, somewhat large for a halo structure, significantly differs from the two neutron removal energy $S_{2n} = 9394.5(8)$ keV [20].

In 2001, the interaction cross-sections for the $^{12-20}$C chain were measured at high energies ($\sim$ GeV/A) on light targets at RIKEN [21]. The effective matter densities and rms were deduced according to Glauber-model calculations and based on the assumption of having a structure of core plus a valence neutron. This work concluded that for the ^{15}C case neither the interaction cross-section σ_I exhibits a halo structure nor the density distribution reveals a remarkable tail (it is found to be one order of magnitude less than in the case of ^{19}C, as seen in Fig. 1.8).

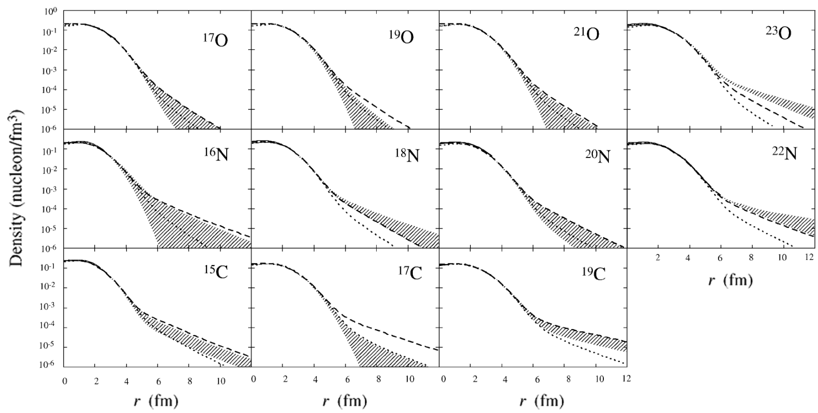

Figure 1.8: Nucleon-density distributions for some neutron-rich light nuclei, from [21]. Dashed line shows distributions deduced from a core plus a $2s_{1/2}$ valence nucleon structure and dotted line from a core plus a $1d_{5/2}$, both using the experimental S_n observed. Hatched areas reproduce the interaction cross section σ_I of every nucleus.

Shortly after, in 2004, at intermediate energies ($\sim$ 80 MeV/u) and with light carbon targets, the reaction cross sections (interaction+inelastic) for $^{14-17}$C and the longitudinal momentum distributions for their fragments after breakup were measured [22]. At these energies, the reaction cross sections are more sensitive to tail components of densities. An enhancement of the reaction cross section was seen for ^{15}C which was not observed in the previous experiments at higher energies (see Fig. 1.9). The longitudinal momenta of the ^{14}C fragments produced in the reaction also showed a remarkable narrow width (Fig. 1.10).

Thus, a halo configuration in ^{15}C was suggested for the first time. Furthermore, a dominant s-wave was required to reproduce the slightly enhanced tail of the density distribution that was observed.

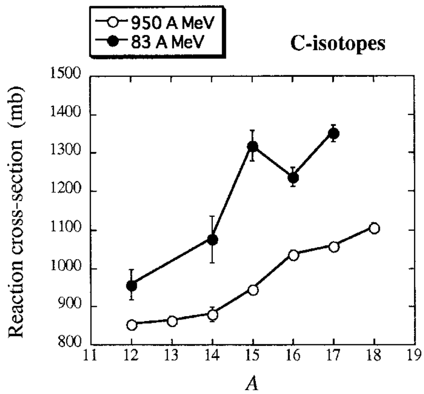

Figure 1.9: Reaction cross sections for several C isotopes at 950 MeV/u and 83 MeV/u. Picture taken from [22].

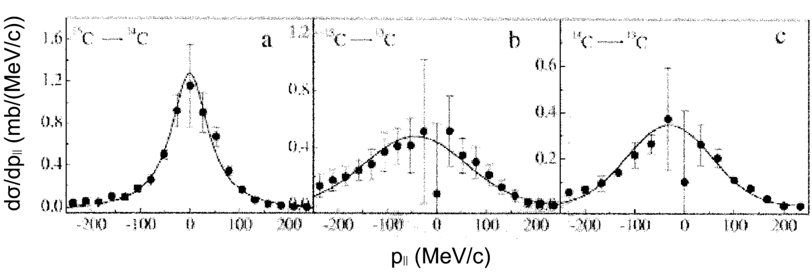

Figure 1.10: Longitudinal momentum distributions for ^{14}C from ^{15}C, ^{13}C from ^{15}C and ^{13}C from ^{14}C. Pictures taken from [22].

At the same time, spectroscopic factors were calculated for ^{15}C, supporting the idea of a halo-like $1s_{1/2}$ ground state. The partial cross sections to different final states in the reaction ^{9}Be(^{15}C,^{14}C)X at 100 MeV/u were measured. The channel to the ^{14}C (0^{+}) ground state, amounts to a quenching factor $R_s = 0.90$ [23] that approaches to unity as it usually happens with weakly bound states, in contrast to the $0.5 - 0.6$ factors typical of well-bound nuclei.

In 2007, the effects of the coupling to the one neutron transfer on the elastic scattering of weakly bound nuclei started to be studied [24], being ^{15}C considered an interesting candidate due to its almost pure $s_{1/2}$ single valence neutron. Coupled reaction channel calculations showed an important effect on the sub-barrier elastic scattering because of the coupling to this neutron stripping. Above the barrier, it is the fusion cross section the one showing important deviations caused by the coupling. These works demonstrated that the halo behaviour is due to the $s_{1/2}$ structure and not to the binding energy of the valence neutron. It is due to this contradictory interpretation manifested by reactions at different energies that we decided to test the elastic scattering of ^{15}C on ^{208}Pb at near-barrier energies, following the work already done for other halo paradigm cases such as ^{6}He, ^{11}Li and ^{11}Be.

1.3 The ^{17}Ne nucleus

On the proton-rich side of the nuclear chart, proton halos are also found, however, they occur more rarely than neutron halos and their evidence is less clear. The charge of the proton tends to create an electromagnetic repulsion between the valence nucleon(s) and the core and thus it is a more unstable structure. Nevertheless, in some situations the nuclear attraction and nucleon correlations can compensate this effect.

The ^{8}B nucleus is the lightest existing proton halo. Actually, its interaction cross section does not provide any evidence of a halo but the momentum distributions from the high energy fragmentation and its proton separation energy (S_p=140 keV) do. This is why the possible effects that the proton halo might show in the near-barrier scattering [25] and in the beta decay [26] are still being investigated nowadays. Such discrepancies in the evidences are often explained in terms of structure, being proton halos more complicated cases than the two-body model (valence nucleon plus inert core), that usually work at the neutron drip line.

The lightest bound neon isotope ^{17}Ne (J^π=1/2$^-$, $T_{1/2}$=109.2 ms), three protons away from stability, is the next case of proton halo that we find. It has a Borromean binding structure (in close parallelism with the neutron halos ^{6}He and ^{11}Li), whose single-proton separation energy S_p=1469 keV is larger than the two-proton one S_{2p}=933 keV, and no two-body subsystem (^{16}F, diproton) forms a bound state. No evidence of excited bound states has been found and it 100% decays by β^+ emission. Its matter-radius, deduced in 1994 from relativistic measurements of its interaction cross-section, led to a value of 2.75 fm, which is a 10% larger than those of the isobars ^{17}N and ^{17}F [27], and the longitudinal-momentum distribution for the two-proton breakup [28], with a $\sigma_{\parallel} = 168 \pm 17$ MeV/c, is quite narrower than the Goldhaber estimation of 290 MeV/c (see Fig. 1.11). The most satisfactory model reproducing the measured data is a ^{15}O+p+p structure, being the core coupled to two uncorrelated protons in a combination of $2s_{1/2}$ and $1d_{5/2}$ wavefunctions in the ground state.

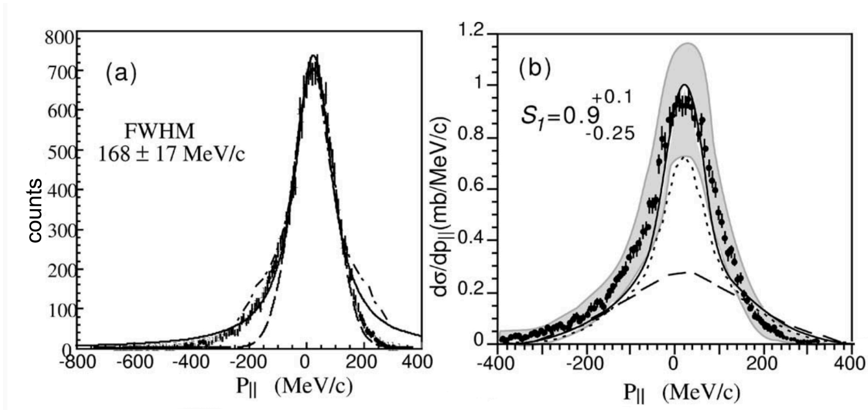

Figure 1.11: (a) Longitudinal momentum distribution from ^{17}Ne to ^{15}O with a Be target at 66 MeV/u. (b) Comparison assuming a model of ^{15}O core plus two uncorrelated protons. Solid line shows the result for a pure s-wave configuration (S_1=1) and long-dashed line for a pure d-wave configuration (S_1=0). A combination of these two extreme cases is set to reproduce the data. Picture taken from [28].

Furthermore, the strength of the first-forbidden beta decay of ^{17}Ne into the first excited state of ^{17}F needs an extent s component for the ^{17}Ne ground state [29]. All this evidence strongly suggest a halo structure for this nucleus.

2
Scattering theory

Nuclear reactions are one of the main sources of nuclear structure information. In 1909, Geiger and Marsden measured the scattering of α particles on a thin gold foil, what is considered the first nuclear reaction experiment in history. From such data, two years later, E. Rutherford could infer the modern structure of the atom as we still understand it today, with a small compact positively charged nucleus around which electrons orbit.

A nuclear reaction is the interaction between two (or more) nuclei that leads to a final state (in which they may have changed their composition), always keeping the total number of nucleons A constant as well as conserving energy and momentum. When the process from the initial to the final state occurs without the formation of an intermediate compound nucleus (i.e. typically takes $\ll 10^{-22}$ s, which is the time scale of the motion of a nucleon inside a nucleus), the reaction is said to be direct. Let's consider a beam nucleus a, with kinetic energy T_a, impinging on a heavier target nucleus A at rest (if the target is lighter than the projectile the reaction is said to be in *inverse kinematics*), then a two-body direct nuclear reaction is schematized as one of the following expressions:

$$a + A \longrightarrow b + B \tag{2.1}$$

$$A(a, b)B \tag{2.2}$$

Being b the ejectile and B the recoil, with $m_b \approx m_a$ and $m_B \approx m_A$. Each pair of nuclei with given internal states compose a reaction channel, being $a + A$ the entrance channel and $b + B$ the exit one in this generic example.

We will consider projectile and target both in their ground state, as it is the common situation when carrying out a reaction experiment at a facility. Recoil and ejectile might be left in excited states, though, and this would cause an energy excess in the exit channel, which usually denoted as Q and calculated as:

$$Q = (m_a + m_A - m_B - m_b)c^2 \tag{2.3}$$

The interactions taking part in a reaction between two nuclei are mainly two: the electromagnetic force, repulsive and long-ranged ($\sim$ Å); and the strong force, attractive, way more intense but very short-ranged ($\sim$ fm). Taking into account the features of these two forces, we can distinguish three cases depending on the energy at which the reaction occurs:

- Below the Coulomb barrier: where nuclear effects barely play a role. Nucleons can only come out through tunneling and the probability exponentially decays as we get away from the barrier. Thus, nuclei mostly exhibit electromagnetic properties, i.e. reduced transition probabilities $B(E\lambda, I_i \rightarrow I_f)$. Targets may experience collective excitations (*Coulex*) and weakly bound projectiles might suffer Coulomb breakup, but a mainly elastic scattering behavior is expected.

- Near the Coulomb barrier: Interferences between Coulomb and nuclear forces prevail, resulting in Fresnel-like patterns in the differential elastic cross-section. Electromagnetic effects still show up but more reaction channels are open as the projectile reaches the limit of the nuclear force range.

- Above the Coulomb barrier: Quantum nuclear effects dominate. Deep inelastic and Fraunhofer-like patterns due to strong diffraction behaviors are found in cross sections.

We will be dealing with scattering processes at energies near the Coulomb barrrier in the experiments of this work and, thus, the most common cases of direct reactions that we can expect are:

- Elastic scattering: The simplest reaction, where the entrance channel $a+A$ remains unchanged and, thus, $Q = 0$. It is often written as $A(a, a)A$.

- Inelastic scattering: Usually the target is left in an excited state. A part of the projectile energy goes to such excitation, so $Q = -E_x$. It is written as $A(a, a)A^*$. Sometimes, the excitation might result in the projectile or in both projectile and target, and it is also called inelastic.

- Transfer: A rearrangement of few nucleons between target and projectile occurs so $b \neq a$ and $B \neq A$. When nucleons are transferred from projectile to target we talk about *stripping* and, when are transferred from target to projectile, about *pickup*.

- Breakup: The projectile is broken up into two or more fragments when it is excited above certain emission threshold because of the electrostatic field of the target.

2.1 Reference frame

In experiments with radioactive ion beams, the reaction target is placed in a fixed position and all observations take place in a reference frame in which it is at rest. This frame is referred to as the *laboratory coordinate system (LAB)*. From a theoretical point of view, nonetheless, the motion of the center of mass of the system is of no relevance and it is then often convenient to use the reference frame where such point is at rest. It is called the *center-of-mass coordinate system (CM)* and most results are provided in this system.

Since the total linear momentum in the CM frame is always zero, the velocity $\vec{v}_{CM}$ of the center of mass is given in terms of the known laboratory bombarding velocity by the relation

$$\vec{v}_{CM} = \frac{m_a}{m_a + m_A}\vec{v}_a \tag{2.4}$$

Hence projectile and target have velocities in the center of mass frame (magnitudes in such frame will be tagged with the super index CM) of

$$\vec{v}_a^{CM} = \vec{v}_a - \vec{v}_{CM} = \frac{m_A}{m_a + m_A}\vec{v}_a \tag{2.5}$$

$$\vec{v}_A^{CM} = \vec{v}_A - \vec{v}_{CM} = -\frac{m_a}{m_a + m_A}\vec{v}_a \tag{2.6}$$

Finding the ratio between them

$$\frac{\vec{v}_a^{CM}}{\vec{v}_A^{CM}} = \frac{m_A}{m_a} \tag{2.7}$$

The initial total kinetic energy in the center of mass frame can be easily related to the laboratory bombarding energy

$$E_i^{CM} = E_a^{CM} + E_A^{CM} = \frac{m_A}{m_a + m_A} E_a \tag{2.8}$$

or equivalently, can be expressed in terms of the bombarding velocity $\vec{v}_a$ and the reduced mass μ of particles a and A

$$\frac{1}{2}\mu v_a^2 = \frac{1}{2}\frac{m_a m_A}{m_a + m_A} v_a^2 \tag{2.9}$$

After the collision, the total linear momentum in the center of mass frame remains zero, thus

$$m_b \vec{v}_b^{CM} = m_B \vec{v}_B^{CM} \tag{2.10}$$

and the final total kinetic energy hence, that must verify the energy balance $E_f^{CM} = E_i^{CM} + Q$ (or in the case of elastic scattering $Q = 0$), can be calculated as

$$E_f^{CM} = E_b^{CM} + E_B^{CM} \tag{2.11}$$

With such considerations about energy and linear momentum conservation, one can derive more or less straightforwardly any unknown quantity.

Regarding the angle transformation, one can state that the velocity of the ejectile in the center of mass frame is

$$\vec{v}_b^{CM} = \vec{v}_b - \vec{v}_{CM} \tag{2.12}$$

and split into parallel and perpendicular (to the beam direction) components

$$v_b^{CM}\cos\theta^{CM} = v_b\cos\theta - v_{CM} \tag{2.13}$$
$$v_b^{CM}\sin\theta^{CM} = v_b\sin\theta - 0 \tag{2.14}$$

From where it is derived by dividing both equations

$$\tan\theta = \frac{\sin\theta^{CM}}{\cos\theta^{CM} + \gamma} \tag{2.15}$$

being $\gamma = v_c/v_b^{CM}$, which reduces to m_a/m_A for elastic scattering, but rigorously is calculated as

$$\gamma = \sqrt{\frac{m_a m_b E_a}{m_B(m_b + m_B)Q + m_B(m_b + m_B - m_a)E_a}} \tag{2.16}$$

On the other hand, the number of reaction products found in a solid angle element $d\Omega$ centered in the θ direction (LAB) needs to coincide with the ones found in $d\Omega^{CM}$ centered in θ^{CM}, meaning

$$\left(\frac{d\sigma}{d\Omega}\right)_\theta d\Omega = \left(\frac{d\sigma}{d\Omega}\right)_{\theta^{CM}}^{CM} d\Omega' \tag{2.17}$$

and hence, if the angular distribution depends only on θ and it is isotropic in ϕ

$$\frac{(d\sigma/d\Omega)_{\theta^{CM}}^{CM}}{(d\sigma/d\Omega)_\theta} = \frac{d\Omega}{d\Omega^{CM}} = \frac{d(\cos\theta)}{d(\cos\theta^{CM})} \tag{2.18}$$

One can check from eq. 2.15 that the angle transformation can be rearranged as

$$\cos\theta = \frac{\gamma + \cos\theta^{CM}}{\sqrt{1 + \gamma^2 + 2\gamma\cos\theta^{CM}}} \tag{2.19}$$

what, with a simple derivative, directly brings the relation between solid angle elements in the two frames

$$\frac{d(\cos\theta)}{d(\cos\theta^{CM})} = \frac{1 + \gamma\cos\theta^{CM}}{(1 + \gamma^2 + 2\gamma\cos\theta^{CM})^{3/2}} \tag{2.20}$$

From eq. 2.15, one finds that very heavy targets and light projectiles lead to $\gamma \approx 0$ and hence the angle of the ejectile has almost the same value in both CM and LAB reference systems ($\theta^{CM} \approx \theta$). The same happens with the solid angle element transformation, which is very subtle. To better appreciate the above discussion, the ratio between the scattering angles and solid angles for the two reference frames is shown in Fig. 2.1 for the case of an elastic scattering ($Q = 0$) of projectiles of mass $m_a = 15$ and $m_a = 17$ on a target of mass $m_A = 208$.

Notice that, having the CM angle, the calculation of the corresponding LAB one is analytical, see expression 2.15, but the other way around needs to be computed numerically, which is the problem here since LAB scattering angles are the ones we obtain geometrically from the experimental setup. For such low γ values as in our reactions, a degree four polynomial is accurate enough to fit the relationship between CM and LAB frames and with the functions shown in Fig. 2.1 calculate any transformation. When the masses of projectile and target become comparable, the change of frame is more noticeable, thus the curves for ^{17}Ne ($m_a = 17$) exhibit greater variation with the angle than the ones for ^{15}C ($m_a = 15$).

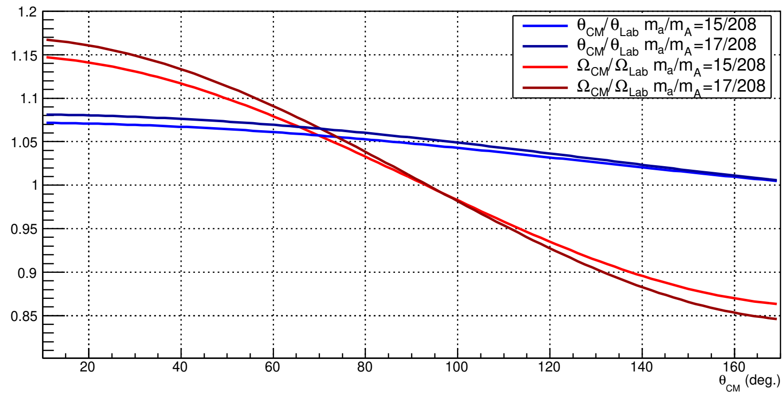

Figure 2.1: Calculated ratios between CM and LAB frames for scattering angles and solid angle elements. Cases of the elastic scattering of $m_a = 15$ and $m_a = 17$ on $m_A = 208$.

2.2 Kinematics

In non-relativistic cases, when nucleons can be treated as structureless particles (tens of MeV/u), the kinematics of a reaction can be calculated classically, imposing energy and linear momentum conservation:

$$T_a = T_B + T_b + E_B^* + E_b^* - Q \tag{2.21}$$

$$\vec{p_a} = \vec{p_B} + \vec{p_b} \tag{2.22}$$

Where E^* are the excitation energies of the recoil and ejectile and $\vec{p_i} = \sqrt{2T_i m_i}\hat{n}_i$, being $\hat{n}_i$ is the unit vector in the direction of motion.

These last two equations can be rearranged to calculate the relationship between the direction θ_b and the kinetic energy T_b of the ejectile: the so-called *kinematic curve*. In the case of elastic scattering, where entrance and exit channels are identical and no excitation occurs, it reduces to the following expression:

$$T_b^{1/2} = \frac{\sqrt{m_a m_b T_a}\cos\theta_b \pm \sqrt{m_a m_b T_a \cos^2\theta_b}}{m_b + m_B} \tag{2.23}$$

2.3 Cross section

The probability by which one particular reaction happens is described in physics by its cross section σ. This can be defined for a certain reaction channel and with respect to any of its variables, such as the outgoing direction of the ejectile or the energy at which it takes place, in its differential form. It is defined as the proportionality constant between the scattered flux in a given area dA centered in a specific direction θ and the incoming flux.

At nuclear scales, the probability of finding a particle is purely a quantum problem, described by the interaction Hamiltonian and the wavefunction of the system. This is why one needs to use the Schrödinger equation, which, in a time-independent description suitable for a nuclear reaction, reads

$$\left[\hat{T}_{\vec{r}} + H_a(\xi_a) + H_A(\xi_A) + V(\vec{r}, \xi_a, \xi_A) - E\right] \Psi(\vec{r}, \xi_a, \xi_A) = 0 \tag{2.24}$$

Where the first term is the kinetic operator of the relative motion $\vec{r}$ of the nuclei, H_a (H_A) is the internal Hamiltonian of the projectile (target) uniquely dependent on its internal coordinates and with solution $\Phi_a(\xi_a)$ [$\Phi_A(\xi_A)$], V is the interaction potential and E the energy of the system. For central potentials and with non-polarized beams it is easily demonstrated that there are no privileged directions and the reaction shows axial symmetry, with dependency on the polar (or scattering) angle θ but not with the azimuthal one φ. This means that the same physics is expected in conical surfaces with their vertexes in the target position and symmetry axes through the incoming beam direction.

The solution to the previous equation must fully describe the scattering process. Considering the physical case, the most frequent choice is an incoming plane wave which, after the interaction with the target, emits a fraction of its intensity in outgoing spherical waves. The wavefunction might suffer a strong distortion during the interaction but it vanishes asymptotically at large distances, meaning that the three remaining terms of the hamiltonian depend each one on a single variable. Therefore the wavefunction can be factorized in three parts with different individual variables ($\vec{r}$, ξ_a). The entrance channel will be tagged as α and the inelastic one as α', then the solution includes three main contributions

$$\Psi \rightarrow \Phi_\alpha(\xi_\alpha) e^{i\vec{k_\alpha}\vec{r_\alpha}} + \Phi_\alpha(\xi_\alpha) f_{\alpha\alpha}(\theta) \frac{e^{ik_\alpha r_\alpha}}{r_\alpha} + \sum_{\alpha' \neq \alpha} \Phi_{\alpha'}(\xi_\alpha) f_{\alpha'\alpha}(\theta) \frac{e^{ik_{\alpha'} r_\alpha}}{r_\alpha} \tag{2.25}$$

However, if a rearrangement of nucleons occurs and the outgoing channel has a different mass partition, tagged as β, the plane wave vanishes

$$\Psi \to \sum_{\beta\neq\alpha} \Phi_\beta(\xi_\beta) f_{\beta\alpha}(\theta) \frac{e^{ik_\beta r_\beta}}{r_\beta} \tag{2.26}$$

Where, by its definition, the amplitude of each channel is directly related to its corresponding differential cross-section [30]:

$$\frac{d\sigma_\beta}{d\Omega}(\theta) = \frac{v_\beta}{v_\alpha} |f_{\beta\alpha}(\theta)|^2 \tag{2.27}$$

The aim is, thus, to find the scattering amplitudes and subsequently the cross sections for every possible reaction channel. This task requires the complete wavefunction for any case, what is in general not solvable and requires theoretical approximations and computational methods.

2.4 Optical Model

The optical model is the simplest quantum scattering formalism [31]. It only considers elastic scattering and treats any other channel as a loss of flux from the incoming beam. Internal degrees of freedom of projectile and target are not taken into account and the effective Hamiltonian for the system depends only on the their relative coordinate.

The Hamiltonian can be separated into two terms: a real potential describing the elastic scattering and another complex one accounting for the coupling to all other channels that participate removing flux. Such potentials are usually determined phenomenologically by fitting parametrized standard analytical shapes to experimental data. The most common analytical expression is a sum of a Coulomb repulsion and a nuclear central attractive Woods-Saxon force. The Coulomb part corresponds to a uniformly distributed charge sphere with radius R_C

$$U_C(R) = \begin{cases} \frac{Z_p Z_t e^2}{2R_C}\left(3 - \frac{R^2}{R_C^2}\right) & R \leq R_C \\ \frac{Z_p Z_t e^2}{R} & R > R_C \end{cases} \tag{2.28}$$

And as nuclear part a Woods-Saxon potential describing a mean field of nucleons, as it is used in a shell model picture, with depth V_r, radius r_r and diffuseness a_r

$$U_N(R) = -\frac{V_r}{1 + e^{\frac{r_r - R}{a_r}}} \tag{2.29}$$

Since interaction with outer nucleons is easier, an imaginary surface term is usually chosen, with the shape of derivative of another Woods-Saxon potential with other different parameters W_i, r_i, a_i

$$U_S(R) = 4i\frac{d}{dR}\left(\frac{W_i}{1 + e^{\frac{r_i - R}{a_i}}}\right) \tag{2.30}$$

Additionally, as it is included in the shell model to reproduce the magic numbers, a spin-orbit coupling term is taken into account

$$U_{ls}(R) = V_{ls}\left(\frac{\hbar}{m_\pi c}\right)^2 \frac{1}{r}\frac{d}{dR}\frac{1}{1 + e^{\frac{r_{ls} - R}{a_{ls}}}}(2\vec{l} \cdot \vec{s}) \tag{2.31}$$

In this work the Optical Model will be the theoretical framework used to describe the measured elastic cross sections, as it is a first approach towards more sophisticated calculations. Nonetheless, the other common theoretical descriptions are briefly depicted in the following sections.

2.5 Coupled-channels (CC)

Including inelastic reactions, with the corresponding coupling to one or more excited states of the projectile, is a more difficult task. The coupled-channels method takes this into account by stating a Hamiltonian depending on the internal degrees of freedom ξ_a of particle a

$$H = T_\alpha(\vec{r}) + H_\alpha(\xi_\alpha) + V_\alpha(\xi_\alpha, \vec{r}) \tag{2.32}$$

With $\vec{r}$ the relative coordinate between projectile and target. The total wavefunction is then expanded in a complete set of eigenstates of the projectile

$$\Psi(R, \xi_a) = \chi_0(\vec{r})\phi_0(\xi_a) + \sum_{n>0} \chi_n(\vec{r})\phi_n(\xi_a) \tag{2.33}$$

being χ_n coefficients describing the probability at a position $\vec{r}$ of finding the projectile in the state ϕ_n. Now the Schrödinger equation for the former Hamiltonian and the developed total wavefunction can be expressed, after multiplying by ϕ_n^* and integrating over ξ_a, as the following set of differential equations

$$[E - \epsilon_n - T_{\vec{r}} - V_{nn}(\vec{r})]\, \chi_n(\vec{r}) = \sum_{n \neq n'} V_{nn'}(\vec{r}) \chi_{n'}(\vec{r}) \tag{2.34}$$

where $V_{nn'}(\vec{r})$ are the coupling potentials that cause the excitation from one state to another

$$V_{nn'}(\vec{r}) = \int d\xi_a \phi_n^*(\xi_a) V(\xi_a, \vec{r}) \phi_{n'}(\xi_a) \tag{2.35}$$

We thus obtain a set of n coupled equations, being every state coupled to all others by one of these potentials, whose solution needs to be found numerically. If the couplings are weak, the problem can be treated perturbatively with the *Distorted Wave Born Approximation*, itemizing the interaction in a potential describing the elastic scattering plus a small perturbation accounting for the excitations.

2.6 Continuum-discretized CC

When the available energy reaches the separation threshold of the exit channel and the continuum needs to be considered in the model space, the Continuum-discretized Coupled-channels (CDCC) formalism is used. Once breakup occurs, a continuum of available energies for the fragments is permitted and discretizing it within the range of distances which are relevant in the description of the reaction mechanism is the starting point of CDCC. The bins of the continuum are treated as excited states that can be coupled among them, and this is why it is considered an extension of CC method.

Considering the projectile a breaking up in the presence of a target into a core plus a valence nucleon $c + n$, an effective three-body

Hamiltonian

$$H = H_a + T_{\vec{r}} + U_{cA}(\xi_{cA}) + U_{nA}(\xi_{nA}) \tag{2.36}$$

being H_a the Hamiltonian for the projectile a and $U_{cA} + U_{nA}$ optical potentials that describe the elastic scattering of the core-target and the nucleon-target systems respectively. Each bin is completely determined by its wave number interval $[k_i, k_{i+1}]$, the angular momentum between core and nucleon $\vec{l}$, the nucleon spin $\vec{s}$ and the coupling between them $\vec{j}$. In this way, the radial part of the wavefunction of the core is a linear combination of scattering states $u_{klsj}(\vec{r})$

$$u_i(\vec{r}) = \sqrt{\left(\frac{2}{\pi N_i}\right)} \int_i^{i+1} w_i(k) u_{kl_i s j_i}(\vec{r}) dk \tag{2.37}$$

with N_i a normalization constant and w_i a weight function for every state.

The total wavefunction then is expanded in terms of eigenstates of the projectile a and the discretized continuum

$$\Psi(\vec{R}\vec{r}) = \chi_0(\vec{R})\phi_0(\vec{r}) + \sum_{i=1}^{N} \chi_i(\vec{R})\phi_i(\vec{r}) \tag{2.38}$$

giving rise to a set of coupling potentials

$$U_{ij}(\vec{R}) = \int \phi_i^*(\vec{r})[U_{cA} + U_{nA}]\phi_j(\vec{r}) \tag{2.39}$$

The result of these differential equations are the coefficients χ_i and once the total wavefunction is built the scattering amplitudes are calculated. This procedure is computed by the software `fresco` [32].

When the problem can no longer be treated as an inert three-body model, a more realistic approach can be introduced by considering collective excited states in the core, keeping the structure of the valence nucleon bound to it [33]. The states of the system are then written as a superposition of valence configurations coupled to different core states. This formalism is called XCDCC and is able to reproduce effects that cannot be explained with CDCC applied to a three-body system, such as the case of the near-barrier elastic scattering of the 1n-halo ^{11}Be [19].

3
Experimental technique

To fully perform a reaction experiment like the ones described in this work, a combination of skills and findings from different scientific fields are needed, many of which, escape the scope of this thesis. Still, an overview of the main technical topics taking part in the complete development of these experiments are given in this chapter.

The production and delivery of exotic beams, the design of the setup, the detectors used, the electronic chain to process their resulting signals and the data acquisition system will be described in order to give a complete picture of the experimental procedure.

3.1 Exotic beams production

The production of unstable nuclei and their delivery in high quality beams (small spread in energy, discrete spatial profile, good particle intensity, etc.) is one of the basis of nuclear science, where large and complex machinery is required and great efforts are dedicated.

Exotic nuclei need extreme conditions, like the ones found in stellar environments, to be produced in nature. And once produced, they quickly decay so, in order to be able to study them in a laboratory, there are two methods used at Radioactive Ion Beam facilities to artificially create them: the in-flight and the ISOL techniques. Both of them face several challenges, such as low production cross sections and very short half lives of the nuclei of interest or overwhelming amounts of undesired contaminant species.

3.1.1 The In-flight method

The In-flight separation technique is based on a heavy ion energetic primary beam impinging on a relatively thin target after which mass separators are coupled. It does not depend on chemistry factors since no diffusion is needed to extract the products from the target. It is fast since it does not require a trapping or cooling in the process and the separation already takes place at high energy. The method is thus more adapted to identify new isotopes, such superheavy elements, their masses and half lives, pushing the boundaries of the known elements. In this work I will concentrate on the second method.

3.1.2 The ISOL method

The **I**sotope **S**eparation **O**n **L**ine technique, developed in Denmark in the early 50s, is one of the most extended methods worldwide to produce radioactive ion beams and it is the one used at ISOLDE-CERN and SPIRAL-GANIL (in a mixed way) for the production of the beams used in the two experiments analyzed in this thesis work. Even though, there are some differences between the production methods at the two facilities that are discussed below.

The technique is often schematized as a production thick target, an ion source and an electromagnetic mass analyzer, all three components coupled in series, as depicted in Fig. 3.1.

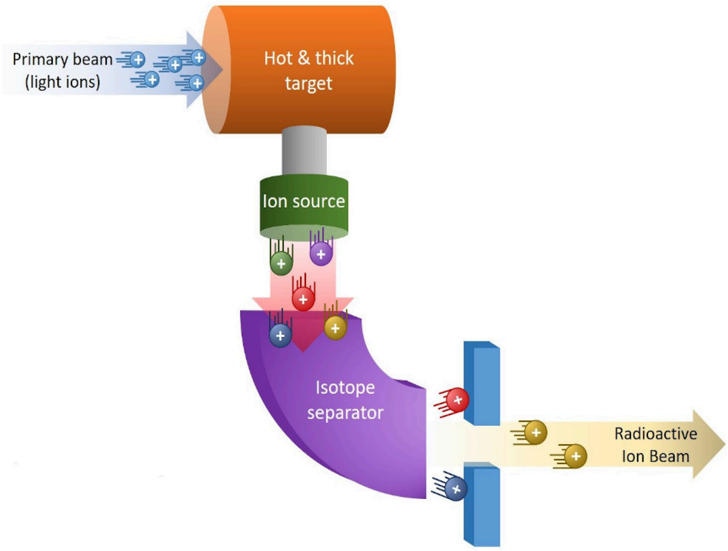

Figure 3.1: Scheme of the production of a low-energy radioactive ion beam with the ISOL method. Driver beam and target material can be different.

Firstly, a primary energetic light beam irradiates the hot and thick primary target producing by the reactions showed in Fig. 3.2 many different nuclear species. This process is accompanied by a large flux of neutrons and light charged particles emitted in a wide energy range and mainly in the forward direction. The products then diffuse out the target, which is kept at high temperature, and are transferred to an ion source, where they are ionized. When they are extracted from the source they have an energy of few tens of keV and are sent to a dipole magnet to be separated in mass. Later, the beam can be fine-focused with electromagnetic quadrupoles and post-accelerated with RF cavities if needed. Of course, all this procedure needs to be done before the nucleus of interest decays. The release from the target and the ion-source retention are the largest delay times. These are highly dependent on the chemical properties of the nucleus of interest and are done, in the best case scenarios, within few milliseconds.

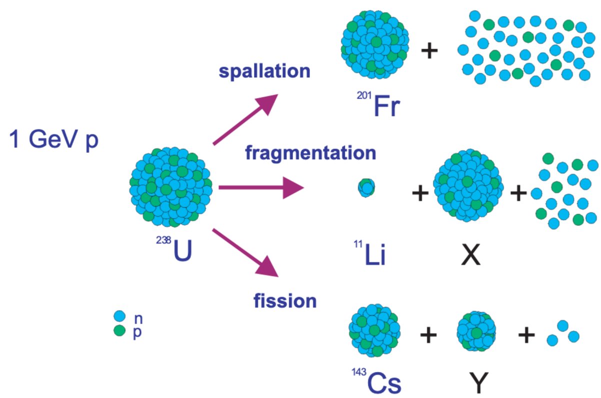

Figure 3.2: Three main reaction channels by which nuclei are produced in the ISOL method when a high energy and intensity proton beam impinges on a uranium carbide target. Target material and driver beam are not necessarily the same.

3.2 The ISOLDE facility

The **I**sotope **S**eparator **O**n **L**ine **De**vice (ISOLDE, see Fig. 3.3), located in Geneva, Switzerland, is the radioactive ion beam facility of

CERN, operating since 1967. It is possible, by the ISOL method, to produce and deliver beams of more than 1300 isotopes of different chemical elements from $Z = 2$ to $Z = 89$ with half-lives down to a few milliseconds. The interdisciplinary ISOLDE group involves radiochemistry, metallurgy, high temperature and surface physics and is constantly studying and developing different target-ion-source combinations to improve the already huge variety of beams provided. This facility consumes 60% of total CERN protons and dedicates most of its beam time to nuclear physics experiments (about 70% of it), but also to solid state physics (~20%) and fields such as biology or medicine (the remaining 10%).

1.4 GeV protons are delivered by the **P**roton **S**ynchrotron **B**ooster (PSB) in pulses every 1.2 s (or multiples) and with an intensity up to 2 μA. The protons impinge on a thick primary target that is kept at high temperature, producing a large variety of nuclei, which are fast liberated via diffusion into one of the different available ion-sources. After the ion-source extraction, the singly-charged ions are accelerated to 60 keV and sent to one of the two mass separators. The **G**eneral **P**urpose **S**eparator (GPS, used in IS619 experiment) has one bending magnet, allowing the extraction of three mass-separated beams simultaneously with a resolving power $M/\Delta M = 1000$. The High Resolution Separator (HRS), on the other hand, consists of two magnets with a slit in between and a sophisticated ion-optical system, reaching a mass resolving power of 5000, but often inducing losses in intensity [34]. The layout of this low-energy part of the facility, with the incoming driver proton beam and the two mass separators can be seen in Fig. 3.3.

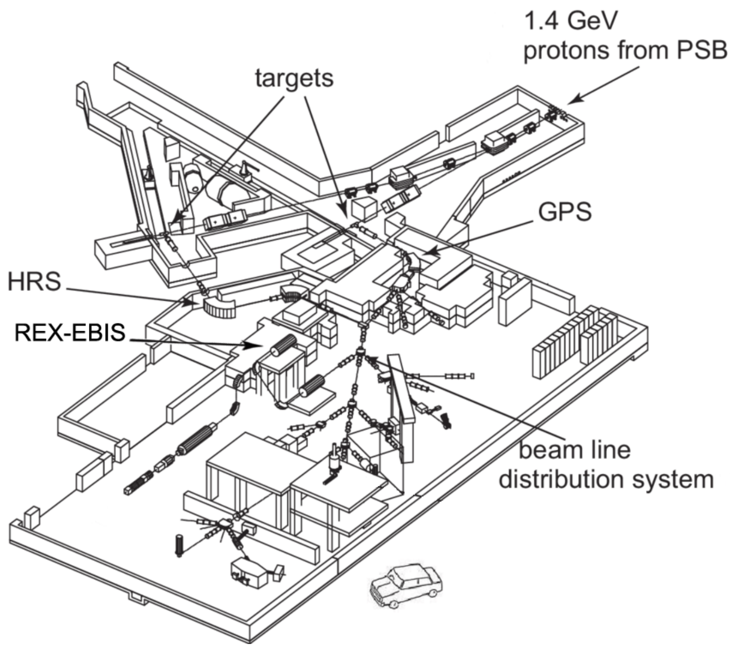

Figure 3.3: Layout of ISOLDE, with the primary targets connected to the PSB, the two mass separators (GPS and HRS) and the low-energy beam lines.

When a post-acceleration is required, the beam is injected into a Penning trap, where ions are accumulated and cooled down by buffer gas collisions. After it, an ion bunch with a typical duration of 10 μs is sent to the **E**lectron **B**eam **I**on **S**ource (EBIS). There, ions overlap with an intense electron beam to be promoted to a higher charge state in order to get a more efficient linear acceleration afterwards. Such charge breeding results in a mass-to-charge ratio A/q between 2.5 and 4.5. A first linear and room-temperature acceleration takes place in the **R**adioactive beam **Ex**periment (REX), which consists of a radiofrequency quadrupole (RFQ), an interdigital H-type structure

(IH), three seven-gap resonators and one nine-gap one. It reaches a maximum beam energy of 2.8 MeV/u.

In 2017, the **H**igh **I**ntensity and **E**nergy (HIE) part entered into operation with three cryomodules (seen in Fig. 3.5), allowing for a further energy boost. IS619 was the first physics run using this upgrade in the third post-acceleration beamline. HIE-ISOLDE consists of a superconducting linear accelerator (SC LINAC) with 20 high-β cavities cooled with helium and distributed through 4 cryo-modules, each based on five niobium-sputtered cooper quarter-wave resonators (Nb/Cu QWR) and one superconducting solenoid. At the exit of the LINAC, three beamlines (XT01, XT02 and XT03) are placed at 90°, where different experiments are allocated [35].

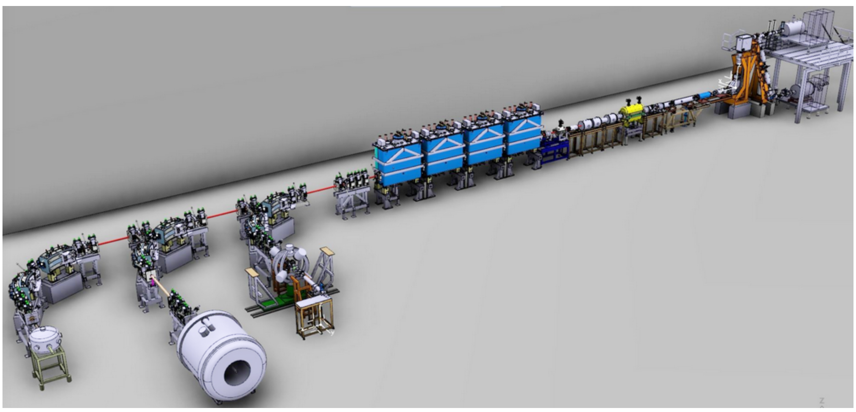

Figure 3.4: Layout of HIE-ISOLDE, with the Penning trap, the REX-EBIS, the 4 cryomodules in blue and the three beamlines XT01, XT02 and XT03 with their respective allocated experiments: Miniball, ISS and SEC. The completion of the energy upgrade with the 4 cryomodules, allowing for acceleration up to 10 MeV/u occurred in 2018.

Figure 3.5: One of the cryo-modules of HIE-ISOLDE SC LINAC with its five high-β cavities.

The **S**cattering **E**xperiment **C**hamber (SEC), seen in Fig. 3.6, is a permanent vacuum chamber coupled to the XT03 beamline of HIE-ISOLDE. It is dedicated to reaction studies where gamma detection is not required. Its versatile design, with 1 m of diameter and 50 cm of height, allows for different detector configurations inside, surrounding a reaction target. Auxiliary detection systems on the outside, such as neutron time-of-flight walls, can also be easily arranged. It has 8 symmetrically distributed flanges; 1 for the incoming beam; 1 for beamdump detectors; 1 for vacuum and venting; 1 for beam diagnostics and 4 with PCB feedthroughs, each with several 64-pin and LEMO connectors [36].

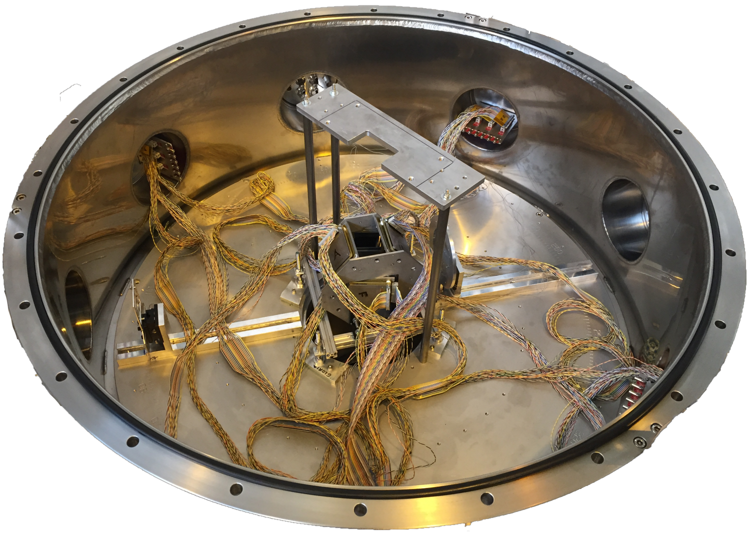

Figure 3.6: Arrangement of the IS619 setup inside the SEC chamber in August 2017.

3.2.1 The ^{15}C beam

The $^{15}C^{5+}$ radiactiove beam used for IS619 is produced with a hot-cathode plasma source coupled to a CaO primary target irradiated by the 1.4 GeV PSB protons. ^{15}C is extracted, ionized and mass-separated with the GPS magnet, sent to the REX-TRAP, where it is cooled down and pulsed in order to get more efficiently a higher charge state (5^+) in the EBIS. Afterwards, the beam is driven through HIE-ISOLDE to be post-accelerated. With the two cryomodules that were installed at the moment of the experiment, it was enough to increase the beam energy up to the required 4.37 MeV/u. The accelerated beam is directed to the XT03 line, where the SEC is coupled and the experiment is carried out.

Unfortunately, $^{15}N^{5+}$ and $^{12}C^{4+}$ (same $A/Q = 3$) remain in the final beam as residual gases from the EBIS. However, a 75 μg/cm^2 carbon stripping foil is placed right before the entry to the XT03 line. The efficiency to pass from charge state 5+ to 6+ in C is close to 100% whereas the suppression factor for $^{15}N^{5+}$ is about a factor of 100 for the given energy. This completely removes ^{12}C from the beam since it gets another value of A/Q. For the remaining ^{15}N the Coulomb barrier with ^{208}Pb lies around 76 MeV so a pure Rutherford scattering is expected, in principle not introducing any disadvantage [37].

The ^{15}C beam yield can be consulted in the ISOLDE database [38]. For the CaO primary target and 1.4 GeV booster protons it was supposed to be $7.9 \cdot 10^5$ pps after the GPS. Assuming 5% efficiency in the transport and stripping in the EBIS, it was estimated a $4 \cdot 10^4$ pps rate at the reaction target. Nevertheless, troubles in the production during the experiment only made possible a fluctuating ^{15}C beam intensity of about 200 pps. This reduction factor $\times 200$ in the expected beam intensity seriously limited the amount of information that could be extracted from the experimental data.

The spread in energy after the post-acceleration of the beam is measured and provided by the ISOLDE team, as shown in Fig. 3.7. The presence of the stripper foil in the XT03 beam line caused a little shift and spread of this profile before the entry in the experiment chamber, which will be discussed later on.

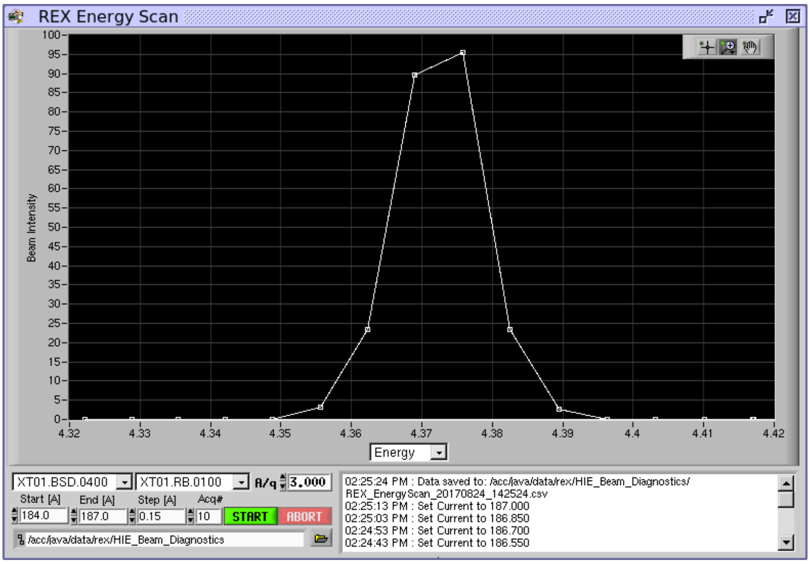

Figure 3.7: Scanned energy profile at $A/Q = 3$ beam ($^{15}N^{5+}$, $^{12}C^{4+}$, $^{15}C^{5+}$) after the post-acceleration process and before the stripping foil. X-axis in MeV/u and Y-axis in arbitrary units. The excellent beam energy resolution shows a FWHM of only 225 keV centered at 4.375 MeV/u.

3.3 The SPIRAL facility

The **G**rand **A**ccélérateur **N**ational d'**I**ons **L**ourds, in Caen (France), hosts one of the largest ion beam facilities of Europe: SPIRAL (**S**ystème de **P**roduction d'**I**ons **R**adioactifs **A**ccélérés en **L**igne). Contrary to the case of ISOLDE, heavy ion beams produced in the cyclotrons impinge on a relatively light target. It is able to deliver elements from ^{12}C to ^{238}U in an energy range from few keV to almost 100 MeV/u. It's been operational since 2001 and its research activity is specially dedicated to the study of exotic nuclear structure and collision dynamics.

The facility consists of a cascade of cyclotrons: two injectors (C01 or C02), two separated sectors (CSS1 and CSS2), and one post-acceleration compact CIME (**C**yclotron pour **I**ons de **M**oyenne **E**nergie), as seen in Fig. 3.8.

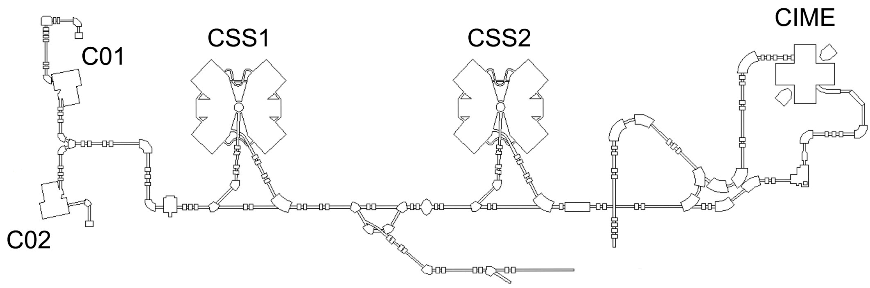

Figure 3.8: 2D layout of SPIRAL.

The wide variety of primary ion beams of GANIL allows for the election of the projectile best suited for the production of the required radioactive beam. The driver beam, from either CSS1 or CSS2, is made to impinge around the axis of the primary (but laminated) production target, from where the products are extracted by diffusion promoted with a gas flow. The efficiency of this process rapidly increases with the target temperature and that is why it is kept at around 2300 K. After it, they are transferred to the high charge state ECRIS (**E**lectron **C**yclotron **R**esonance **I**on **S**ource). There, RF waves accelerate the plasma electrons, which in interaction with the injected atoms lead to high charge state ions, typically with A/Q ratios from

2.5 to 11.1. After the extraction of this ions from the source, the low-energy beam is mass separated thanks to a magnetic dipole of resolution $m/\Delta m = 250$. The resulting beam can be then either directly delivered or sent to CIME for post-acceleration in a range from 4.8 up to 25 MeV/u [39].

3.3.1 The ^{17}Ne beam

The production of a ^{17}Ne beam in SPIRAL-GANIL is achieved by the fragmentation of a ^{20}Ne driver beam at 95 MeV/u impinging on a graphite target. Graphite is a refractory material able to sustain high temperatures without serious damages. It is a light material which is not activated, hence limiting contaminations and showing a large range of the primary beam in it. In view of the energy deposition over it (the narrowness of the Bragg peak would cause a rapid destruction of the material by evaporation and sublimation otherwise) a conical and laminated design (see Fig. 3.9) is frequently used in the facility. Its internal structure together with such design eases the diffusion of the products.

The final ^{17}Ne beam passes the ECRIS as a 3^+ charge state and with a maximum intensity after the post-acceleration with CIME of $4{\cdot}10^4$ pps. The energy range in which it can be delivered goes from 4 up to 8.2 MeV/u [40], being 8 MeV/u the chosen value in order to be slightly above the Coulomb barrier of the system with ^{208}Pb. No contaminants were present, but this depends on the cleanliness of the gas used in the production (^{20}Ne in this case).

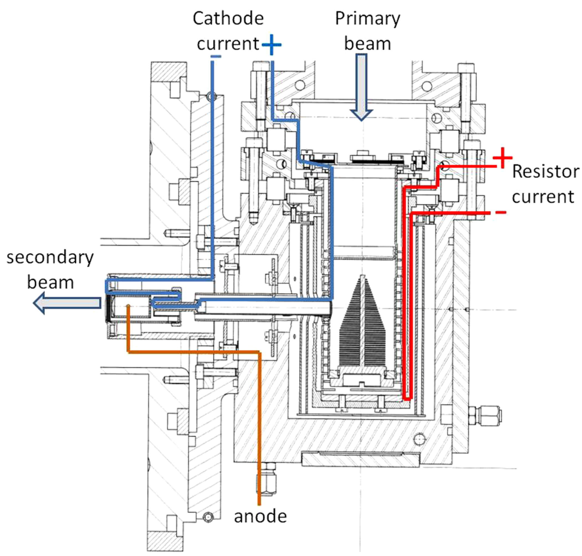

Figure 3.9: Conical laminated graphite production target of SPIRAL.

3.4 The GLORIA setup

The beam provided by the facility is sent to a chamber where the reaction of interest occurs. There, a detection system is arranged with a specific configuration depending on the physical case under study.

For the two experiments analyzed as part of this thesis, the chosen design is the **Glo**bal **R**eact**i**on **A**rray (GLORIA) [41]. This is a compact and large-coverage silicon array specially thought to measure charged particles coming from direct nuclear reactions induced by exotic nuclei. It consists of 6 particle-telescopes surrounding the reaction target and covers a continuous angular range from $15°$ to $165°$ (LAB). Its total solid angle coverage is 25% of 4π. The telescopes are placed in such way that a 30° rotation of the target off the beam direction avoids unwanted shading due to the ladder or the foil itself, introducing in counterpart asymmetries in the energy losses through the azimuthal φ angle. Each telescope is tangent to a 6 cm radius sphere and is made of two detectors: a 40 μm thick ΔE-detector and a 1 mm E-detector, with a distance between them of 8 mm. All detectors are fixed to a solid mechanical structure, minimizing in this way their relative freedom. As ΔE-stage, DSSDs have always been used in previous experiments. As E-stage, again DSSDs were used for IS619 but, instead, silicon pads were chosen for E788S, as it will be discussed later.

Manufactured by Micron Semiconductor Ltd., W1 type **D**ouble-sided **S**ilicon **S**trip **D**etectors are widely used in charged-particle spectroscopy and can be seen in Fig. 3.10. Their large 50×50 mm^2 area is divided in 16 p-doped strips on the front face and 16 n-doped orthogonal ones on the back face, each with a 3×50 mm^2 surface. These strips create 256 effective 3×3 mm^2 pixels. Front strips are defined by a 50 nm depth implantation of p$^+$-doping on the n-type silicon bulk. Back strips, however, are made up by boron implantation to a n$^+$-depth of 400 nm. The contact on the p-side is performed with a metal grid, covering only a 3% of the active area and, thus, making negligible the effect of the total front dead layer for high-energy particles. On the n-side, the contact is made with a 200 nm Al conducting surface, which, together with the 400 nm of doping results in a 600 nm back dead layer.

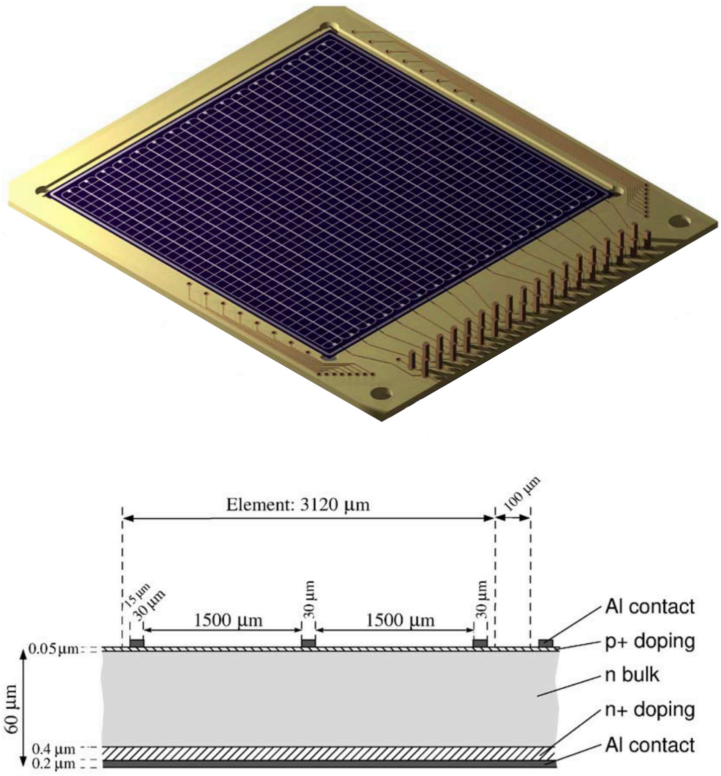

Figure 3.10: W1 type detector. Seen from the p-side on the top and 2D section throughout a n-side strip on the bottom [42].

The basic operation principle of semiconductor detectors is the creation of electron-hole pairs due to the passage of radiation through the depletion region. This ionization efficiency is close to 100%, although a tiny fraction might result in phonon creation and other interaction types which are, in any case, neglected. A reversed bias voltage creates the depletion zone where charge carriers can be generated and drives them onto electrodes where they are collected and measured.

The large amount of pairs means a very narrow (low statistical uncertainty) signal is achieved, hence the choice of this type of detectors for charged particle high resolution spectroscopy. Thicknesses usually go from few tens of microns (less than 20 μm implies large undesired non-uniformities) up to 2 mm (more than this is hardly depleted), what leads to a good telescope configuration ΔE-E when the particles to identify are not too heavy ($A < 20$) in an intermediate energy range ($\sim$MeV/u). Drawbacks are the fragility of such thin pieces and the manufacturing high cost.

3.5 Reaction targets

As reaction target, ^{208}Pb is widely chosen for reaction experiments. It is a stable nucleus with a $J^\pi = 0^+$ ground state and a large atomic number $Z = 82$, what creates a strong electromagnetic field, something convenient if the structure of the projectile is going to be studied through its Coulomb polarization. It is a doubly magic nucleus and thus very well bound. It is also the most abundant isotope of lead, with a presence of 52.4% in the natural composition. The large separation energy between the ground and first excited states ($E_{1^{st}} = 2.614$ MeV, $J^\pi = 3^-$, $T_{1/2} = 16.7$ ps) prevents undesired inelastic reactions from opening easily and polluting the elastic channel.

The thickness of the target is the main contribution to the experimental resolution; the widening of the spectra due to the straggling in such a heavy material exceeds any other source of energy uncertainty, like the intrinsic resolution of the silicon detectors or the beam energetic profile. It also dictates the amount of statistics: the number of reactions occurring is proportional to the number of scattering centers found. Therefore, target thicknesses are decided as a balance between these two factors. For IS619, two ^{208}Pb targets were available: one of 1.5 and another of 2.1 mg/cm^2 (see Fig. 3.11 with their position in the ladder). For E788S, however, only one target of 1 mg/cm^2 was used during the run. The density of ^{208}Pb is 11.38 g/cm^3, so the thicknesses are easily converted to microns, being 1.32 and 1.85 μm the cases of IS619 and 0.88 μm in the case of E788S. The target ladder is placed with a 30° tilt with respect to the beam direction, so the effective thickness is, in average (but strongly dependent on φ, enhancing the straggling in one side of the detector array), a factor 1/cos(30°) larger. A silicon detector, an empty frame and a collimator are always mounted together in the target ladder in order to ease the beam tuning, its centering and alignment inside the reaction chamber.

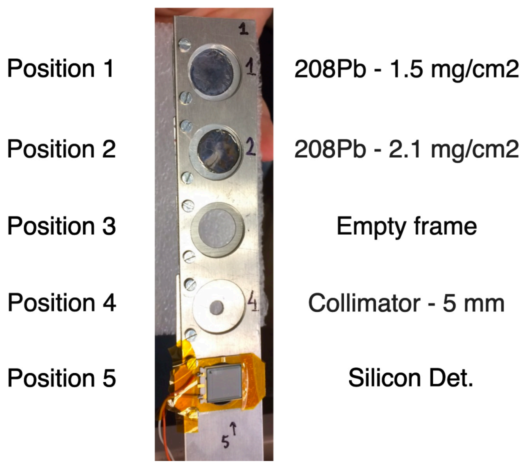

Figure 3.11: Target ladder used in IS619 experiment with the two ^{208}Pb targets, an empty frame, one 5 mm collimator and a silicon detector used for the beam tuning.

The IS619 targets were made at the University of Lisbon with enriched lead bought to ISOFLEX, claiming a 97.85% purity of ^{208}Pb and little residuals of ^{206}Pb (0.65%) and ^{207}Pb (1.5%). The unexplained bad resolution observed for the elastic channel (that cannot be reproduced with Monte Carlo simulations, as will be explained in Chapter 4) led to the hypothesis of a greater presence of ^{206,207}Pb in a range between the values specified by the provider of the material and their natural abundance, close to the 22% each. This fact could explain the overlap with inelastic contributions very close in energy that broaden the elastic channel and create a low-energy tail over it. That is why a composition test was proposed and approved (STD034/20 and STD042/21) at CMAM (the local 5 MV tandem at Universidad Autónoma de Madrid), in order to check the isotopic ratios of the ISOFLEX material. A Pb beam was produced by sputtering and studied in a fixed 3^+ charge state by varying a magnet current and measuring the collected charge with a Faraday cup after slits closed at maximum. A measurement with ^{nat}Pb gives a magnet current for ^{206,207,208}Pb of 94.05, 94.40 and 94.78 nA respectively which, compared to the spectrum obtained with the ISOFLEX material, shown in Fig. 3.12, leads to the conclusion of a proper composition of the material that is claimed by the provider. Hence the difference in resolution must be due to other factors such as inhomogeneities in the target thicknesses or imperfections in their placements.

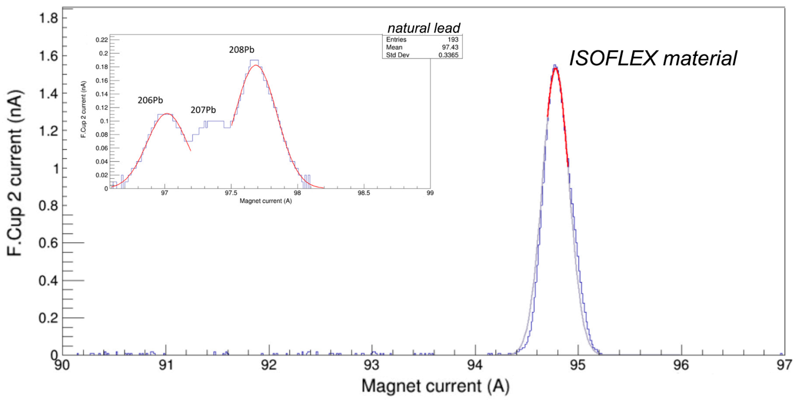

Figure 3.12: Faraday cup current versus dipole magnet current for the sputtering study of the ISOFLEX material. The only observed peak is fitted to a gaussian function. The inset shows the equivalent spectra measured for natural lead.

3.6 Acquisition system

The data acquisition system (or DAQ) is the ensemble of electronic modules and software that converts the resulting signals from the detectors to some type of structured digital file with the minimal relevant information about the experiment. It is usually subdivided into two parts: the *frontend* and the *backend*.

The frontend takes care of amplifying, digitizing the analog signals and discriminating which ones to save. The backend, on the other hand, is the software responsible of storing the final data, monitoring the acquisition and displaying preliminary online analysis in order to check the quality of the files. The link between these is the *readout*, handling the data extraction from the modules and the transfer to the backend. A schematic overview of a general DAQ is shown in Fig. 3.13.

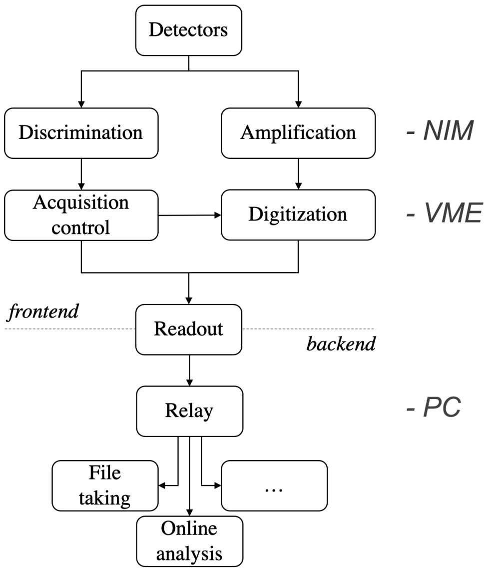

Figure 3.13: General scheme of the main components of the acquisition system (DAQ).

3.6.1 Triggering logic

Some criterion needs to be established to decide which signal is worth to save. The system is said to *trigger* on such signal of interest and the decision is usually based on amplitude terms. When a trigger arrives, the acquisition has to digitize the information and store it.

In a *synchronized mode*, independently of the module that triggers, the whole system starts digitizing, time during which the DAQ is *busy*. This period of time when no new triggers can be accepted is called dead time (DT), in contrast to the live time (LT), or time when the system is ready to accept and digitize new ones. During dead time, the acquisition control rejects any trigger request from the discriminated signals. During live time, a trigger request generates a `Master Start (MS)` logic signal that gates ADC modules and tells them to start the digital conversion. While this process lasts, the modules assert a logic `busy` that prevents the acquisition control to accept new triggers.

Once digitization is done, information is stored in the internal buffer of the modules and, before the system is ready to accept a new trigger, the readout transfers and saves it externally. This process is implemented with a VULOM 4b logic module using TRLO II firmware.

The total number of triggers, including the ones that have been rejected due to the system being busy, is saved by the acquisition control. This allows for the calculation of the dead time as the fraction between the accepted triggers and the total requested ones.

$$\mathrm{DT} = 1 - \frac{N_{acc}}{N_{tot}} \tag{3.1}$$

This value is used to correct for the dead time of a given file, dividing the saved number of counts of a detector by it.

Fan-in fan-out modules are used to replicate signals in the electronic chain. The *three-fold logic* sets the logic procedure functioning as `AND` and `OR` gates. The *dual timers* (also known as *gate & delays*) delay the logic signals and produce a gate for the ADC. The logic chain scheme of E788S experiment for the 6 telescopes of the setup is shown in Fig. 3.14.

3.6.2 Signal processing

A 9 MeV charged particle fully stopped on a silicon detector generates 0.3 pC of charge. This charge is converted to a voltage signal in a pre-amplifier, (MPR-64) always kept close to the detector in order to avoid noise pickup. Such signal is characterized by a fast rise and a slow exponential tail and is sent to an amplifier (STM-16+), where it is further amplified and limited in bandwidth, producing a 0-8 V gaussian signal with a typical FWHM of 1-2 μs (shaping time $\sim$0.5 μs).

Analog-to-Digital converters are based on a charge capacitor to get the maximum value of the amplified signal. The time during which the input signal is analyzed is controlled by a `GATE` logical signal. The analog signal is converted into a digital one, dividing the maximum amplitude that the module may receive as an input into 4096 possible values (actually into 2^n with n the number of bits, which is 12 in our case) and allocating it to a channel. The signal is analyzed, converted and buffered while asserting a `BUSY` that asks for the acquisition control to wait. The main source of DT comes from the combination of this `GATE` and the conversion time, which in the CAEN 785G modules that were used in both IS619 and E788S experiments, take about 10 μs (4 μs event window + 2 μs/conversion $\times$ 3 conversions). The electronic is designed to keep a linear relationship with the energy deposited in the detector by the charged particles.

In order to provide a good timestamp, *constant fraction* discriminators are used. If the arrival time is chosen when the signal surpasses a threshold, two simultaneous signals with different amplitude will have different time signature. The CFD module duplicates, delays and inverts every signal, and then sum them to obtain a constant crossing point. The output signal surpasses the offset value at the same instant independently on the amplitude and thus provide a good time reference. Discriminators assert a logic value whenever the signal passes such offset and pass it to the Time-to-Digital converters, that timestamp the arrival of the signals. A TDC trigger from the acquisition control tells to save all channels that were fired within a time window, usually set to 4 μs, which defines the duration of an *event*. V1190 128ch TDC modules were used.

TDCs were only connected to the p-side of DSSDs, and PIPs (Passive Implanted Planar silicon detectors used for beam tuning) were added to the final logic module. In the IS619 experiment, E-detectors were also DSSDs, so an analogous chain to those of the ΔE-detectors was set up. A positive pulser signal was connected to all p-side detector channels in order to correct for the efficiency of the electronic chain if needed.

Modules are based in VME crates and communicated via VME bus. To read data from the buffer, move to a physical disk and subsequently empty the modules, the system needs to receive from the acquisition control a readout trigger, reporting a DT while it is carrying out its duties. The Nustar Readout Library [43] handles the code running on a Single Board Computer in the same crate for such communication.

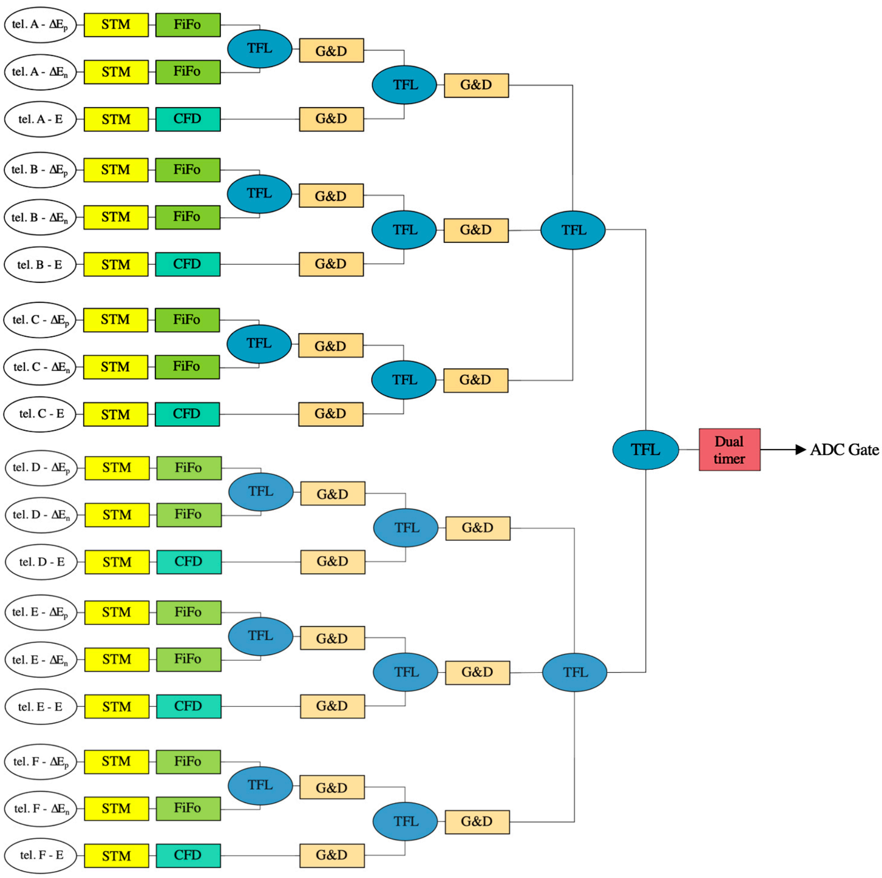

Figure 3.14: General trigger logic for E788S experiment. All Three fold logic modules (TFL) working as `OR` gates.

3.6.3 Backend software

Backend softwares usually run on a desktop computer connected to the same network as the readout node. The most essential task is the data storage, but online analysis and monitoring are always of great importance to check possible flaws in the acquisition, the beam or the detectors functioning.

The *relay* decouples all possible tasks. It receives the readout data and produces different streams. Usually one of them, dedicated to the data storage, requires an external action to start/stop the acquisition, and another one, for the online analysis, continuously consumes the incoming data and shows some preliminary analysis of it.

Data storage was done using list mode (`.lmd`) format, i.e. stored in an event by event basis, that needs an unpacking process later. For security reasons each file is separated in parts of few hundreds of Mb and compressed. The online stream is sent to a user interface that allows for showing some basic analysis of the incoming data, such the mapping of the ADC channels to detector strips or applying calibrations. More complicated routines can also be implemented but, since every experiment requires very specific and complex conditions, it's rather difficult to get it ready during the progress of the acquisition, leaving a detailed offline work to a subsequent moment.

The framework for the relay process was `MBS` (Multi Branch System) [44] for IS619 (and all experiments carried out at the XT03 of HIE-ISOLDE between 2016 and 2018). The `Go4` [45] online interface and the `Ausalib` [46] routines were used for the online analysis. The global `DaqC` ensemble, which allowed for an intuitive control of the acquisition, was developed by J. Jensen and M. Munch from the Aarhus University in 2016, based on H. T. Johansson work [47].

For E788S, however, `MIDAS` (Multi Instance Data Acquisition System) [48] was used, developed by the Euroball collaboration as a general purpose acquisition system adapted for medium scale experiments involving particle detectors and VME hardware. The software is written in `C` and free licensed.

3.6.4 Data structure

The `.lmd` files that are saved during the experiment by the acquisition system need an *unpacking* process before they can be analyzed. The *unpacker* gets the information provided by the electronic modules and organizes the data in some type of structure according to analysis conveniences. This is done in `ucesb (unpack & check every single bit)` [49] for IS619 experiment, since all the backend used in this case was implemented with this tool. However, a `C` program adapted to the `MIDAS` output was developed by A. Perea for the E788S experiment in order to unpack data. The user needs to specify the modules that are used, their corresponding channels and the data layout in the stream. This task is done during the setup of the acquisition system, so it is used all through the experiments.

Unpacked files are given in `.root` format and data are stored in a `TTree` structure, class which is optimized to reduce disk space and enhance access speed. From the `TTree` hang different *leaves*, each one holding specific type of data, such as objects, arrays or simple types, for every recorded event.

For DSSD data, the most common structure consists of the following leaves:

- `DSSD_F`: The multiplicity in the front strips of the detector for every event. An integer number between 1 and 16.

- `DSSD_FI`: The identification numbers of the hit front strips. An array of integers (from 1 to 16) with size equal to `DSSD_F`. Saved in ascending order.

- `DSSD_F_E`: The energy channel for every hit in the front strips. An array of integers (from 0 to 4096) with size equal to `DSSD_F`. Each position in this array corresponds to the strip indicated in the same position of `DSSD_FI`.

- `DSSD_F_T`: The time signal for every hit in the front strips. An array of integers with size equal to `DSSD_F`. Same position correspondence as the previous array. Notice TDCs are frequently only connected to one side of the DSSDs.

- `DSSD_B`: The multiplicity in the back strips of the detector for every event. Analogously to the front side.

- `DSSD_BI`: The identification numbers of the hit back strips.

- `DSSD_B_E`: The energy channel for every hit in the back strips.

In addition, other leaves are added in the `TTree` depending on the availability of extra signals. The PIP detectors data, time signals from the facility clocks (such as the references of the bunch releases from the ion source or the pulses impinging on the primary target) and patterns indicating the detectors that trigger each event are often accessible to the acquisition system.

4
Monte Carlo simulations

The Monte Carlo toolkit `Geant4` [50] is a software dedicated to the simulation of the passage of radiation through matter and it is the result of a worldwide collaboration that started at CERN in 1993. Based in an object-oriented methodology and in the practical `C++` programming language, it is widely used in the field of nuclear and particle physics. It is the chosen tool for the simulation of the detector setup GLORIA and its response to the radioactive ion beams used in IS619 and E788S experiments. Simulations result of great importance for understanding the measurements, being a crucial step for geometry optimizations and energy calibrations, as it will be discussed. The code is split in six different parts, each performing one task, which are going to be discussed along the sections of this chapter, paying special attention to the details that are more relevant to the needs of these experiments.

4.1 Detector geometry

The setup geometry is defined, being DSSDs simulated as a set of 16×16 adjacent squared 3.12×3.12 mm silicon pixels (the 0.12 inter-strip gap is not simulated). Two continuous silicon layers on each side of the set of pixels recreate the dead layers: one of them 50 nm thick corresponds to the front side and another 600 nm thick to the back side. ΔE detectors are allocated tangent to a 6 cm radius sphere, in which center the reaction target is placed. E detectors are situated 8 mm behind each ΔE, according to measurements of the GLORIA support. A ^{208}Pb foil is centered in the sphere conformed by the detectors, with a 30° tilt with respect to the beam direction (z-axis) to avoid the shadowing of any telescope. Each detector is firstly defined on the Y-Z plane and centered in the origin of coordinates, then they are rotated according to Tab. 4.1 and later are translated to their respective positions keeping the distances that are mentioned. Front dead layers are always placed on the side of the detectors that face the target. An identification number is assigned to every volume that is defined (silicon pixels, dead layers and lead target). This way, a correspondence list is made with the experimental data pixels.

Table 4.1: Rotation angles that characterize the telescopes of the GLORIA setup departing from the Y-Z plane.

Telescope	R_x	R_y	R_z
A	0	52°	0
B	0	-52°	0
C	0	52°	0
D	0	-52°	0
E	75°	90°	0
F	75°	-90°	0

The ensemble of telescopes and reaction target defined in the simulation is shown in Fig. 4.1, where the coordinate axes and the beam direction are marked. Detectors in the ΔE stage of each telescope will be labeled with a single letter, e.g. 'A', and detectors in the E stage with a double letter, e.g. 'AA'.

Angles covered by each stage and telescope are shown in Tab. 4.2. Note the high symmetry of the setup, with all telescopes tangent to a sphere centered at the target and hence covering the exact same solid angle $\Delta\Omega$. E-stage detectors are, however, more restrictive since they are the same size but placed further from the target. This fact will be limiting when imposing coincidences between the two detectors of a telescope.

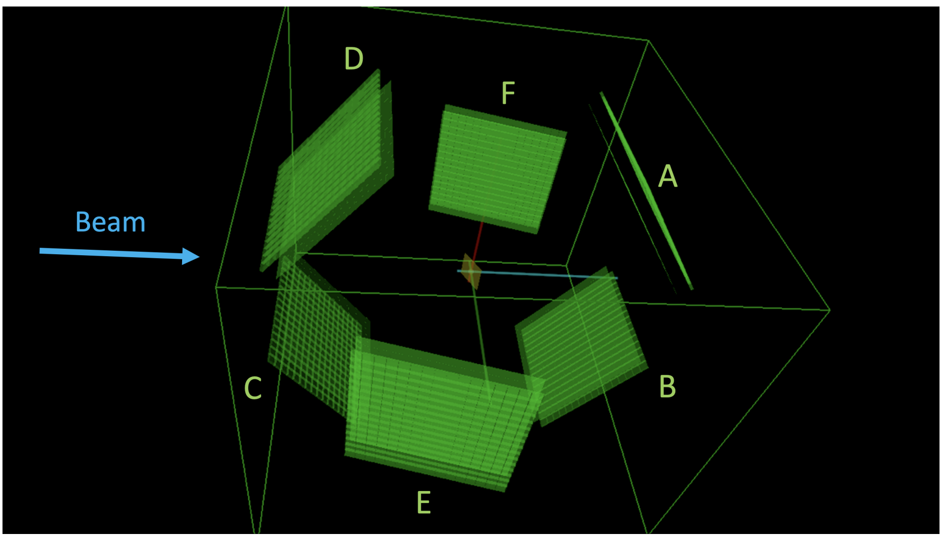

Figure 4.1: Visualization of the detector setup defined in the Geant4 simulations. X-axis in red, Y-axis in green, Z-axis in blue and reaction target in the origin of coordinates.

Table 4.2: Angles coverage by each detector of the GLORIA setup in the nominal configuration.

Detector	$\Delta\theta_{LAB}$	$\Delta\varphi_{LAB}$	$\Delta\Omega$
A	16.75 – 61.33°	-51.67 – 51.67°	547.84 msr
AA	19.05 – 58.80°	-44.97 – 44.97°	440.32 msr
B	16.75 – 61.33°	-128.33 – 128.33°	547.84 msr
BB	19.05 – 58.80°	-135.03 – 135.03°	440.32 msr
C	118.67 – 163.25°	-51.67 – 51.67°	547.84 msr
CC	121.20 – 160.95°	-44.97 – 44.97°	440.32 msr
D	118.67 – 163.25°	-128.33 – 128.33°	547.84 msr
DD	121.20 – 160.95°	-135.03 – 135.03°	440.32 msr
E	83.70 – 126.29°	65.73 – 114.27°	547.84 msr
EE	86.01 – 123.98°	68.57 – 111.43°	440.32 msr
F	53.71 – 96.30°	-114.27 – -65.73°	547.84 msr
FF	56.02 – 93.99°	-111.43 – -68.57°	440.32 msr

4.2 Physics lists

In the simulation there are no time considerations and each event ends when all possible decays are completed and all particles have either deposited all their energy or escaped from the mother volume defined. On the other hand, the experimental event time window (4 μs) is much smaller than the half lives of the nuclei of interest (^{15}C and ^{17}Ne) and practically all events are over before the decay occurs. Hence, if we let the ions to decay in the simulation, we would observe the decay products and the recoil energy within the simulated events and the comparison with the experimental data would not be suitable. This is the reason why, despite having radioactive species in the beams, the decay libraries are disabled and only the standard electromagnetic physics library is used.

The effects of letting the beam ions to decay are shown in the Fig. 4.2, where the incoming ^{15}C beam, with the properties provided by the facility (energy centroid and FWHM), is made to impinge on a bulk silicon piece thick enough to ensure it completely stops.

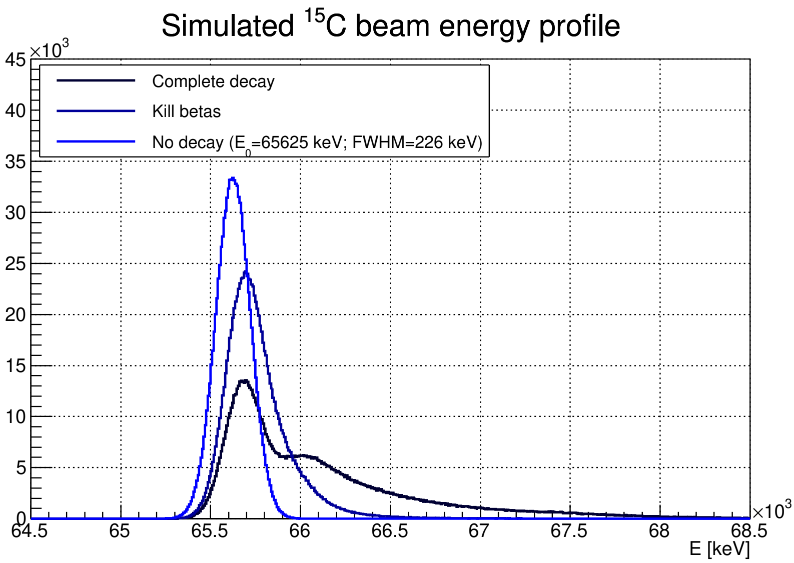

Figure 4.2: Energy profile of the incoming ^{15}C beam when letting it completely decay, killing beta particles and preventing it from decaying.

When the ^{15}C beam is let to decay, we observe a main peak corresponding to the kinetic energy profile of the ^{15}C beam convoluted with its β decay spectrum, creating a prominent bump towards higher energies. If we let it decay but kill all β particles, we see an asymmetric peak with a high energy tail due to the recoil of the daughter nucleus. Only preventing the ion from decaying we get the gaussian kinetic profile of the beam.

The energy loss and spread of the beam profile in the 75 μg/cm^2 carbon stripping foil and in the lead targets (1.5 and 2.1 mg/cm^2) are then calculated. Targets are defined with half their real thicknesses in order to get the profiles in their middle point, from where the ions will be launched later. See Fig. 4.3 with the energetic profiles at the different instances. In this figure all spectra are normalized, so a loss in height implies a widening of the peak.

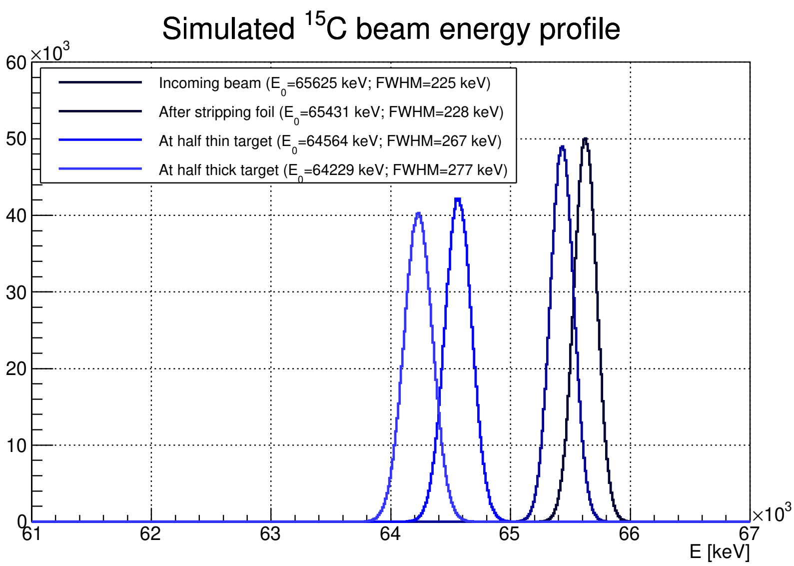

Figure 4.3: Energy profile of the incoming ^{15}C beam before the stripping foil, after the stripping foil and at half the target thicknesses.

The stripping foil causes a loss of barely 200 keV and a negligible spread. However, in the lead target the beam losses are close to 1.5 MeV, considerably widening the FWHM of the incoming beam.

4.3 Particle generation

Particles are launched from the origin of coordinates, in the center of the reaction target, where we assume the scattering happens. The energy profile at this point has first to be calculated, as it was explained in the previous section, taking into account the losses in the first half of the target (and in the stripping foil if it existed). With the centroid of the energy profile, the kinetic curve, shown in Fig. 4.4, is calculated [51]. With this method it is possible to select the range of scattering angles in which ions are ejected and, thus, save a valuable computation time. We avoid simulating the scattered particles going into the very forward directions, as they are not detected by the setup. The main disadvantage of assuming all reactions happened at the same point is a little loss of accuracy in the simulation but it is, in any case, smaller than the experimental resolution induced by the straggling in the lead target, compensating the choice of the method.

The generation of the scattering angles is done according to the Rutherford cross section, which in the CM frame reads

$$\frac{d\sigma_R}{d\Omega} = \left(\frac{1}{4\pi\epsilon_0}\frac{Z_a Z_A e^2}{4E}\right)^2 \frac{1}{\sin^4(\theta/2)} \tag{4.1}$$

Where Z_a and Z_A are the atomic numbers of projectile and target respectively, E the energy of the system and the differential solid angles $d\Omega = 2\pi\sin(\theta)d\theta$ concentric rings on the sphere surface covering a differential scattering angle $d\theta$.

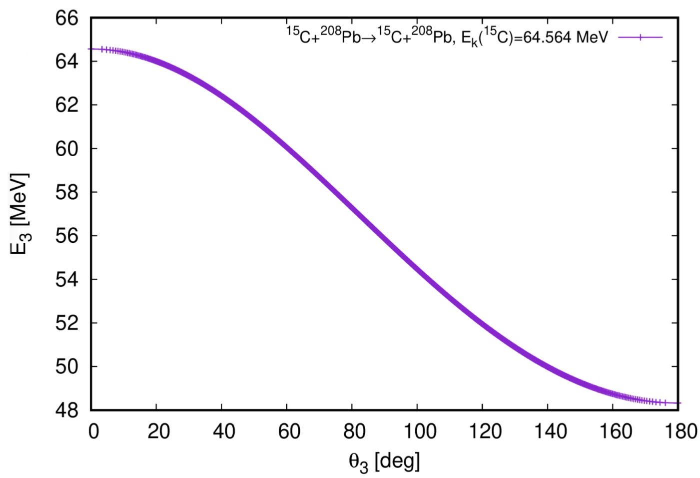

Figure 4.4: Kinetic curve for elastically scattered ^{15}C on ^{208}Pb assuming the reaction occurs at half the thick target thickness. Data from [51] with the information from Fig. 4.3. Y-axis is the lab. kinetic energy of ^{15}C after the reaction and X-axis is its lab. scattering angle.

The fact that the differential expression of the cross section is given for differential solid angle rings $d\Omega$ of the sphere, which depend on θ, has to be carefully taken into account in the random generation of the scattering angles. A flat cross section would mean that for any angle the probability of finding a particle is the same, regardless the size of $d\Omega$. Then, on the sphere surface we would find a larger concentration of particles near the poles ($\theta = 0, \pi$). This could be simulated generating uniformly distributed random numbers on the intervals $[0,\, \pi)$ for θ and $[0,\, 2\pi)$ for φ, which means a uniform distribution of particles on the cartesian θ-φ plane (not on the sphere surface as one could wrongly interpret). Extrapolating this case, it is easy to see how a good angle generation for the Rutherford cross section would be uniform in $\varphi \in [0, 2\pi)$ and with a $\sin^{-4}(\theta/2)$ distribution in $\theta \in [0, \pi)$. In order to avoid too low and too high scattering angles with no interest, we will generate $\theta \in [\pi/20, 19\pi/20)$ and, therefore, the normalization constant for the distribution will be

$$\int_{\pi/20}^{<19\pi/20} \frac{1}{\sin^4(\theta/2)} d\theta \approx 1392.8 \tag{4.2}$$

With this value, the height method for a random generation of θ with a Rutherford distribution is followed by

- Generating a first uniformly distributed random number *rand1* in the range $\theta \in [\pi/20, 19\pi/20)$
- Generating a second uniformly distributed random number *rand2* between zero and the maximum of the normalized distribution

$$\frac{1}{1392.8} \frac{1}{\sin^4\left(\frac{\pi}{20}/2\right)}$$

- Accept *rand1* as the scattering angle θ if *rand2* is lower than the normalized distribution evaluated at *rand1*

The generated angles θ are analytically converted to the lab. frame, which is the one observed with the setup, before they are launched in the simulation.

4.4 Trajectory step

The step length during the Monte Carlo simulation is by default set too large in some situations and might lead to a wrong energy deposition estimation when volumes are very thin. This is our case with thin reaction targets, ΔE detectors and, specially, front and back dead layers of the W1-9G detectors. This is why, in these potentially conflictive volumes, the step length is specified to ensure enough interaction steps and a good energy deposition. It is done with the `G4UserLimits` class, which applies over a logical volume passing as parameter the maximum step limit. For the reaction target this limit is set to 200 nm, for the front dead layers to 10 nm and for the back dead layers to 100 nm. For all other volumes, limits are not specified since no problems in the simulations have been observed.

4.5 Event construction

A particle is launched from a given position with certain initial energy and direction. No decay is allowed so the most common case is that the generated ion losses its kinetic energy as it keeps passing through different material volumes in a mainly rectilinear direction. Regardless time considerations, each event ends once the particle either has deposited its full energy in the setup materials or has escaped from the mother volume in which the setup is defined. The number of volumes in which some energy is deposited defines the multiplicity of the event and it will be used to determine the (anti-)coincidences between detectors in the data analysis. Two arrays with size equal to this multiplicity value store the identification numbers and energies of the different hit volumes. These three variables, together with the event number, fill the `TTree` once every event is over.

4.6 File structure

The designated variables of interest of all the events are saved in a `.root` file with a `TTree` which is created at this instance. The defined data leaves are defined according to the type of the variables that are being recorded and the access to these values is specified. This output file contains all relevant information with the most basic structure but, for analysis convenience, it usually has to be rearranged for an easier comparison with the experimental data. The more practical file structure depends on the experimental setup and on the physical case to study so this has to be adapted for every experiment.

4.7 Simulation predictions

In the following plots, simulations of the elastic scattering of the radioactive beams of IS619 and E788S experiments are shown. In Fig. 4.5, the expected energy deposition in the GLORIA detectors for ^{15}C under IS619 conditions, i.e. at 4.37 MeV/u on a 2.1 mg/cm^2 ^{208}Pb target, with the nominal geometric values of the setup. The two-dimensional plots, built as ΔE versus ΔE+E, of every telescope are shown. The kinetic curve is calculated as previously explained and introduced as an input, but the measured ΔE+E energy depends on the outgoing direction of the particle due to the geometric disposition of the detectors and target, so the expected observation is shown to the right. Note the discontinuities in energy between detectors that are caused by the asymmetries in the azimuthal angle related to the target tilt respect to the beam direction.

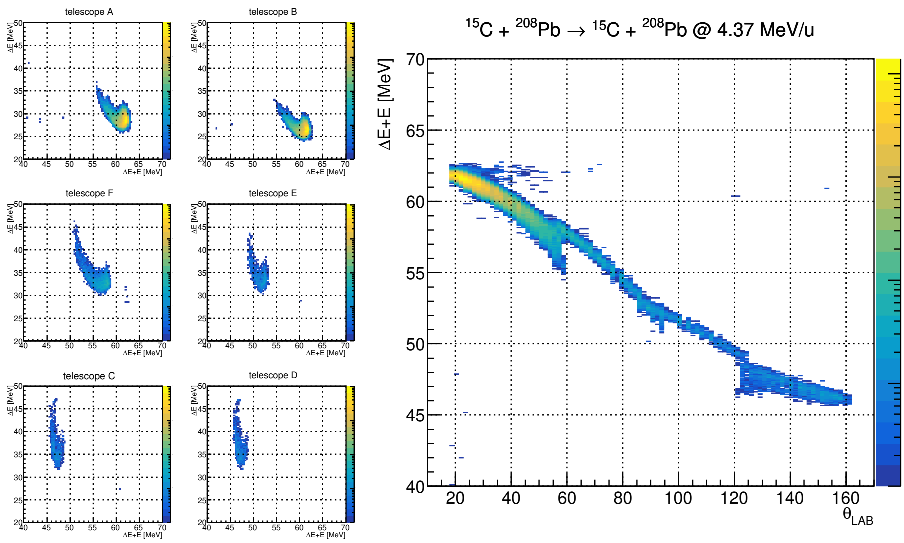

Figure 4.5: Simulation for elastically scattered ^{15}C on 2.1 mg/cm^2 ^{208}Pb 4.37 MeV/u. To the left: two-dimensional plots (ΔE vs. $\Delta E+E$) of the six telescopes of the GLORIA setup. To the right: measured kinetic curve obtained adding together these telescopes.

Same simulation is done for the E788S experiment, with a ^{17}Ne beam on a 1 mg/cm^2 ^{208}Pb target at 8 MeV/u; see Fig. 4.6. In both cases the elastically scattered ions do not stop in the ΔE detector at any angle so they can always be identified as discrete spots in the two-dimensional plots (mass spectra). This is why an accurate cleaning condition can be set by imposing coincidences between ΔE and E detectors of each telescope, only loosing boundary strips data due to the divergence of the trajectories of the scattered particles from the reaction point (remember sizes of ΔE- and E-detectors are equal so there is not a 100% geometrical overlap in their solid angle coverage). It's important to remark the influence of the target thickness in the resolution of these reaction experiments, and how a target twice as thick in the ^{15}C case translates into much wider peaks despite the fact of being a nucleus lighter and less charged than ^{17}Ne.

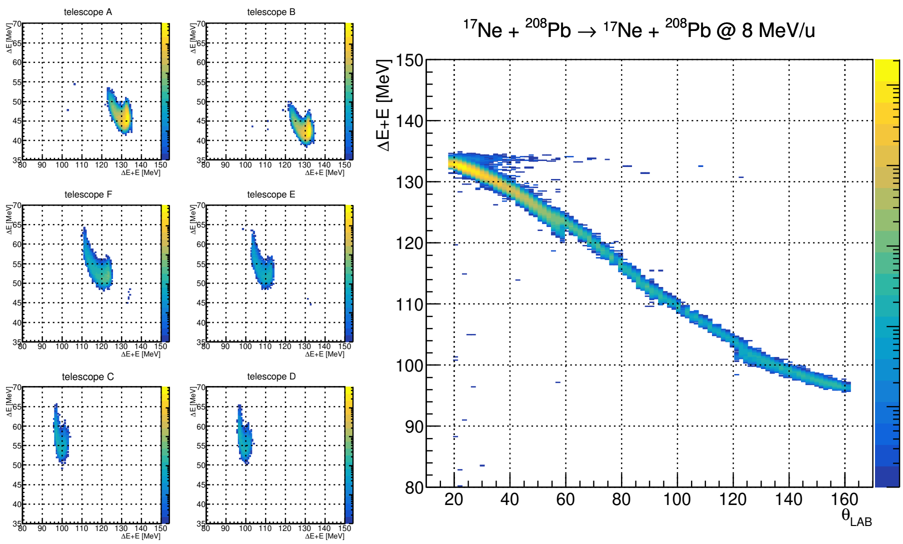

Figure 4.6: Simulation for elastically scattered ^{17}Ne under E788S conditions. To the left: two-dimensional plots (ΔE vs. ΔE+E) of the six telescopes of the GLORIA setup. To the right: measured kinetic curve obtained adding together these telescopes.

The elastic angular distributions of these reactions are not known and, as this is the final goal of the measurements of this thesis, the simulations are used for energy loss estimations, regardless the amount of counts observed. Still, the Rutherford cross section has been used for the simulations since deviations from this trend are expected to be small. Furthermore, the presence of ^{15}N in IS619 beam at an energy quite below the barrier (hence exhibiting pure Rutherford scattering) is used as a reference during the analysis. The simulated ^{15}N angular distribution is shown in Fig. 4.7. There, it can be seen the hit patterns of the six ΔE detectors of the GLORIA setup with a color legend that reflects the number of counts measured in every pixel. Due to the strong decreasing trend of the Rutherford formula it is appreciated how most of the counts go to the forward detectors A and B, which cover symmetric scattering angles, hence they show identical data except for statistical fluctuations. The number of counts is integrated pixel by pixel, normalized by the covered solid angle and plotted versus the scattering angle converted to CM frame, leading to the image shown to the right. Notice, in this case, due to the thicknesses of the detectors and the evolution of the kinetic curve, ^{15}N stops in the ΔE stage from telescope F onwards, being necessary to integrate the corresponding ΔE detectors in order to get a proper angular distribution. In the last two telescopes C and D, where the Rutherford cross section becomes almost flat, is noticeable how there is an increase in the number of counts in the hit patterns for the last angles ($\sim$165°; pixels F1B8) due to the dependence of $d\Omega$ on $\sin(\theta)$, as already explained in section 4.3. Despite this apparent increase in the number of counts, after normalizing the counts by the solid angle of the pixels, the resulting distribution has a continuously decreasing trend, as the expected $\sin^{-4}(\theta/2)$ function. This effect, that might result counterintuitive, arises from the fact of changing from polar to spherical coordinates after the reaction occurs, as result of the interaction of the incident beam with a central potential.

In situations where the angular distribution is not relevant and the interest of the simulations exclusively lie on the energy deposition, the generation of the scattering angles is done uniformly on a spherical surface, in order to optimize computational time and get good statistics even at backward angles. This means, if φ is uniformly generated in $[0,\ 2\pi)$, then θ is calculated as $\mathrm{acos}(1 - 2 \cdot rand1)$, being $rand1$ a uniform random in $[0,\ 1)$. The following conversion of θ_{CM} to the lab. frame tends to concentrate the points towards one pole but, with such a large difference in mass between projectile and target, the distortion is negligible.

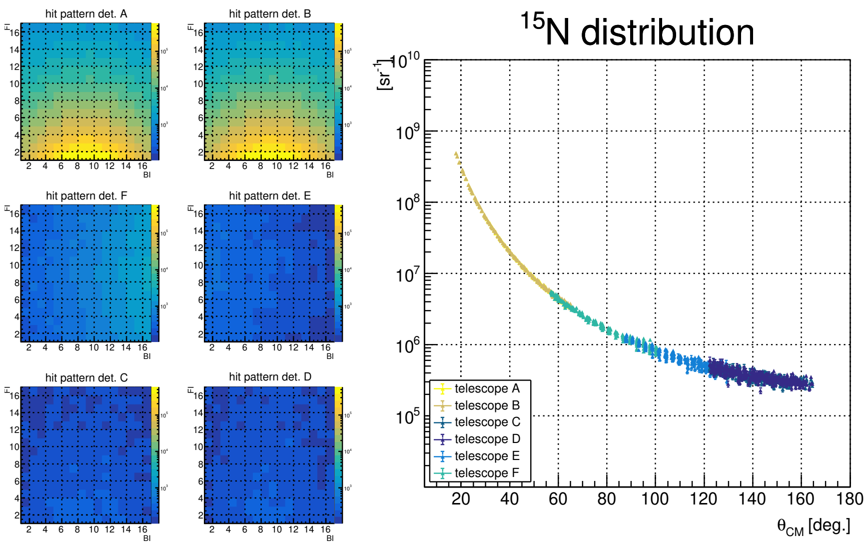

Figure 4.7: Simulation for elastically scattered ^{15}N with IS619 conditions. To the left: hit patterns of the six ΔE detectors of the GLORIA setup. To the right: angular distribution of the normalized number of counts in each pixel.

To obtain the distribution shown in Fig. 4.7, angles are assigned to the geometrical centers of the pixels. The solid angles are approximated by the expression

$$d\Omega_{pix} \approx \frac{9\text{mm}^2}{r^2}\cos(\alpha) \tag{4.3}$$

Where 9 mm^2 is the area of the 3×3 mm pixel, $\vec{r}$ is the vector from the center of each pixel to the reaction point (assumed in the origin of coordinates) and α is the angle formed between $\hat{r}$ and the normal vector of each pixel $\hat{n}$, calculated as $\cos(\alpha) = \hat{r} \cdot \hat{n}$.

The losses in the target after the reaction occurs (assumed in the center of the volume) and in the dead layers of the detectors is obtained from the simulations as well. For elastic ^{17}Ne in E788S experiment, the profiles of the energy deposition in these different volumes is shown in Fig. 4.8 and the total energy accumulated has a mean value of 1.93 MeV. In the same way, for ^{15}C in IS619 experiment, with the this mean value is found to be 2.65 MeV and 2.11 MeV for the 2.1 and 1.5 mg/cm^2 targets respectively.

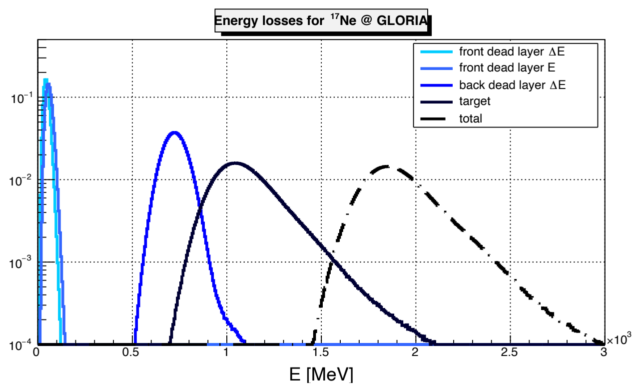

Figure 4.8: Simulation of the energy losses for elastic ^{17}Ne in the target and dead layers of the GLORIA setup used in E788S experiment.

5
IS619 experiment

The first physics run of HIE-ISOLDE (CERN, Geneva, Switzerland) at the SEC beamline, carried out in August 2017. The goal of IS619 experiment was to probe the halo structure of ^{15}C at energies near the Coulomb barrier, which had never been studied before. With two cryomodules of the superconducting LINAC working at that time, a ^{15}C beam could be accelerated up to the desired 4.37 MeV/u (slightly below the Coulomb barrier) and made to impinge on a ^{208}Pb target, aiming to measure the angular distribution of the elastic scattering and study whether it is distorted and other reaction channels are open due to the halo configuration of the nucleus and the almost pure s-wave nature of its ground state wavefunction. The already detailed GLORIA setup was chosen for this purpose.

5.1 Alpha calibration

Calibration files before and after the beam measurements were taken with the α source of ISOLDE, whose specifications are shown in Tab. 5.1. Two files were taken each time: one facing ΔE detectors and another one facing E detectors of the GLORIA telescopes. The source emits isotropically so the observed number of counts uniquely depends on the solid angle covered by each detector/pixel. The four emitters are deposited on the source support and the vacuum was good enough before starting the acquisition so we can assume no energy losses occurred before the alpha particles hit the detectors. Furthermore, at these energies, all α particles are fully stopped in all detectors (no *punch-through* occurs) and their front dead layer (50 nm of doped silicon) can be neglected in energy loss terms.

Table 5.1: Four-alpha source information. Nuclei that compose it and their respective emission intensities and energies.

$\times 4$ α source		
Nucleus	Intensity	Energy (keV)
^{148}Gd	100%	3182.8
^{239}Pu	10.6%	5104.7
	15.1%	5142.8
	73.2%	5155.5
^{241}Am	1.4%	5388.0
	12.8%	5443.0
	85.2%	5485.7
^{244}Cm	23.6%	5762.8
	76.4%	5805.0

Due to the large dynamic ranges of the detectors (>40 MeV), all peaks lie at the very beginning of the spectra, what implies a loss of accuracy at high energies due to a large extrapolation of the calibration. The resulting calibrated energies are, in principle, valid in the whole energy range due to the linear response of the silicon detectors. However, the calibration is done in the low energy part and one should be aware that deviations can happen so, the further we measure from the last alpha peak ($E \gg 6$ MeV), the more disagreement we could expect with real energy values. Despite the possible wrong extrapolation, the alpha calibrations are completely independent to external factors such as the position of the detectors or target and beam properties, so these are a rather good first approximation.

The energy spectrum of every strip is plotted with a strict multiplicity equal to 1 condition. Four maxima are found and gaussian fits are performed. The centroids of the resulting fits are assigned to the energy values shown in Tab. 5.1 and a linear regression between channels and energies is calculated, e.g. the fits shown in Fig. 5.1 give a calibration line with an offset of 474.9 keV and a slope of 15.5 keV/channel (other strips have similar values).

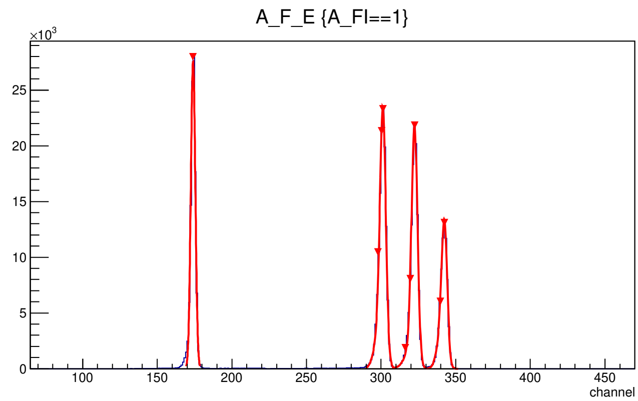

Figure 5.1: Gaussian fits to the 4 emitters in the alpha source used for calibration. Spectrum of the first front strip of detector A. Centroids of the fits are remarked with a triangle. Notice that only the first 475 channels of the spectrum are shown.

So far we obtained the calibration per strip, which can be applied to the same spectra from where we got the gaussian fits.This will let us check how good the obtained regressions are in this energy range and we will be able to compare the different strips behavior. With this purpose an overlay of the 16 front calibrated strips and the 16 back ones of detector A is shown in Fig. 5.2. From it we observe several features. One of them is that the resolution of the front side of the detector (p-doped side) is defaulty better than the one of the back side (n-doped side). For the ^{148}Gd peak, with only one alpha line, we observe nothing but the detector response to a monochromatic energy source and hence its intrinsic resolution, finding full widths at half maxima (FWHMs) varying from 49.7 to 55.4 keV in the front strips and from 63.4 to 67.4 keV in the back strips.

It is noticeable, looking at the spectra in logarithmic scale, an artificial lack of counts at around 4 MeV on every strip of detector A and B. This effect turned out to be due to a misconfigured setting (the baseline restorer threshold, which can only be adjusted by the remote control) of the *Mesytec* amplifier modules (MSCF) and is appreciated in two of the detectors in this experiment (A and B). Luckily, this valley lays in zone between peaks and therefore it does not prevent us from a proper peak fitting for the calibration. Unfortunately, this will be the proton region in the radioactive beam files and they may not be integrated.

It can be seen how the boundary strips (1 and 16) on each detector side show, in general, worse resolution and, sometimes, a deficit in the counting rate. These effects, due to a losses in the charge collection at the detector boundaries, are expected when *guard rings* are not biased, which is usually the case in experiments with large number of DSSDs and electronic channels. Removing these faulty strips from the analysis whenever strange behaviors are observed is instead a frequently used method.

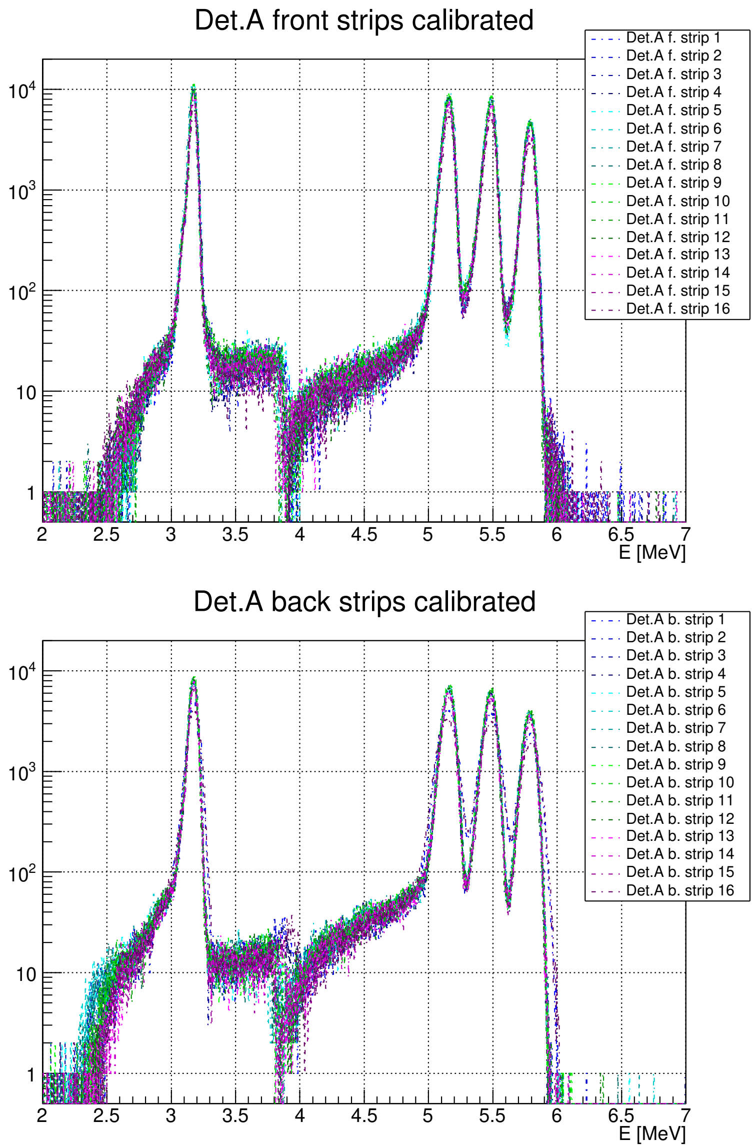

Figure 5.2: Overlay of the calibrated alpha spectra of the 16 front strips (top) and the 16 back strips (bottom) of detector A.

5.2 Energy matching

Once front and back (p- and n-) sides of the DSSDs are calibrated in energy, an energy matching has to be done. This first cleaning process of the analysis consists of making a correspondence, for every event, between the hits measured in the front strips and the hits in the back strips. Hits from the two sides are paired according to the best energy agreement, and that is why a first calibration, although it might be rough, is required. All hits that remain unmatched, either because there is a different multiplicity on the detector sides or because the energy difference is greater than an established limit and cannot pass the threshold condition, are removed.

Only after matching sides, the multiplicity in the front strips is the same as in the back strips, and a logic number of hits per pixel (hit pattern) in DSSDs is achieved. Also the difference in behavior between the detector sides can be seen in front versus back energy plots, like the ones shown in Fig. 5.3. Most of the events lie in the diagonal (front equals back energy), meaning a good matching performance. The shape of the peaks in this front-back energy plane gives account of the different resolution of the detector sides, observing, in the ΔE-detectors, a narrower distribution (better resolution) when projecting onto the front-energy axis than projecting onto the back-energy one. Thick E-detectors show a comparable width in both sides, though, giving pretty circular distributions. The valley due to the faulty Mesytec setting is observed through all this plane, affecting both sides equally and independently and, besides them, features involving events out of the diagonal, which correspond to charge-sharing events, are discussed in the following section.

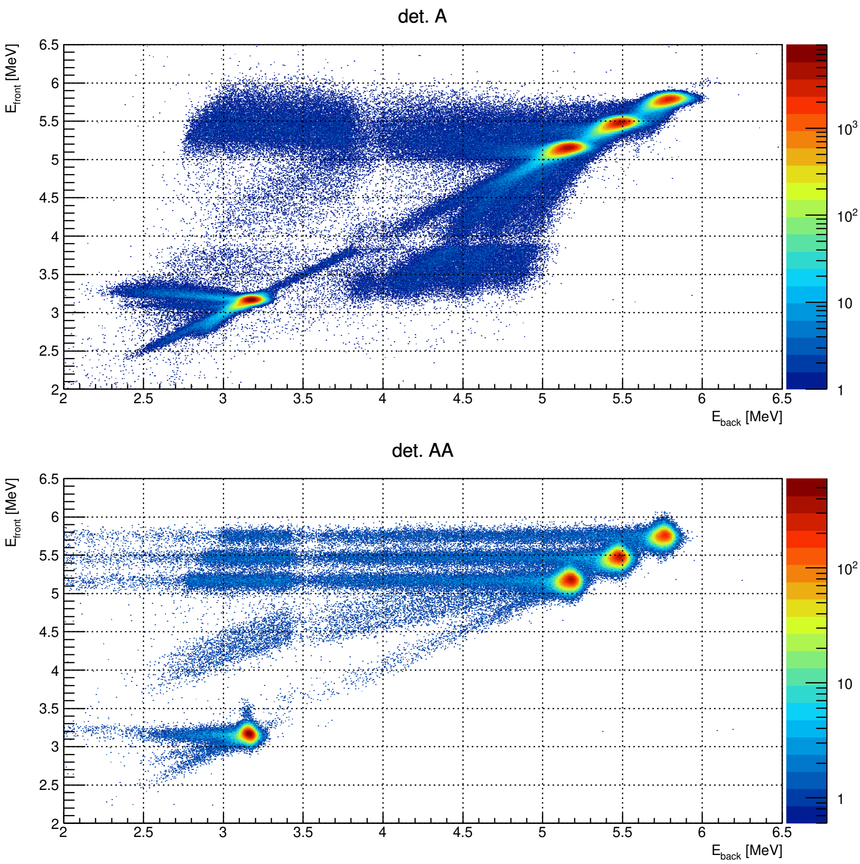

Figure 5.3: Front versus back energies of the calibrated and matched events in detectors A (ΔE-stage, top) and AA (E-stage, bottom) for the 4$\times\alpha$ source.

5.3 Calibration extrapolation

In principle, alpha calibration (per strip) is applied to all data as a first approximation. Having $\sim$ 60 MeV dynamic ranges, when the last alpha emitter is below 6 MeV, implies a large extrapolation of the lines and, consequently, possible inconsistencies at high energies. The inaccuracy of such extrapolation is observed when comparing the energies in the front and back sides of the detectors, as it is shown in Fig. 5.3. There we observe the alpha spectra calibrated by itself, so the agreement is perfect (it is just a check of the goodness of the fits and the linearity of that range) and from it we obtain the intrinsic resolution of the detector. But this time and in order to appreciate the differences between sides better, the difference $E_{front} - E_{back}$ will be plotted versus E_{front}, as shown in Fig. 5.4.

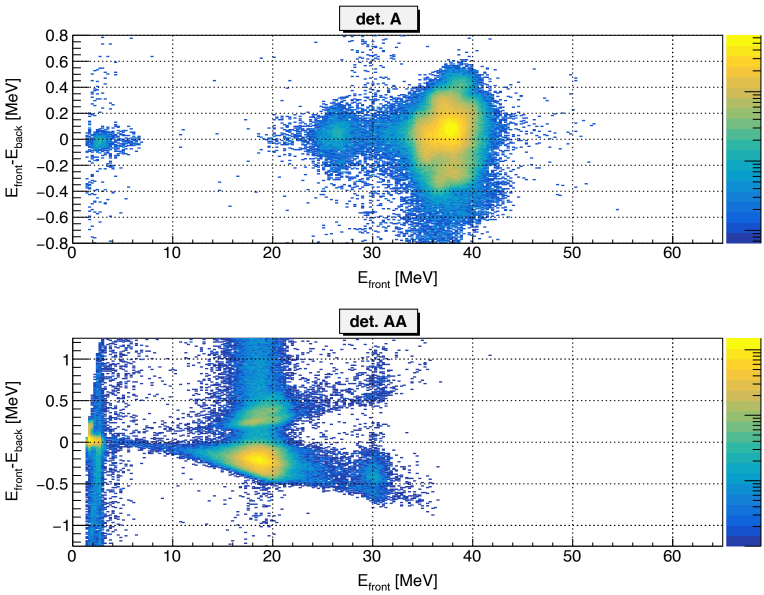

Figure 5.4: Front minus back energies versus front energy for all pixels in detectors A (top) and AA (bottom). Data from elastic scattering of ^{15}N+^{15}C with the alpha calibration applied.

We observe the energies of the elastically scattered ^{15}C and ^{15}N given by the extrapolated alpha calibration. This representation illustrates, for a given energy on the front side, the disagreement with the energy on the back side. If the agreement is perfect (not necessarily being a good value of the energy) the spot would lie in the $E_{front} - E_{back} = 0$ line, meaning front energy equals back energy. What it is found is that the alpha calibration line for every strip wrongly extrapolates at high energies and, what is more, all they change their trend in a different way. This results in as many different spots in this plot as combinations of different calibrations are, i.e. 16×16=256 (one per pixel). It is noticeable how the differences in energy between sides increase as the energy does, diverging from the $E_{front} = E_{back}$ value of the low-energy part (it is properly calibrated with the alpha source) as we reach the end of the dynamic range. This dispersion reflects a lack of linearity in the electronic chain throughout the complete dynamic range but, the fact that the spectra depart from the $y = 0$ line apparently in a linear way, also indicates that a good approximation to the real situation could be a piecewise function made of two linear calibrations: one for low energies up to 6 MeV (the alpha calibration works in its own range) and another one (yet unknown) for higher energies, which will be discussed later.

Hence, if we want to use the alpha calibration for the whole dynamic range, two important concerns need to be taken into account: one of them related to the front-back dispersion, making necessary to allow large differences in the energies of the sides in order to include the good physical data; and the other one related to the real value of the energy of a hit, which does not have to coincide with none of the values of the sides, since there is no energy reference once the calibration line has changed from the one given by the alpha-source. We do not know how much the observed energies deviate from the real values yet, but we know the disagreements between sides is kept around ± 1 MeV for telescope A, which is not really worrying since it is less than a 2% of the total dynamic range and, furthermore, it is a value close to the experimental resolution caused by the reaction target. In conclusion, despite having almost 60 MeV dynamic ranges, the use of the alpha calibration is a rather good first step that allows for a reasonable energy matching between the detectors sides, something which is crucial for the following analysis.

Notice that setting an energy tolerance for detector A of ±0.1 MeV because it is a good choice for the alpha spectra would mean a loss of all the elastic ^{15}N data at ∼ 35 MeV in some pixels due to the disagreement in the extrapolation of the alpha calibrations of the two strips that define the pixel. In summary, the energy tolerance needs to be set in terms of the dispersion observed in Fig. 5.4 in order to not lose good physical data. The cost of leaving a tolerance much larger than the intrinsic resolution of the detector is discussed in the following section.

5.4 Charge sharing

Charge sharing events are defined as those events where the produced charge has been collected by two adjacent strips on, at least, one side of the detector. They occur when a particle hits inter-strip regions, where the electric field shows bifurcations towards charge collectors belonging to different strips.

In Fig. 5.3, charge sharing events are identified out of the diagonal. In ΔE detectors, main branches depart from the full-energy peaks towards lower energies in both front and back sides. When the full energy of an alpha emitter is detected on the front side but only a fraction on the back side, we talk about back-side charge-sharing events. The previous plots are obtained after the matching process so the only signal on the front side has been paired with the signal of the back side closest to the full energy value, leading to the horizontal branches in the upper triangle of the figure. On the other hand, when charge sharing occurs in the front side of ΔE detectors, similar branches are found but, this time, deviating from the vertical. This fact means that the charge on the back side is not completely collected if the sharing effect occurs in front strips, increasing this deficit of the observed back energy as the fraction of sharing approaches a ratio 1/2. In thick E-detectors, even more curious effects are found, since no front-side charge-sharing occurs at all and more branches (despite having lower intensities) with different directions are observed on the other side. All these charge sharing phenomena in DSSD detectors are explained in terms of the inter-strip volume itself and the geometry of the electric field lines in it [52, 53, 54]. Nonetheless, if the charge sharing in the alpha source files are more or less understood with the current knowledge published in literature, at higher energies new phenomena appear with stranger consequences. The danger then lies in the appearance of discrete spots in the two-dimensional mass spectra (ΔE vs. E plots) of the telescopes that might be confused with reaction channels.

The amount of charge-sharing events is expected to be proportional to the inter-strip gap surface for a uniformly irradiated detector, i.e. about 3% of the total hits. This is most of the times a non-negligible amount that has to be considered in the analysis and hence the cleaning of charge sharing events is a major task that can be tackled in different ways.

In view of Fig. 5.3, one could think of removing events far from the diagonal from this plot (and hence from the matched data) in order to clean all charge-sharing effects. Indeed, this is frequently done in DSSD analysis. Setting an energy tolerance between front and back sides of the detector with a value comparable to the intrinsic detector resolution keeps all events with equal front and back energies. Just few charge sharing events near the full-energy peaks, where the fraction of sharing is close to 100% on one side, might have matched the full energy signal on the other side and remain in the data leading to a little widening, fact that is probably masked by the resolution of the detector and has no further relevance. This way of cleaning is pictured in Fig. 5.5, where a main peak around front equal to back energy is found. A matching tolerance is set based on the width of this peak, which depends on the intrinsic resolution of the detector, and the rest of events out of the allowed region are discarded, as they must come from either charge sharing or other spurious coincidences between the detector sides.

However, at energies far from the alpha-source range, charge-sharing phenomena get more complicated. Events under the $E_{front} = E_{back}$ diagonal are found and these cannot be removed with an energy tolerance window. A step previous to the energy matching needs to be applied by imposing no adjacent strips are hit. This introduces the extra risk of determining whether one of the two contiguous signals is noise or just a little fraction of the shared charge. A variable noise threshold can be set in order to differentiate the two possibilities. Results are ambiguous in noisy data but straightforward otherwise.

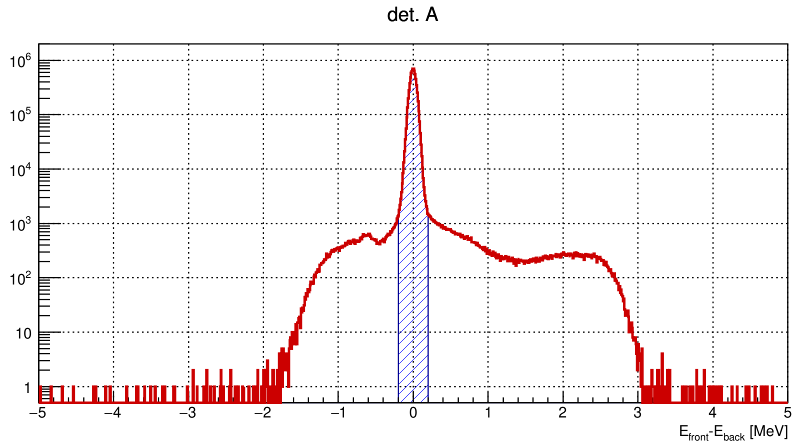

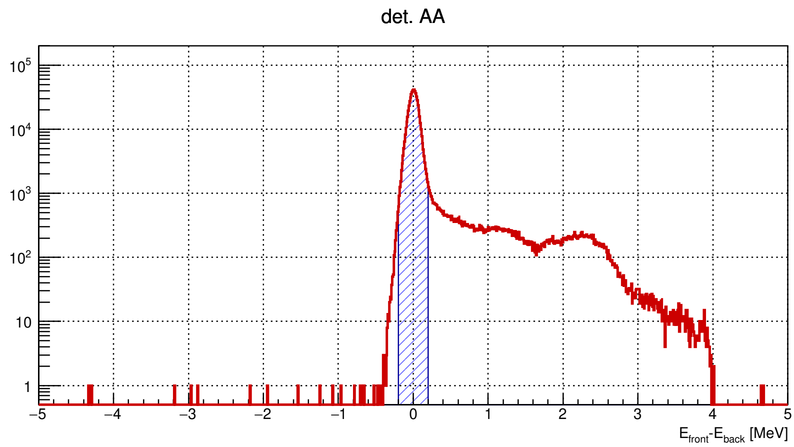

Figure 5.5: Front minus back energy of the calibrated and matched events in detectors A (ΔE-stage, top) and AA (E-stage, bottom) for the $4{\times}\alpha$ source. Dashed blue region indicates the energy matching tolerance allowed for each detector in order to remove charge-sharing events. A $\pm$ 200 keV tolerance is chosen for detectors in telescope A according to these plots.

5.5 Energy resolution

The observed experimental resolution is dominated by the straggling in the reaction targets, whose thicknesses lead to 1-2 MeV wide elastic peaks depending on the observation angle, according to the Monte Carlo simulations. The energy profile of the beam and the intrinsic resolution of the silicon detectors also contribute to this widening to a lesser degree. These factors cause a very limiting separation between ^{14}C and ^{15}C in the mass spectra. When a continuum energy distribution is simulated, for an angular sector, the two nuclei are barely distinguished, as seen in Fig. 5.6, where the separation between the maxima of the two spectra is lower than the width of the distributions at half the maxima.

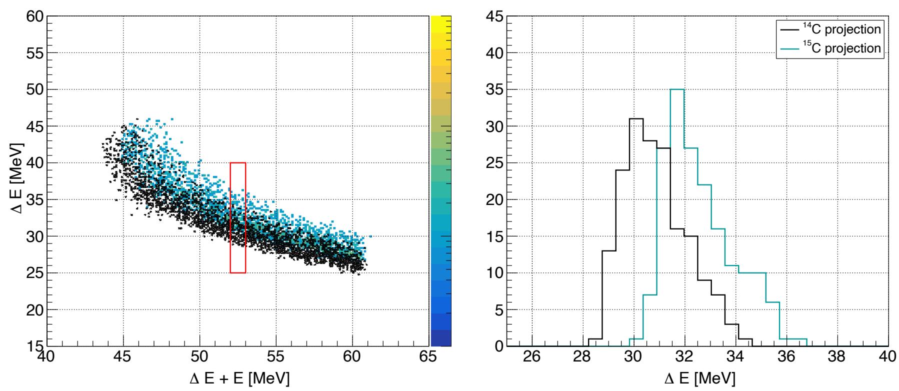

Figure 5.6: Simulated ^{14}C and ^{15}C with continuum energy distributions for an angular sector centered at 32.3° in telescope A. To the left: mass spectra of the angular sector. To the right: projection onto the ΔE-axis for the total energy range that is framed in red.

We assume then that, unless the total energy of the two carbon isotopes is clearly different, it is not possible to resolve the ^{14}C channel from the ^{15}C one with this resolution conditions. Despite it is mainly due to the target straggling, a different ΔE detector thickness would also help to separate the different bananas along the $y - axis$.

5.6 Channeling

When a particle punches-through a silicon detector with a lattice structure, the so-called channeling effect might arise in the energy spectrum. If a particle trajectory coincides with one channel of the lattice, its interaction with the silicon atoms decreases and, thus, the deposited energy is lower than the expected value predicted by the Bethe-Bloch formula. The reduction in energy deposition depends on the direction of the silicon channel with respect to the particle trajectory but such detailed information about the structure of the detectors is hardly known. That is why this effect needs to be treated empirically and many times it is not even taken into account in Monte Carlo simulations.

The overall effect on an energy spectrum is a continuously decreasing distribution from any peak towards energy zero. For typical silicon detectors the ratio of particles that undergo channeling creating this low-energy tail is frequently around a 2% and should be integrated as part of the reaction channel from where it comes. The amount of channeling is usually negligible, but not in our case, where ^{15}C is also a 2% of the ^{15}N yield and both elastic channels reach to overlap in some situations.

The ΔE vs. ΔE+E mass spectra for two selected pixels in the E-stage of telescope A is illustrated in Fig. 5.7. The left plots are obtained from data with the pure ^{15}N beam on the thick 2.1 mg/cm^2 ^{208}Pb target, hence everything observed is elastically scattered ^{15}N. The right ones, however, are obtained from data with the ^{15}N+^{15}C beam on the same target. A fixed squared region where elastic ^{15}C is expected to be found is drawn in red. For some pixels, the ^{15}N channeling distribution departing from the main elastic peak extends far enough through the ΔE axis. Nitrogen counts are found in this square framed region. Such counts are dangerous since they overlap with the elastic ^{15}C channel and contribute to the integration of the region. Notice that two events in the same position in the mass spectra are indistinguishable; it is impossible to say whether one is ^{15}N suffering channeling or just ^{15}C with a standard energy deposition.

The mass spectra for every pixel using the ^{15}N beam are integrated and, dividing the counts that are found in the ^{15}C region by the total number of counts of the plot, the *channeling factors* are obtained. The obtained values are shown in Fig. 5.8 as a map of pixels, where the color indicates how large the factors are and they reflect the fraction of elastic ^{15}N that undergoes channeling and consequently show up in a conflictive region that would correspond to elastic ^{15}C events.

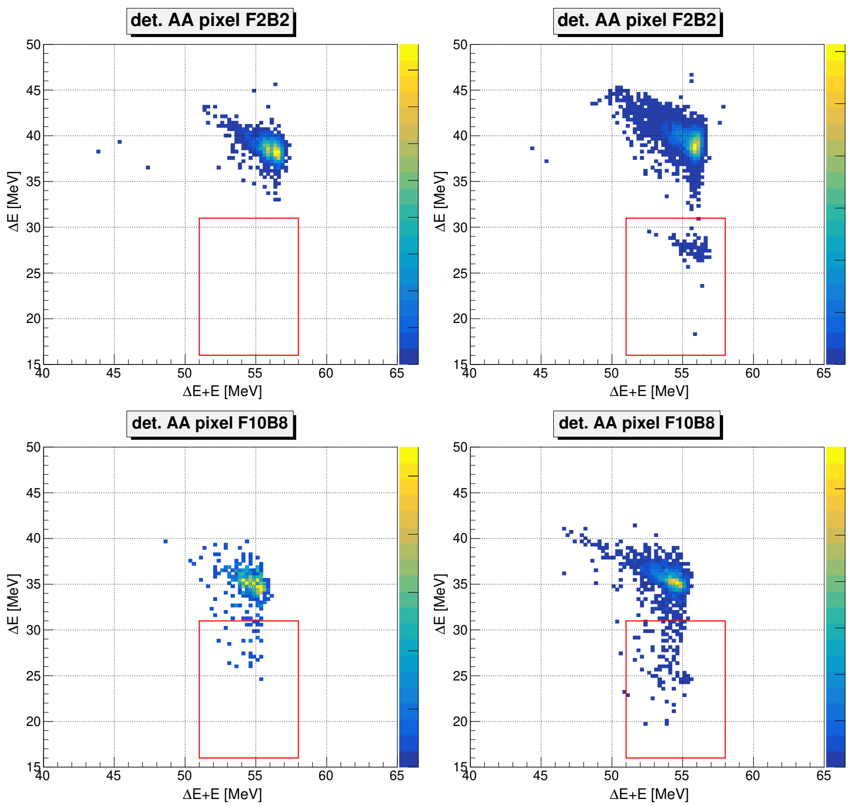

Figure 5.7: Mass spectra for two pixels selected in detector AA and for two beams. To the left: data with the pure ^{15}N beam. To the right: data with the ^{15}N+^{15}C beam. In the top: pixel F2B2, where the little ^{15}N channeling effect allows for a perfect ^{15}C separation. In the bottom: pixel F10B8, where the huge ^{15}N channeling effect prevents ^{15}C from being distinguished among the ^{15}N channeling counts. The red box indicates the region where elastic ^{15}C is expected in this telescope. 2.1 mg/cm^2 target used.

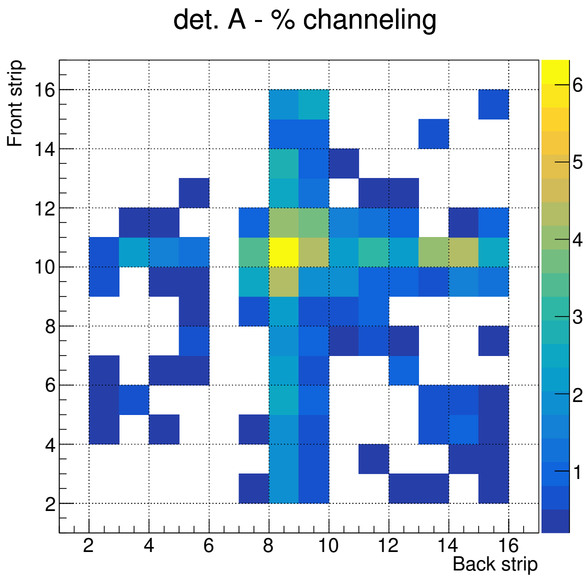

Figure 5.8: Channeling factors for detector A pixels showing the fraction of elastic ^{15}N undergoing channeling and getting into the elastic ^{15}C region in the mass spectra.

It is found that the channeling effect shows a maximum in pixel F10 B8, reaching more than 6% of elastic ^{15}N undergoing channeling. Strips F10 and B8 are largely affected and out of the cross delimited by these strips the effect is minor. Since channeling is understood as a geometric effect enhanced whenever the silicon lattice channels coincide with particle trajectories, taking into account our setup geometry and, assuming that the silicon lattice is more or less uniform through the whole detector, it is understandable that there is one direction (the one given by pixel F10 B8) where such coincidence is the greatest and, getting far from it, the effect vanishes. The inhomogeneities we find in Fig. 5.8 must reflect changes in the silicon lattice.

Regarding the amount of ^{15}N undergoing channeling, it is seen that it goes from 0 (no effect) up to 6%, what is a rather large ratio in any circumstance. Furthermore, reminding that the provided beam comes with an abundance ^{15}C/^{15}N$\sim$2%, the channeling of ^{15}N turns out to be even more relevant, since it clearly exceeds the amount of ^{15}C in some pixels. Not considering this effect would create an overestimation of carbon in the directions where the channeling is favoured. Notice that the *channeling factors* do not depend on the nucleus, so they have to be identical for ^{15}C. They only depend on the position of the reaction point with respect to the setup, which determines the direction of the outgoing particles from the reaction to the detectors (and their lattice channels).

To face the ^{15}C overestimation issue due to the channeling of ^{15}N we propose two alternatives: one is the subtraction of the channeling background and the other is the discard of those pixels whose channeling background is too large. Both methods will be based on the *channeling factors* obtained above. In the first one, the background is calculated for every pixel by scalating the amount of elastic nitrogen out of the channeling region with its corresponding factor. Then the whole channeling region is integrated and the background is extracted. The scarce statistics to obtain the *channeling factors* (about 10 counts of ^{15}N per pixel in the channeling region), however, leads to large uncertainties in the subtraction ($\sqrt{10}$ $\sim$3, hence a 30% of error), what in many cases creates negative counts or yet an excessive number of ^{15}C after computing the correction. The result is an increase in the data dispersion and in the statistical error bars so the method is soon discarded. In the second method, the channeling factor of every pixel is compared to the carbon abundance in the beam, which is 2% in average. Those pixels whose channeling factor is greater than a tenth part of the carbon abundance, i.e. 0.2%, are considered potentially dangerous since they are showing the same order of magnitude in the counts of elastic ^{15}C and ^{15}N inside the channeling region. These are all removed, reducing considerably the statistics but ensuring a good ^{15}C selection. The error bars will increase due to the decrease of statistics but no extra errors are introduced, being this the preferred situation.

5.7 Geometry optimization

Despite the efforts dedicated to the alignment of the chamber and the setup with respect to the facility beam line, a little shift of the reaction point (intersection between beam and target) and/or a little tilt of the beam direction are always expected. Small variations in the position of the detectors respect to their ideal designed configuration are also possible. All these small deviations introduce changes in the angles θ,φ and solid angles Ω of the detector pixels and introduce a relevant dispersion in the data when looking for any angular distribution of particles. The search of the optimum angles and solid angles for every detector is referred to as the geometrical optimization (or geometric calibration) and, in this case, will be performed by looking for the best ^{15}N Rutherford distribution, i.e., the case with minimum χ^2.

Often, the shift in the position of the reaction point, which ideally is the origin of coordinates $\vec{r} = (0, 0, 0)$, is the most important factor in the geometric optimization. Hence, a new set of cartesian coordinates defining its position respect to the origin $\vec{r}_{RP} = (x_{RP}, y_{RP}, z_{RP})$ has to be found. Since there is a 10 mm diameter entrance collimator at the end of the beam line and right before the chamber, the accepted shift will not be larger than ±5 mm around the origin. Sometimes, this shift is not enough to flatten the ^{15}N Rutherford distribution and little tilts need to be considered around the detector axes in order to consider imprecisions in their positions. Three angles $(\alpha_{det}, \beta_{det}, \gamma_{det})$ define these tilts around their respective inertia axes. Furthermore, a beam tilt could also play a role, described by two angles $(\alpha_{beam}, \beta_{beam})$ that define the direction of the beam respect to the z-axis and, thus, determining the symmetry axis of the reaction (a third angle around the symmetry axis is meaningless). However, in this case, since the distance from the last beam line collimator to the reaction target is so large (above 1 m), deviations lower than 0.5° are expected, which are negligible, specially if detector rotations are considered, which turn out to be much more relevant.

The data to fit are the hit patterns of our detectors, which show the number of elastic ^{15}N measured in every pixel and should unequivocally determine the geometric situation of each detector respect to the beam direction and position of the reaction point. In the ideal case where the reaction point is the geometric center of the setup, the beam direction is exactly the z-axis and the detectors are placed in their ideal position, the angles that define every pixel in the setup, on the $\theta - \varphi$ plane, would be the ones shown in Fig. 5.9. With these angles (and the solid angles associated to them), however, it is not found a proper Rutherford angular distribution; there are discontinuities between detectors and broad distribution of points, what indicates the need of a geometric optimization.

With the angles and solid angles calculated from a possible geomet-

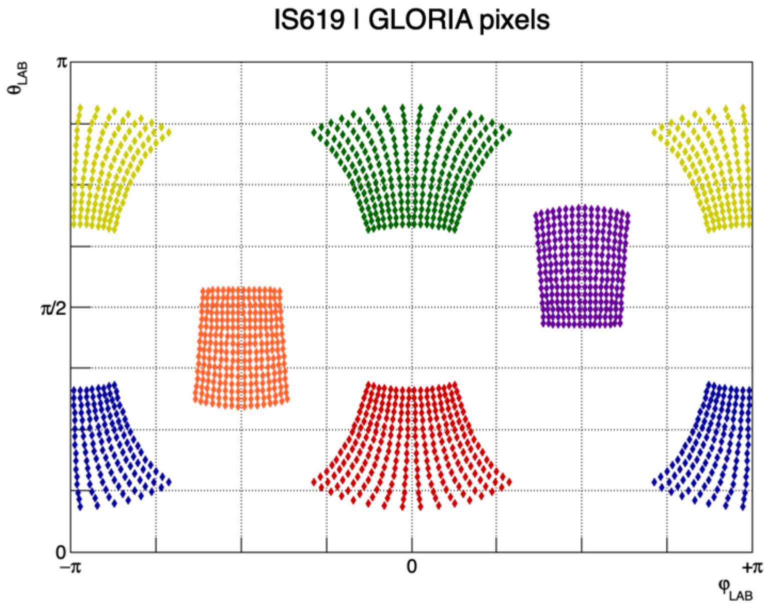

Figure 5.9: Angles θ, φ for every pixel of the ΔE detectors assuming the reaction point at $\vec{r} = (0, 0, 0)$ and the beam direction along z-axis. Detector A in red, B in blue, C in light green, D in dark green, F in orange and E in purple.

ric configuration, the observed number of ^{15}N counts (N^{obs}) in every pixel is compared to the expected value N^{exp} given by the Rutherford formula

$$N^{exp} = I_{beam} \cdot t \cdot \sigma_{Pb} \cdot \frac{d\sigma_{Ruth}}{d\Omega} \cdot \Delta\Omega \tag{5.1}$$

Being I_{beam} the beam intensity, t the measurement time (after dead time correction), σ_{Pb} the superficial density of scattering centers facing the beam, $d\sigma_{Ruth}/d\Omega$ the Rutherford differential cross section and $\Delta\Omega$ the solid angle of the pixel. Notice the dependence on θ of the Rutherford cross section, that σ_{Pb} depends on the thickness of the target, that the intensity I_{beam} fluctuates through the experiment and hence is an averaged value and that this expression is given in the CM frame.

Then, all observed and expected values are compared pixel by pixel and the χ^2 value, normalized by the number of degrees of freedom, is calculated as

$$\frac{\chi^2}{dof} = \frac{1}{N-1}\sum_i \frac{(N_i^{obs} - N_i^{exp})^2}{N^{obs}} \tag{5.2}$$

The values of σ_{Pb} and live time t for each target measurement are shown in the following table

Table 5.2: Thickness, superficial density of scattering centers facing the beam and live time of measurement with each ^{208}Pb target with ^{15}C(+^{15}N) beam.

Target thickness	Scattering centers σ_{Pb}	Live time
2.1 mg/cm^2	$7.03{\cdot}10^{22}$ m^{-2}	396257 s (110.1 h)
1.5 mg/cm^2	$5.01{\cdot}10^{22}$ m^{-2}	121298 s (33.7 h)

Where the live time has been computed from the number of total versus accepted triggers. The superficial density of scattering centers σ_{Pb} is approximated as the number of atoms per volume n_{Pb} times the effective length (facing the beam) of the target l_{eff}, what is expressed in terms of the volume density of lead ρ_{Pb}, the Avogadro constant N_A and the atomic mass A of ^{208}Pb. The effective length is the target thickness divided by $\cos(30°)$ in order to correct the tilt respect to the beam direction.

$$\begin{aligned}\sigma_{Pb} = n_{Pb} \cdot l_{eff} = \rho_{Pb}\frac{N_A}{A} \cdot l_{eff} = \\ = 11.38\frac{g}{cm^3}\frac{6.02 \cdot 10^{23}}{208}\frac{mol^{-1}}{g \cdot mol^{-1}} \cdot l_{eff} = \\ = 3.29 \cdot 10^{28}\ \mathrm{m}^{-3} \cdot l_{eff}\end{aligned} \quad (5.3)$$

Being $l_{eff} = 1.32 \cdot 10^{-6}/\cos(30°)$ m in the case of the thin target and $1.85 \cdot 10^{-6}/\cos(30°)$ m in the case of the thick one.

On the other hand, $d\sigma_{Ruth}/d\Omega$ and $\Delta\Omega$ for every pixel are calculated for every attempted geometric configuration.

$$\begin{aligned}\frac{d\sigma_{Ruth}}{d\Omega} = \left(\frac{1}{4\pi\epsilon_0}\frac{Z_1 Z_2 e^2}{4E}\right)^2 \frac{1}{\sin^4(\theta/2)} = \\ = \left(\alpha\hbar c \cdot \frac{Z_1 Z_2}{4E}\right)^2 \frac{1}{\sin^4(\theta/2)} = \\ = \left(\frac{197}{137} \cdot \frac{7 \cdot 82}{4 \cdot 60.62}\right)^2 \frac{1}{\sin^4(\theta/2)}\ \mathrm{fm}^2\end{aligned} \quad (5.4)$$

Where α is the fine structure constant $\approx 1/137$, $\hbar c = 197$ MeV·fm and $E = 60.62$ MeV is the energy of the system in the CM frame ($E_{lab} = 65$ MeV). The resulting units of the cross section are fm^2, equivalent to 10^{-2} b or 10^{-30} m^2.

The beam intensity I_{beam} is not known accurately and, if one tries to leave it as a free variable during the optimization, might find convergence troubles. For instance, letting vary the intensity I_{beam} together with the coordinates of the reaction point (X_{RP}, Y_{RP}, Z_{RP}), it gives the χ^2 trend over the $I_{beam} - Z_{RP}$ plane shown in Fig. 5.10, meaning that the algorithm does not find a minimum.

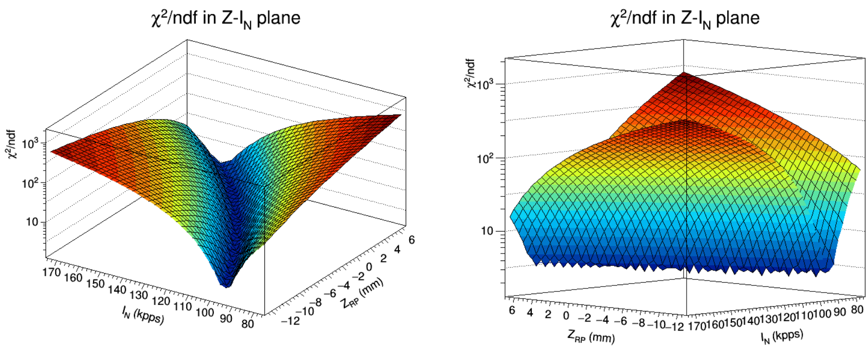

Figure 5.10: χ^2 surface over the $I_{beam} - Z$ plane under two different perspectives. A valley of minima is found, meaning that for a given I_{beam} there is a value of Z leading to a Rutherford fit of the hit maps with χ^2 close to 1.

Fig. 5.10 shows that the parameters I_{beam} and Z_{RP}, despite not explicitly, are closely related in Eq. 5.2. For any beam intensity there exists a Z_{RP} position of the reaction point giving an equally good Rutherford fit of the hit pattern than infinite others (from the χ^2 point of view). Thus, it is needed to fix either the beam intensity or the Z_{RP} coordinate in first instance. The shift in Z_{RP} is expected to be lower than ± 5 mm due to the inaccuracy hanging the target ladder by hand in the setup. The fluctuations of the beam yield were observed to be rather large, making difficult to get an averaged value during the measurement time. Consequently, it seems preferably to fix $Z_{RP} \approx 0$ and find a proper value of the intensity, checking later that the ± 5 mm uncertainty translates into a reasonable error of the intensity better than the vague information we have about it. Furthermore, we can assume that the optimization of each detector separately leads to different X_{RP} and Y_{RP} coordinates since their positions might differ a little from the ideal designed positions, however, the intensity I_{beam} should be the same for all of them. For this purpose, and since our knowledge about the beam intensity is so scarce, it is convenient firstly to find a value of I_{beam} giving a good agreement between the detectors in the setup. It is possible to do so taking advantage of the fact of having several detectors, assuming in first instance that they are perfectly placed in their ideal positions, and letting vary the coordinates X_{RP} and Y_{RP}, determining Z_{RP} consequently. Using detectors A and B, which cover forward angles from 15 to 65° (the huge change in the Rutherford formula at low angles makes them more effective), the code clearly converges with a sensibility greater than 0.1 mm. This is less than the size of the spatial profile of the beam (expected to be of few mm), so the result exceeds the required accuracy. The χ^2 surface over the $X_{RP} - Y_{RP}$ plane and the angular distribution of the intensity observed from every pixel in the minimum are shown in Fig. 5.11.

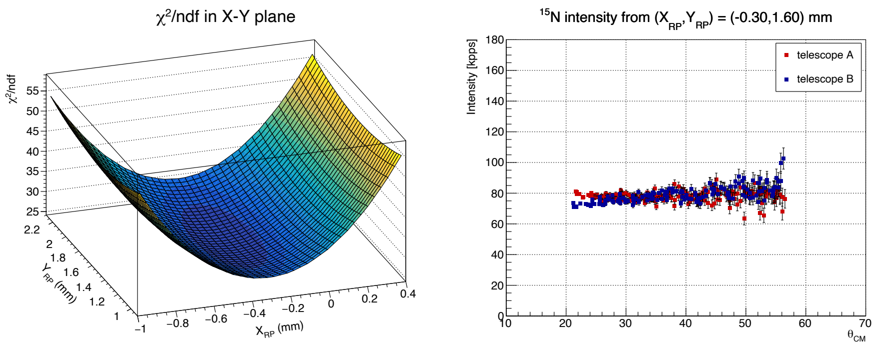

Figure 5.11: To the left: χ^2 surface over the $X_{RP} - Y_{RP}$ plane fitting the ^{15}N beam intensity observed from pixels in telescopes A and B. To the right: the angular distribution minimizing the χ^2. All files with the 1.5 mg/cm^2 (thin) target. The two telescopes are assumed to be in their rigid designed configuration.

The deduced averaged ^{15}N intensities during the measurements with both targets, the minimum χ^2 and the position of the reaction point in each case are shown in the following Tab. 5.3.

Table 5.3: Averaged ^{15}N beam intensity, minimum χ^2 and reaction point position (X_{RP}, Y_{RP}) found for each target measurement.

Target	(X_{RP}, Y_{RP})	^{15}N intensity	^{15}C intensity
2.1 mg/cm^2	(0.3, -0.3) mm	$5.57{\cdot}10^4$ pps	$0.96{\cdot}10^3$ pps
1.5 mg/cm^2	(-0.3, 1.6) mm	$7.86{\cdot}10^4$ pps	$1.42{\cdot}10^3$ pps

The reaction point coordinates for each target are obtained from the ^{15}N data, which are more reliable due the larger statistics. It is observed that the position differs a little for the two target positions, something understandable within these limits. The fluctuations in the beam intensity throughout the experiment are clear in the deduced values for each target measurement. Despite everything, the consistency in the abundance ratios and the agreement between these both telescopes are satisfactory enough for a good angle and solid assignation to every pixel.

Besides this, it is evident there is a little disagreement between telescopes A and B, meaning it is needed some relative freedom in their position respect to the nominal configuration that can be corrected. It turns out that telescope B needs a $3°$ tilt respect to its own y-axis in order to reproduce a flat ^{15}N Rutherford distribution. This tilt is determined following the same procedure of minimizing the χ^2 value the fit once the averaged intensity and the $x-$ and $y-$ coordinates of the reaction point have been chosen assuming a rigid (nominal) configuration of the setup. With these and the new tilt applied over telescope B, the consistency in the geometry and intensity is kept and the agreement between the two telescopes hugely improves, as it can be seen in Fig. 5.12. Same method is applied over 2.1 mg/cm^2 target data. This little discrepancy respect to the nominal position might describe just the use of a thicker washer in the support of the detector and it is seen how it needs to be corrected in order to get a good agreement between the symmetric detectors and proper flat Rutherford distribution of ^{15}N in telescope B.

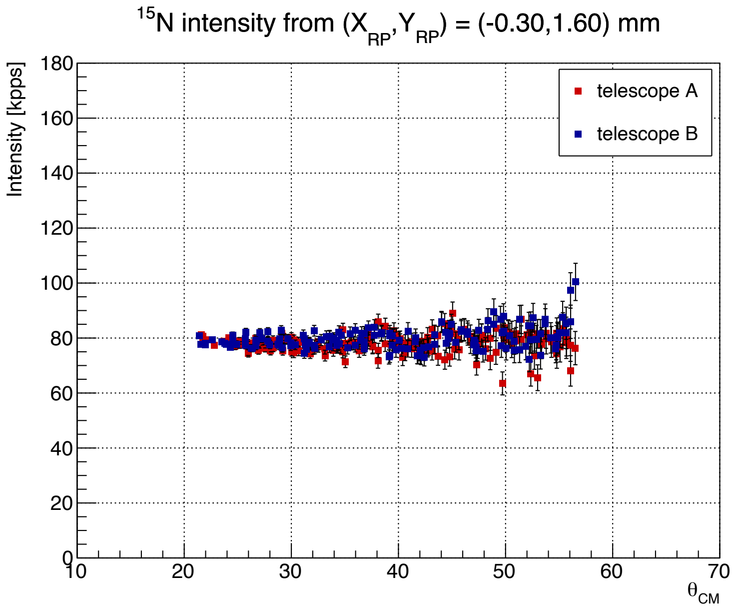

Figure 5.12: ^{15}N angular distribution observed from pixels in telescopes A and B with the 1.5 mg/cm^2 target data. Optimized position of the reaction point assuming a rigid configuration of the two telescopes plus a 3° tilt around telescope B $y-$axis. This relative degree of freedom is seen that needs to be allowed in order to get a proper flat Rutherford distribution in telescope B and a good agreement with telescope A.

Once the geometry is optimized and the assignment of scattering angles and solid angles for every pixel is made, it is tested for ^{15}N in the full angular range, in order to ensure that a Rutherford behavior is found, as expected and guarantee that it can be use to normalize ^{15}C data afterwards. The result is seen in Fig. 5.13. Some statistical fluctuations are observed from 60° onwards.

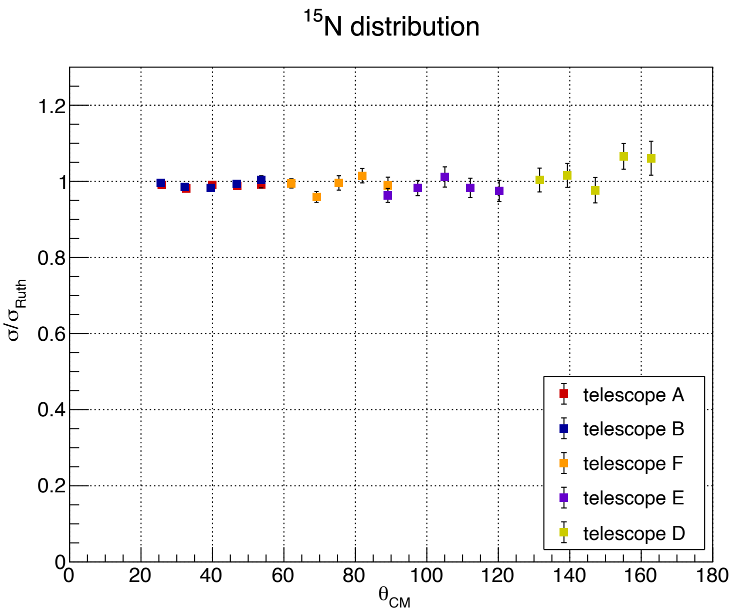

Figure 5.13: ^{15}N angular distribution averaged in 5 angular sector per telescope observed in all working detectors of the setup. Data for the 1.5 mg/cm^2 target. The expected Rutherford distribution is observed.

5.8 Mass spectra construction

The use of DSSD as both ΔE and E-detectors of the telescopes allows for two different methods in the construction of the mass spectra, depending on the stage (ΔE or E) in which pixels are selected. If one pixel is fixed in the ΔE stage, the E-stage detector then is treated as a non-segmented pad (it can be checked that counts will be distributed in set of $\sim$4 pixels behind the ΔE pixel). Then, the angle and solid angle associated to those events will be the one of the fixed pixel, which is the one that constrains the selection. In telescopes A and B, it is preferable to choose the pixels in the E-stages (which have some dead strips), since all strips are alive in the ΔE detectors and, when looking for multiplicity 2 events, we avoid the problem of the missing hit due to the dead strips. In the other telescopes, however, it is better to choose pixels in the ΔE-stage, since ^{15}N does not completely punch through such detector and sometimes lead to multiplicity 1 events that need to be considered. Some examples of mass spectra for the final angular sectors are shown in Fig. 5.14. They are built by selecting the pixels (and hence angles) in the ΔE stage and imposing multiplicity 2 (i.e., multiplicity 1 in the ΔE-detector and multiplicity 1 also in the E-detector of the same telescope). Strip front-11 is dead in telescope F, as well as front-4, front-5 and back-8 in telescope E. The empty pixel in the sector of telescope D is alive but has measured 0 counts, so its solid angle will contribute to the results. In the figure of telescope F, where nitrogen barely stops in the ΔE stage and its distribution can be clearly appreciated, it is seen an evident ^{15}C region which also shows the same aspect, as it is expected for any elastically scattered nucleus. At these angles, the channeling overlap, whose effect is proportional to the amount of nitrogen, becomes less important, so it should not be worrying during the integration. In telescopes E and D (angles above 89°), where the elastic channel is expected to show some absorption and other channels to open, nonetheless, things get more complicated. Elastic ^{15}C should exhibit the same features as elastic ^{15}N, but nitrogen's shape is not fully observed (part stops in the ΔE stage) and its shape is not well understood (very broad and flat instead of peaked spectra). This, together with the fact that ^{14}C and ^{15}C are not separable at the same energy, makes impossible to make any statement about whether ^{14}C channels are open and all we can do is perform a quasi-elastic integration of what we believe it is ^{15}C.

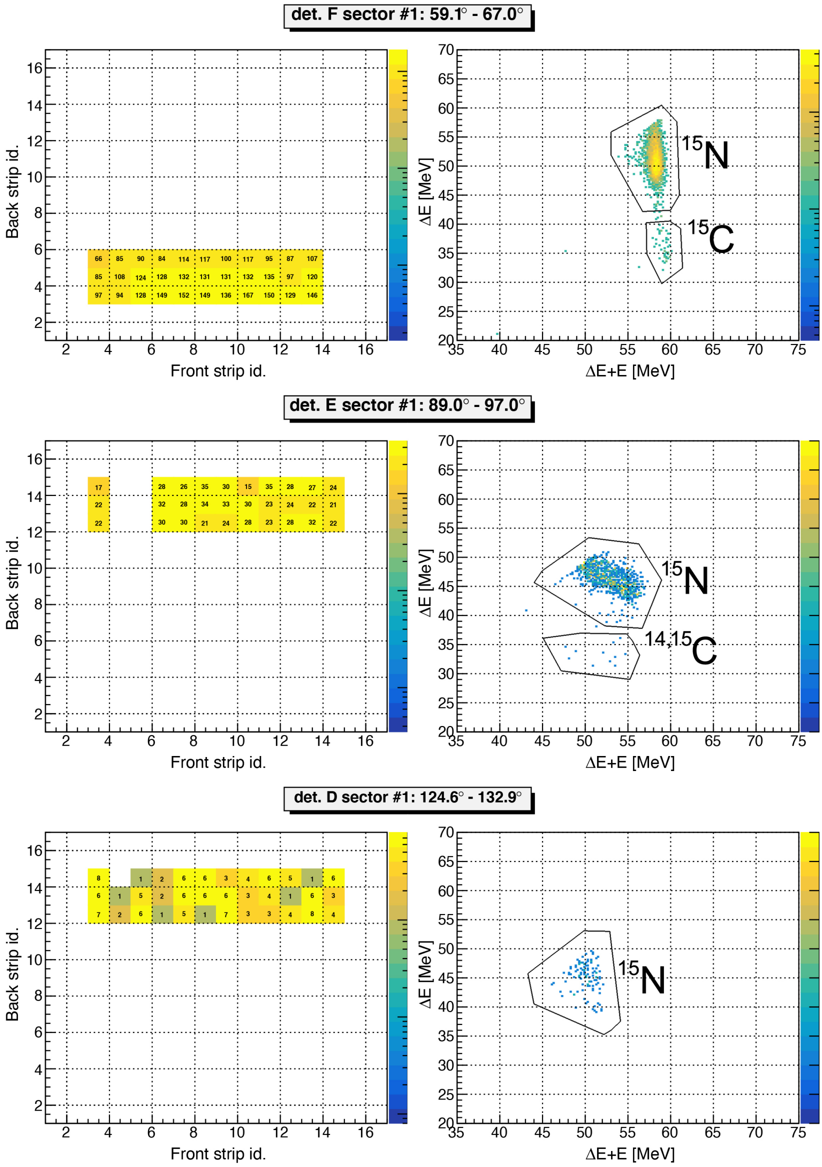

Figure 5.14: Mass spectra and hit patterns for given angular sectors. All ^{15}C on 1.5 mg/cm^2 target data. Alpha calibration and matching tolerance applied. Multiplicity 1 in both ΔE and E detectors of the telescopes.

In the first angular sector of telescope E (see middle plot of Fig. 5.14), the 9-10 carbon counts around ΔE$\approx$ 30-35 MeV are quite widespread respect to the resolution predicted by the simulation. Even they seem to be grouped in two clusters. This might indicate there exists an extra reaction channel overlapped with the elastic. But, also, the nitrogen shows an extraordinarily wide distribution for what uniquely should be an almost discrete spot of elastic scattering. In the angular sector of telescope D (bottom plot of Fig. 5.14), there are clearly no counts other than ^{15}N, but there will be in the thick target files, making the cross section not to vanish at any angle.

5.9 Further energy corrections

It's clear that the extrapolation of the alpha calibration is not good enough, as it's been discussed in the p- vs. n- plots, shown in Fig. 5.4. We can perfectly assume that the linear regression done up to $\sim$ 6 MeV with the 4$\times$alpha source differs more and more from the real energy values as one keeps getting far from the last point of the calibration. Hence, another linear calibration with different offset and slope should exist, able to reproduce the spectra in high energy regions.

On the other hand, a 20% error in the thickness of the ΔE detectors is perfectly possible according to the manufacturer. This means that for a nominal 42 μm thick detector, a 8 μm fluctuation is acceptable. For 65 MeV ^{15}N ions, it might mean energy shifts above 5 MeV. The beam energy is given by the ISOLDE team with an accuracy of 225 keV (FWHM). The dead layers and reaction target thicknesses may show also some errors, let's say of a 10%, due to incomplete depletion of the detectors or imprecisions during the manufacturing method. These uncertainties might only explain 170 nm of intermediate material which is not considered in the simulations and would not cause a difference larger than 200 keV in the expected energy losses. This is pretty below the experimental energy resolution in any case, so we conclude that the ΔE thickness must be the most important factor in the deviation of the observed energies.

The fact that all available beams during the experiment do punch-through the ΔE stage (at least in the region with large statistics, i.e. forward angles), together with the scarce information about these detector thickness and the bad behavior of the alpha calibrations when they are extrapolated to high energy regions, lead to many uncertainties about the energies that are experimentally observed. In this section different techniques are proposed in order to understand and explain the energy spectra and shed some light on the experimental setup behavior.

5.9.1 ΔE vs. E relative correction

Calibrations are firstly done strip by strip with the α-source. The change at high energies where they are extrapolated is associated to the electronic chain to which each strip is connected. Since the electronic modules accept 32 channels, a complete DSSD is connected to a single shaper amplifier and, hence, global differences from detector to detector may occur. The ΔE vs. $\Delta E + E$ plots of telescopes A and B, which cover the same scattering angles angles from 15 to 65°, and hence should look very similar (at least in the $\Delta E + E$ axis), are found to be, actually, contradictory; see Fig. 5.15.

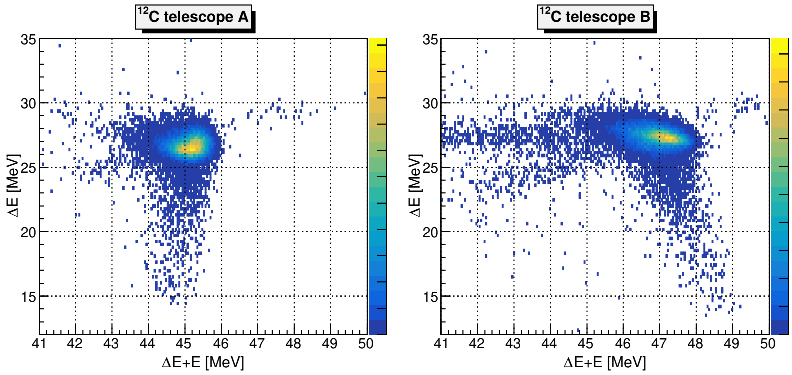

Figure 5.15: Mass spectra for central pixels (strips 6-10 on both sides) of telescope A and B with alpha calibrations. Elastic ^{12}C data on 1.5 mg/cm^2 thin target.

Telescope B shows very different total energy total energy of ^{12}C. Also, its channeling tail reaches energies higher than the elastic spot, what is unfeasible. There is a general distortion of the mass spectrum respect to the one of telescope A, which shows a vertical channeling tail, as expected. Still, the energy values from any telescope cannot be taken as good as long as the α-calibrations are used. We can ensure, however, no distortion is introduced in the mass spectrum of telescope A due to relative differences in the electronic chains of detectors ΔE and E.

If alpha calibrations are going to be extrapolated, besides being aware of the wrong energy values that they provide, this distortion has to be corrected to get a proper shape of the different reaction channels in the 2D plots. The need of such correction has already been observed in other works with similar segmented silicon detectors [12], proposing a multiplicative constant factor for the energy of one of the telescope detectors respect to the other. Here, such factor has been applied to the E-detector, which only influences the x-axis of the mass spectrum, which, hence, is built as ΔE vs. Δ E + δ·E, being δ a constant close to unity. The effect of such δ factor is appreciated in Fig. 5.16.

The correction factor is chosen according to the channeling tail, which needs to be vertical. This corresponds to a $\delta = 0.85$ (middle case in Fig. 5.16) for telescope B. In telescope A it happens to be $\delta = 1$, so no correction is needed. In general, the factor can be chosen from the pixel with the largest channeling effect and it will be valid for the whole E-detector. Once the distortion is solved, a recalibration can be attempted if one needs to obtain more accurate values of the energies. The total energy observed with the alpha-calibration together with this correction factor, i.e. $\Delta E_\alpha + \delta \cdot E_\alpha$ can be modified in order to recreate the Monte Carlo simulations. It is discussed in the following section.

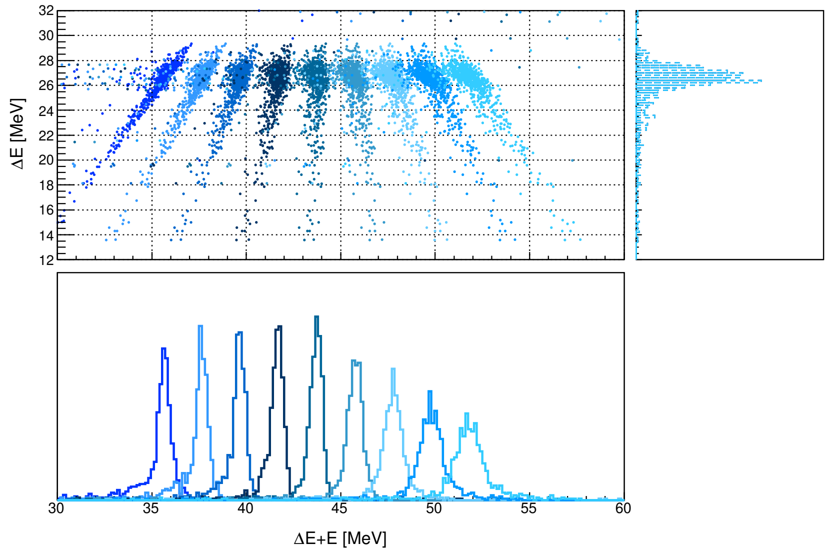

Figure 5.16: Mass spectrum and its projections for nine different correction factors $\delta = 0.45 - 1.25$. Detector BB pixel F7B8 (largest channeling tail). Elastic ^{12}C data on 1.5 mg/cm^2 thin target. All projections are normalized.

5.9.2 $\Delta E + E$ recalibration

The energy deposition of a scattered beam in each stage strongly depends on the ΔE thickness, which is unknown with a large uncertainty of a 20%, as discussed. Thus, a recalibration of the total energy $E_{tot} = \Delta E + E$ is firstly suggested, where such dependency on the ΔE thickness almost vanishes. A lower ΔE thickness means a lower energy is deposited in the ΔE detector, however, it will always be compensated with a larger value in the E-detector, where the particles stop. The position of the dead layers, which are relative to the ΔE thickness, introduce a minor but unavoidable error: it is not the same a 500 nm dead layer after 38 μm of active volume than after 42 μm in the total energy deposition. Either way, this method allows for a reconstruction of the kinetic curves, which were far from reality when using the alpha calibration and also a deep understanding of the asymmetries through the azimuthal angle φ in the energy losses.

Considering the ^{12}C and ^{15}N elastic peaks in every pixel of the E-detector, the total energy ΔE+E of each peak (any pixel of ΔE hitted) observed with the alpha calibration is compared to the Monte Carlo simulation (performed with the nominal ΔE thickness, which is 42 μm in the case of detectors A and B). Then, the ΔE+E energies are modified aiming to make coincide the experimental data and the simulations. Of course, this method is only applicable when peaks can be properly fitted, strongly limiting the angular range of application to the two forward telescopes A and B, where statistics per pixel are good enough to ensure good gaussian fits. The proposed recalibration reads as follows

$$(\Delta E + E)_{RC} = a \cdot (\Delta E_\alpha + E_\alpha) + b \tag{5.5}$$

Where the subindex α denotes those energies are observed with the α calibration and a, b are the recalibration parameters, calculated as

$$a = \frac{E_{sim}^{^{15}\mathrm{N}} - E_{sim}^{^{12}\mathrm{C}}}{E_{\alpha}^{^{15}\mathrm{N}} - E_{\alpha}^{^{12}\mathrm{C}}} \tag{5.6}$$

$$b = -(E_{\alpha}^{^{12}\mathrm{C}} \cdot a - E_{sim}^{^{12}\mathrm{C}}) = -(E_{\alpha}^{^{15}\mathrm{N}} \cdot a - E_{sim}^{^{15}\mathrm{N}}) \tag{5.7}$$

The slope a reproduces the separation of the two peaks that have been used. The offset b shifts the spectra after applying the new slope so the centroids lie in the positions obtained with the simulatons.

A comparison between the ^{15}N and ^{12}C kinetic curves observed with the α calibration and the Monte Carlo simulations are shown in Fig. 5.17. The large discrepancy between the observed and expected energies makes clear how wrong the extrapolation of α calibrations works. The experimental kinematic curves are not only several MeV below the simulated values but also show slightly different trends. A recalibration aiming to reconstruct the simulations is proposed. ^{12}C and ^{15}N data are used to get the recalibration parameters a, b, so the α-calibrated centroids are forced to coincide with the simulated ones. The total ΔE+E energy of any other beam should now be well estimated if the simulations used are realistic enough (proper energy beam, target thickness and detector positions).

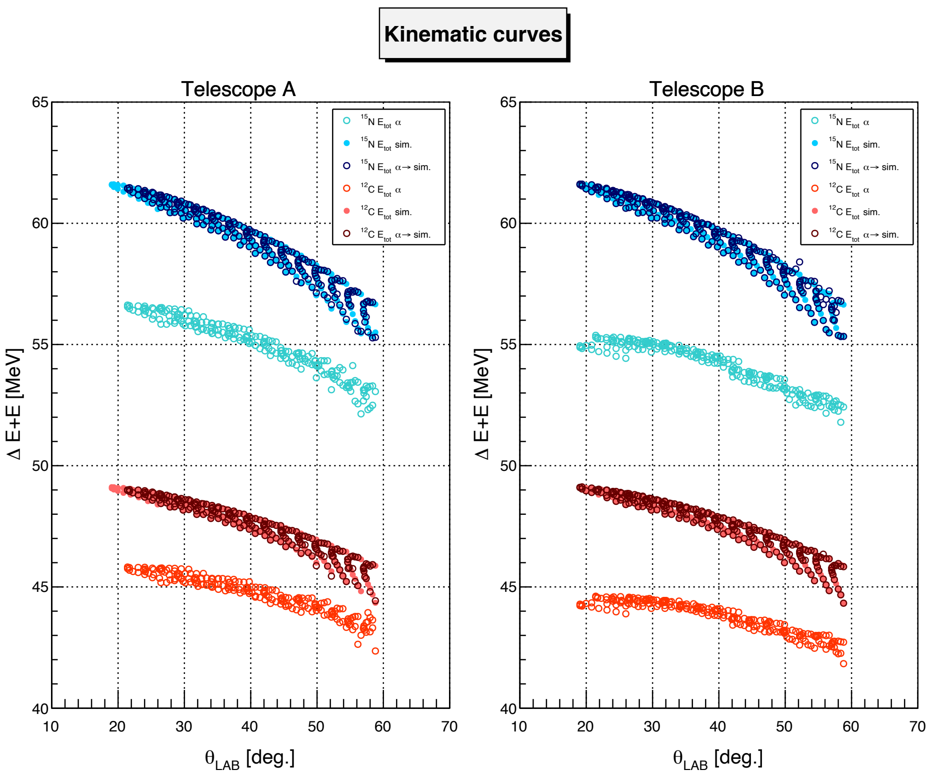

Figure 5.17: Centroids of the elastic ^{15}N and ^{12}C peaks on the thin 1.5 mg/cm^2 target in each pixel versus the scattering angle. Monte Carlo simulations (filled circles) are compared to experimental data (empty circles) with the α calibration (bright colors) and after the proposed recalibration (dark colors). Simulations with nominal thicknesses and angles.

5.9.3 ΔE thickness maps

An attempt of calibrating ΔE and E detectors separately with beams involves an intermediate step of getting the thickness of the ΔE detector. On the other hand, the fact of having segmented detectors as E-stage in the telescopes allows for a mapping of the thickness of such ΔE-detectors. The detectors are nominally 40 μm thick but it is well known and warned by the manufacturer that there might exist inhomogeneities of a 20 % at most over the surfaces. Despite not having fine calibrations (alpha calibrations are still extrapolated in the whole dynamic range), it is possible to make a rather good estimation by taking advantage of the presence of, at least, two elastically scattered beams whenever they punch-through the ΔE stage. It will be shown that the relative separation of the peaks in E-detector pixels, even with wrong calibrations, mainly depends on the thickness of the ΔE-detector that the particles have punched-through previously and, by comparing to several simulations carried out with different thicknesses, the inhomogeneities of ΔE detectors can be calculated.

We assume the slope and offset of the alpha calibration have both changed in the observation range, so it would be better not to rely on them for any energy observation. Then, at least two experimental elastic peaks (^{12}C and ^{15}N) are needed. Pixel by pixel in the E-detector, the alpha-calibrated spectrum will be compared to simulations with different ΔE thicknesses. The ΔE thickness that best recreates the ratio between the centroids of the alpha-calibrated peaks will be chosen and assigned to the closest ΔE-detector pixel. The centroids ratio must be similar for the alpha-calibrated spectra and for the simulation with the most suitable ΔE thickness. It can be shown that, for two experimental peaks (^{12}C and ^{15}N), the energies for a given alpha calibration with slope and offset a^α, b^α are:

$$E_N^\alpha = a^\alpha \cdot ch_N + b^\alpha \tag{5.8}$$

$$E_C^\alpha = a^\alpha \cdot ch_C + b^\alpha \tag{5.9}$$

Being ch_N and ch_C the channel position of the uncalibrated centroids of the peaks.

For another linear calibration, whose parameters a, b cannot be very different to the previous ones ($a \approx a^\alpha$, $b \approx b^\alpha$):

$$E_N = a \cdot ch_N + b \tag{5.10}$$

$$E_C = a \cdot ch_C + b \tag{5.11}$$

This will be called the *final* calibration and its resulting energies must coincide with the most realistic simulations ($\alpha \to$ simulation).

Then, the ratio between the peak centroids is approximately constant in some situations:

- If $ch_N = ch_C$. It is trivial that $E_C = E_N$ and $E_C^\alpha = E_N^\alpha$. In general any calibration will give the same energy for the two peaks fairly or not. What is more, there will be a unique ΔE thickness making the peaks to coincide in the simulation.

- If $ch_N \neq ch_C$, it is possible to develop

$$\frac{E_N}{E_C} = \frac{E_N^\alpha}{E_C^\alpha} \Leftrightarrow \frac{a \cdot ch_N + b}{a \cdot ch_C + b} = \frac{a^\alpha \cdot ch_N + b^\alpha}{a^\alpha \cdot ch_C + b^\alpha} \Leftrightarrow \frac{a}{b} = \frac{a^\alpha}{b^\alpha} \tag{5.12}$$

  So the ratio is strictly constant whenever the ratio of the calibration parameters is. But also when the offsets b, b^α are much smaller than the peak energies, i.e. $b \ll E_C, E_N$ and

$b^\alpha \ll E_C^\alpha, E_N^\alpha$, so it is possible to neglect them. Then the calibrated energies are

$$E_N \approx a \cdot ch_N,\ E_C \approx a \cdot ch_C \tag{5.13}$$

$$E_N^\alpha \approx a^\alpha \cdot ch_N,\ E_C^\alpha \approx a^\alpha \cdot ch_C \tag{5.14}$$

And the ratio reads

$$\frac{E_N}{E_C} = \frac{E_N^\alpha}{E_C^\alpha} \Leftrightarrow \frac{a \cdot ch_N}{a \cdot ch_C} = \frac{a^\alpha \cdot ch_N}{a^\alpha \cdot ch_C} \tag{5.15}$$

Which is always valid.

Since the offset parameters of the alpha calibrations are around the 200 keV and the elastic peaks reach about 20 MeV in each detector (similar values are expected for the final calibration), only a 1% of error is introduced with the approximation. This inaccuracy is one order of magnitude less than the resolution of the peaks (1-2 MeV FWHMs) so it is not a limiting factor. The thickness from the simulation showing the best agreement between E_N/E_C and E_N^α/E_C^α is chosen. Notice that the deduced thickness from the spectrum of a given E-detector pixel is actually associated to the set of pixel regions in the ΔE-detector that is punched-through. The nominal angles/solid angles are used in the procedure since two beams are used, each with a different reaction point position. These are the main sources of error and, regarding the fluctuations observed in the energy ratios, up to a ± 1 μm uncertainty is achievable. Simulations are performed with ΔE thicknesses from 30 μm to 50 μm, micron by micron. The reliability of choosing the proper thickness from a given pixel is illustrated in Fig. 5.18.

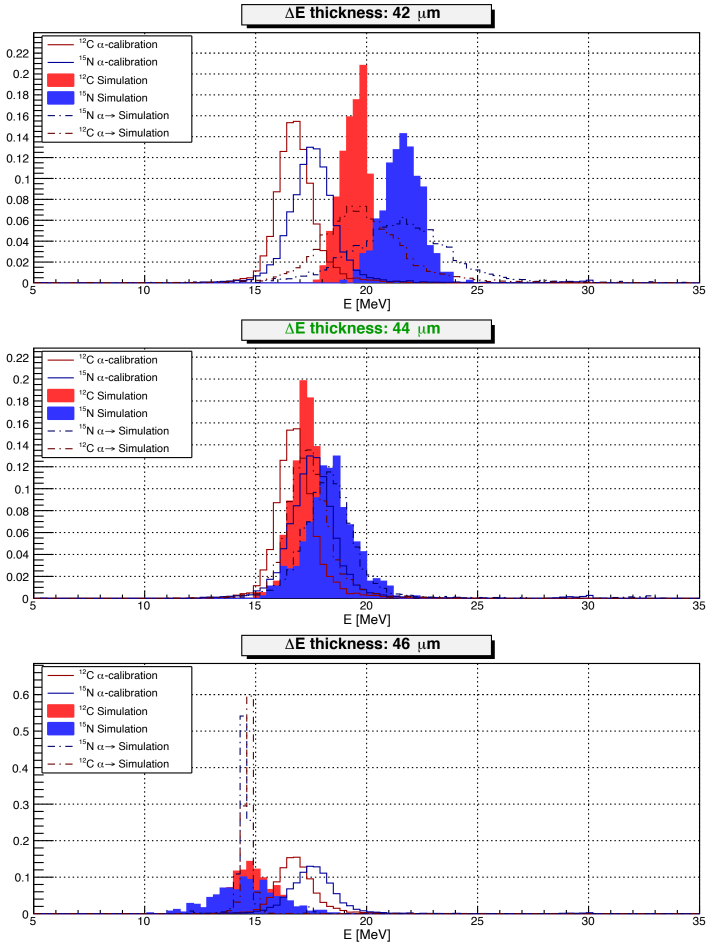

Figure 5.18: Variation of the elastic ^{12}C and ^{15}N peaks in the E-detector (det. AA pixel F2B4) for different ΔE-detector thicknesses. The experimental α-calibrated peaks (solid lines) are compared to three different simulations (filled histograms): with a 42 μm thick ΔE-detector on the top, with a 44 μm thick ΔE-detector in the middle, and with a 46 μm thick ΔE-detector on the bottom. In each case the α calibration is corrected in order to make the experimental centroids coincide with the simulated ones, leading to the recalibrated spectra (dashed lines). The ratio between the peak centroids determines the most proper thickness that allows for a good recreation of data, which in this case is 44 μm.

If the simulated ΔE thicknesses is underestimated, the peaks are more separated than in reality, so when one tries to recalibrate the experimental data in order to make the observed centroids coincide with the simulated ones, the resulting spectrum shows a unexplainable worsening of the resolution (as shown in the top plot of Fig. 5.18). On the other hand, if the simulated ΔE thickness is overestimated, the peaks are closer than in reality, even they may completely overlap (as it occurs in the bottom plot of Fig. 5.18) or they swap the order of appearance in the spectrum. Then the recalibration of the experimental data leads to very narrow peaks or negative slopes, being also unable to recreate the simulation without huge distortions. In this particular case, the best thickness is found to be 44 μm. This is 2 μm above the nominal thickness, which is enough to introduce a huge change in the expected spectra (much closer peaks and a $\sim$5 MeV shift). The α calibration seems to change very little, as it is supposed to do at these energies. Even the FWHMs are kept almost constant after the recalibration, so we still can explain the observed resolution. However, even if the α calibration was worse or if the resolution to expect was not perfectly known, by comparing the ratios between the centroids, as explained previously, it is possible to choose a proper ΔE thickness from each E-detector pixel. The resulting ΔE thickness maps, deduced from the E-detectors spectra, are shown in Fig. 5.19. Due to the continuous and smooth resulting trends, dead strip observations are deduced from the arithmetic mean of the neighboring pixels. Thin target data is used for this calculation since its better resolution will allow for a more accurate estimation of thicknesses. The statistics allow for coherent maps in telescopes A, B and F, and even a general trend reaches to be appreciated in detector E, despite showing many outlier pixels.

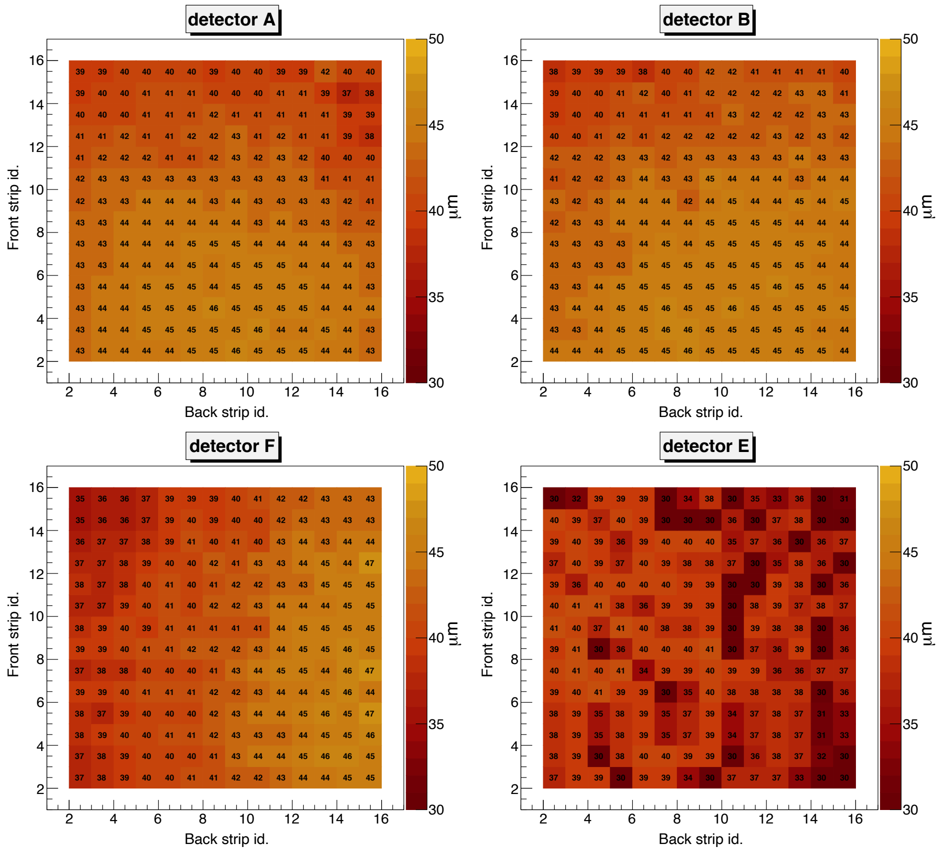

Figure 5.19: Deduced thickness for ΔE detectors A, B, F and E . Each pixel thickness with a ± 1 μm uncertainty associated.

It is found a 7 μm variation in detector A, from 39 to 46 μm, meaning almost a 20% fluctuation over the nominal thickness. With the current ± 1 μm acceptable error in each pixel, the thickness uncertainty has been reduced down to a 2%, being a really successful improvement. Similar results are found in detector B, adding consistency to the method. Furthermore, the trends are very similar to the ones observed in other works that have estimated thin DSSD thickness maps, such [55]. In detector F the inhomogeneity is a little larger, from 35 to 47 μm. In detector E, ignoring those pixels breaking the trend, a similar feature can be hinted, varying from 35 to 41 μm. These results may look suspicious at first glance, since the thickness decreases in the same direction as the scattering angle in all detector, but no acceptable change in the geometry (detector tilts, reaction point position and beam angle) can explain the relative position of the ^{12}C and ^{15}N peaks as these thickness inhomogeneities do: a 5° tilt in a detector position might change its effective thickness by a factor 1/cos(5°) ~0.4%, which is far from the 20% fluctuations observed.

Despite having considerably reduced the uncertainty in the thickness maps from $\sim \pm 10$ μm to ± 1 μm, this error is still too large to perform a fine calibration with stable beams punching-through the ΔE detectors. The introduced loss of resolution in the spectra is not worth and the discrimination of reaction channels in the 2D spectra gets worse. For this reason the α calibration is used in the reaction channel identification shown further in this work, always being aware of the effects of such large extrapolations of the calibrations.

5.10 Angular distribution

The final integrated statistics of ^{15}C, adding the two targets files (analyzed separately, though) is shown in the following tables 5.4 - 5.7. Due to the amount of pixels that need to be erased in telescopes A and B because of the channeling overlap and since they cover almost identical angles (only slight differences arise after the geometry optimization) the two detectors are also summed, reducing the associated uncertainty in this angular region as much as possible. On the other hand, telescopes F, E and D have been analyzed strip by strip, adding the statistics in groups of 3 strips later. In these detectors, the two outer strips on each side have been removed due to resolution or counting issues. Only back strip #11 in telescope F has been erased due to channeling, whose effect tends to become less important as the statistics decrease to these levels.

Table 5.4: Telescopes A+B - Sectors information and final number of counts for elastic ^{15}C on ^{208}Pb at 4.37 MeV/u. All accumulated statistics with the two targets.

Telescope	Sector θ_{LAB}	Sector Ω_{LAB}	^{15}C counts
A+B	25.3°	64.1 msr	7777
	31.6°	67.5 msr	3336
	38.0°	42.5 msr	1034
	47.2°	35.3 msr	400
	52.6°	95.8 msr	728

Table 5.5: Telescopes F - Sectors information and final number of counts for elastic ^{15}C on ^{208}Pb at 4.37 MeV/u. All accumulated statistics with the two targets.

Telescope	Sector θ_{LAB}	Sector Ω_{LAB}	^{15}C counts
F	62.3°	72.5 msr	229
	70.9°	77.6 msr	159
	78.2°	52.1 msr	86
	88.2°	72.5 msr	72

Table 5.6: Telescopes E - Sectors information and final number of counts for elastic ^{15}C on ^{208}Pb at 4.37 MeV/u. All accumulated statistics with the two targets.

Telescope	Sector θ_{LAB}	Sector Ω_{LAB}	^{15}C counts
E	91.8°	59.6 msr	40
	100.4°	63.8 msr	21
	109.2°	63.8 msr	9
	117.7°	59.6 msr	10

Table 5.7: Telescopes D - Sectors information and final number of counts for elastic ^{15}C on ^{208}Pb at 4.37 MeV/u. All accumulated statistics with the two targets.

Telescope	Sector θ_{LAB}	Sector Ω_{LAB}	^{15}C counts
D	128.2°	79.4 msr	4
	136.6°	85.0 msr	3
	145.2°	85.0 msr	3
	153.4°	79.4 msr	2

The poor amount of ^{15}C that is finally integrated is appreciated in the tables above. It will be seen how such few counts lead to very large error bars in the angular distribution and that they will be specially enhanced in the representation when normalizing to Rutherford, mainly due to the large grazing angle ($\sim 100°$) of the elastic cross section. It is estimated that, from the total requested beam time, after tuning issues and dead time corrections, a 40% is used. In addition, the averaged beam intensity observed in the data is a 5% of the expected value. Approximately, a 30% of statistics is lost due to dead/faulty strips and channeling troubles. All this means that only a 1.4% ($0.4 \cdot 0.05 \cdot 0.7$) of the planned statistics is finally achieved, making understandable the uncertainties and statistical fluctuations that are observed in the results.

6 E788S experiment

Despite the availability of a pure ^{17}Ne beam with a rather good intensity, E788S turns out to be the first experimental probe of this two-proton halo at energies around the Coulomb barrier ever. Analogously to IS619, a 1 mg/cm^2 ^{208}Pb target and the GLORIA detection system are used in order to measure the angular distribution of the elastic scattering at 8 MeV/u and explore other possible reaction channels, such as breakup, open due to the weakly bound structure of the nucleus.

6.1 Energy calibration, matching and tolerance

We face again a calibration issue associated to the large dynamic ranges required for the detectors and the low energies of the natural alpha emitters (up to 6 MeV). This time, and due to the properties of the facility, beam could not be changed easily (without changing the accelerator settings and hence all the tuning) except to ^{20}Ne at the same energy per nucleon, which unfortunately is out of range in any of the used detector, preventing from any attempt of stable beam calibration. Hence an alpha calibration is computed following the same method applied for IS619 experiment. A matching between sides is then performed for DSSDs (this time E-stages are all pad silicon detectors) and the tolerance window of every detector is set regarding the extrapolation of the alpha calibrations in the region of the elastic ^{17}Ne events. The dispersion of these events in a $E_{front} - E_{back}$ plot will determine the required tolerance between the energies of the sides in order to not miss good physical data. In Fig. 6.1 one can notice tha for detector A at least a ± 2 MeV tolerance window is needed to keep the elastically scattered ^{17}Ne at E_{front} ∼45 MeV.

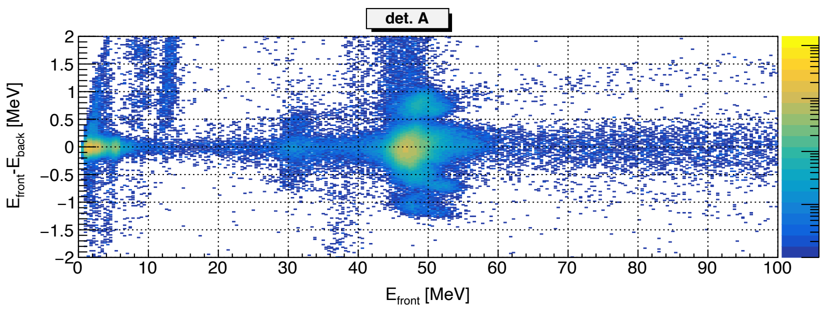

Figure 6.1: Front minus back energy versus front energy in detector A for all ^{17}Ne data after applying alpha calibration and energy matching. Energy tolerance between sides is kept below ±2 MeV in this case.

The cost of leaving a large tolerance, i.e. higher than the intrinsic resolution of the detector, would be the presence of some remaining charge-sharing events, as it will be discussed in the following section.

6.2 Charge sharing

Before the matching process, allowing adjacent strips to be hit or not, it is possible to separate a DSSD data into three sets: one with no charge-sharing events at all, one with all potential charge-sharing events in the back side, and another one with all potential charge-sharing events in the front side. Notice they are called potential charge-sharing events since we could expect a noise signal adjacent to a full-energy signal and that would be triggered as charge-sharing. After applying the alpha calibration and matching sides in energy, the different sets of events for detector A, in a front versus back energy representation, is shown in Fig. 6.2.

The separation of charge-sharing events in detector A is perfect: we do not miss any full-energy elastic event with the applied condition of hit adjacent strips. The first set of data comprises 96.89% of the total events, the potential back-side charge-sharing events are 1.75% and the potential front-side charge-sharing events 1.05%. The remaining 0.3% are potential charge-sharing in both sides.

In the back-side charge-sharing data set (middle plot in Fig. 6.2), a clear branch departs from the full-energy elastic spot of ^{17}Ne and goes upwards. These events have almost constant energy in the front-side (quite vertical branch) and show a deficit in the back side, where the sharing has occurred. Hence, the matching process has paired the full-energy in the front side with the largest value among the shared ones in the back side.

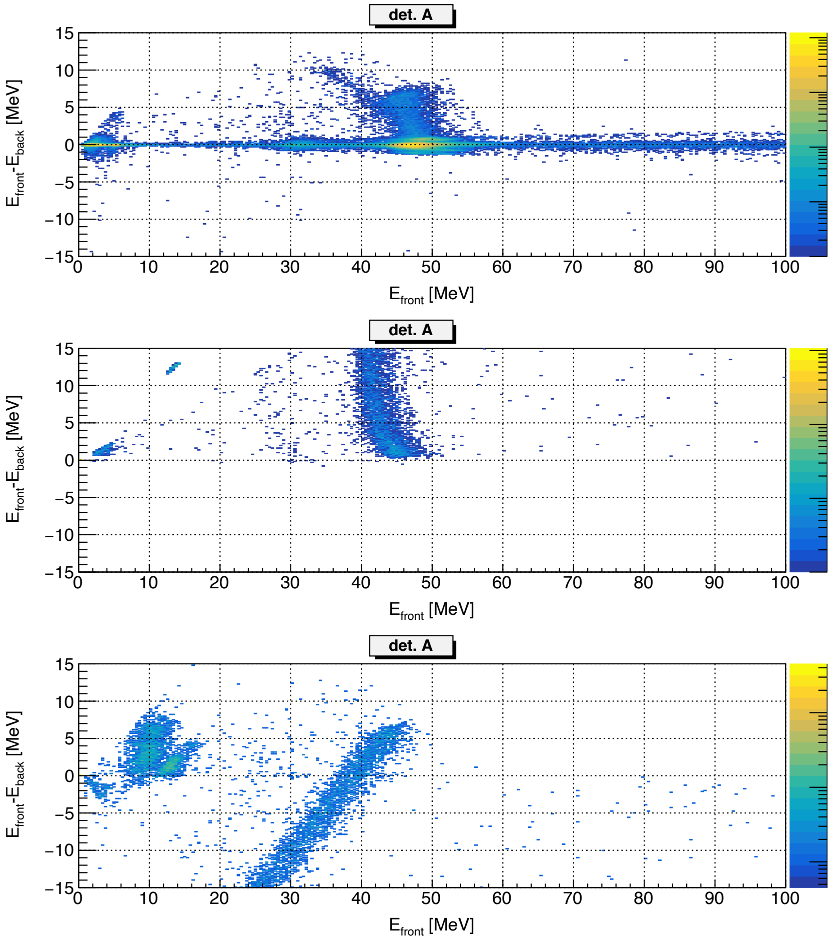

Figure 6.2: Front minus back energy versus front energy in detector A for ^{17}Ne data after applying alpha calibration and matching. Set with no charge-sharing events in the top, set with all potential back-side charge-sharing events in the middle and set with all potential front-side charge-sharing events in the bottom.

In the front-side charge-sharing data set (bottom plot in Fig. 6.2), a similar branch is found. This time it shows a constant energy in the back side and a deficit in the front side, where the sharing occurs. Nevertheless, it is noticeable how this branch does not start in the full-energy elastic spot, but from a point with already an energy deficit on the back side of about 5 MeV. Actually, it directly connects with the little branch found in the set with no charge-sharing events. The fact that the front-side charge-sharing events begin with a deficit of energy on the back side, makes this branch to cross the $E_{front} = E_{back}$ horizontal line at some point. Thus, if the front-side charge-sharing events could not be separated with this method, few events from such branch would survive the tolerance condition during the matching process and a secondary elastic peak shifted to lower energies would show up. This shift seems to be proportional to the deposited energy (remember it is not observed for alphas) and the amount of counts would depend on the accepted tolerance window. Supposing the sharing occurs uniformly in any ratio and having a tolerance of 2 MeV in 100 MeV of dynamic range, that would mean a 2% of this branch would survive. If front-side charge-sharing events are less than 1% of total data, then the secondary peak must be lower than 0.02% of the main peak. Despite of the low intensity of this effect, it is very often observed in logarithmic scale and, the fact of finding such counts creating a very discrete peak, is somewhat misleading specially if one is looking for reaction channels.

On the other hand, the first set, completely free of charge sharing, besides all events in the $E_{front} = E_{back}$ line, also shows some events out of it creating a short branch with a lack in back energy which extends exactly until the charge-sharing in the front-side actually starts. Since these two branches connect so precisely, one seems to be the continuation of the other. Apparently, not only a fraction of charge is always missed on the back side in front-side charge-sharing events, but also in some events before a sharing between front strips is noticed. And when one begins, the other disappears.

6.3 Geometry optimization

The nominal geometry, i.e. assuming the beam direction coincides with the z-axis and the reaction point lies at the origin of coordinates, gives a poor agreement between the two forward telescopes A and B, which needs to be corrected. A least squares minimization is performed by computing for each pixel observation:

$$I \cdot \sigma_{Pb} \cdot t = \frac{N^{obs}}{d\sigma_{Ruth}/d\Omega \cdot \Delta\Omega} \tag{6.1}$$

Where I is the beam intensity, σ_{Pb} the superficial density of scattering centers, t the measurement time, N^{obs} the observed number of ^{17}Ne counts, $d\sigma_{Ruth}/d\Omega$ the Rutherford differential cross section for its elastic scattering and $\Delta\Omega$ the solid angle of the pixel (which is corrected by a factor $\times 2\pi \sin(\theta)$ in order to compensate that dΩ are concentric rings in the Rutherford formula). The left side of Eq. 6.1 is a constant, so the averaged value of the right side for all pixels should also be. Actually, the angular distribution of points would only be flat if the data followed the $d\sigma/d\Omega$ function that has been used. The hit patterns and their respective angular distribution (with nominal geometry) used for the optimization are shown in Fig. 6.3.

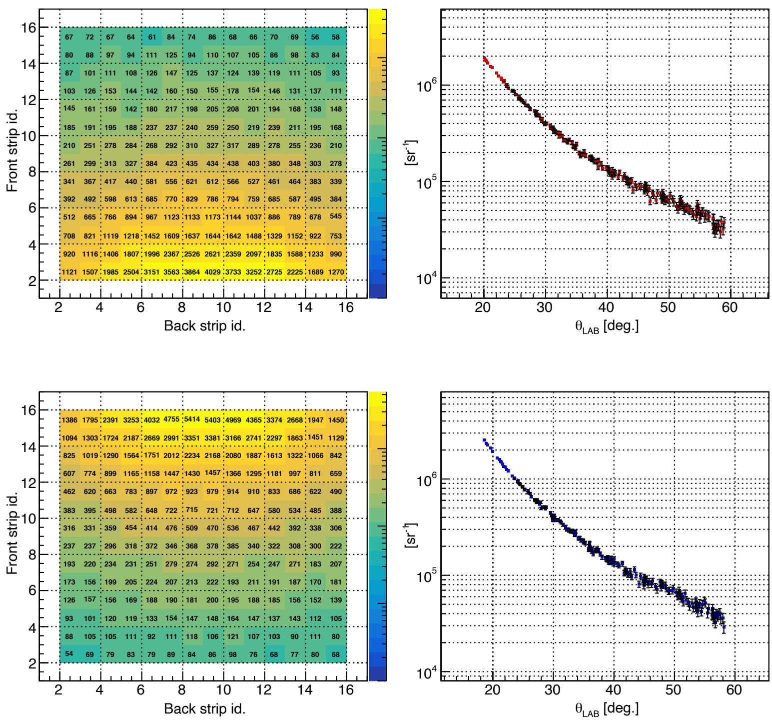

Figure 6.3: Hit patterns and angular distributions (with nominal geometry) of the number of counts observed in every pixel of telescopes A (top) and B (bottom). The number of counts is obtained from the mass spectra of each pixel by imposing multiplicity 1 in ΔE and E detectors and integrating the region 40-150 MeV on the x-axis and 10-70 MeV on the y-axis.

Little deviations are expected at large angles due to the fact that ^{17}Ne does not follow a perfect Rutherford distribution (the determination of this distribution is the goal of this experiment) and several reaction channels are opened. However, at low angles, the trends should coincide and, due to the large rate change of the $\sin^{-4}(\theta_{CM}/2)$ function in such region, these first points will dominate the optimization. The sum of the squared differences S clearly shows a minimum when varying the reaction point (the beam-target intersection, from where angles and solid angles are calculated) along the $x - y$ plane (see Fig.6.4). The z-coordinate is then unequivocally determined according to the optimized x and y values and assuming a perfect position of the target with its 30° tilt.

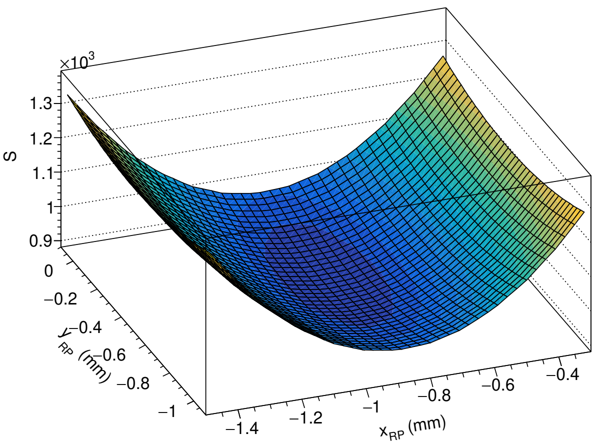

Figure 6.4: Surface of the sum of least squares (S) versus the position of the reaction point through the $x - y$ plane for the observations of telescopes A+B. Minimum found at $(x, y) = (-0.9, -0.5)$ mm.

This procedure shows an accuracy better than ± 0.1 mm in the determination of the reaction point position just by looking for the best agreement between telescopes A and B, which are assumed to be in their ideal positions (no relative freedom between them are considered) and the beam direction is always assumed to be in the z-axis. The achieved improvement is seen in Fig. 6.5, where the observation obtained for the nominal angles is compared to the one obtained with the optimized position. In view of the good resulting agreement, neither detector tilts nor a different beam direction is searched for.

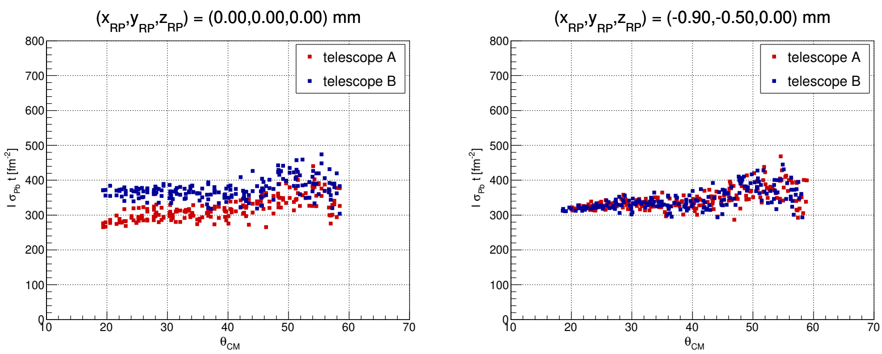

Figure 6.5: Agreement between the observation of telescopes A and B. To the left: nominal angles. To the right: optimized reaction point position in the $x - y$ plane.

The beam intensity has been deduced from one single file: run #243, which is 7.5 h long and showed a stable trigger rate during its acquisition according to the logbook. The dead time has been estimated to be a 10% and $\sigma_{Pb} \approx 3.78 \cdot 10^{-8}$ fm^{-2} (1 μm thick ^{208}Pb target with a 30° tilt). After the corresponding geometrical optimization, the averaged value of the ^{17}Ne beam intensity results $2.2 \cdot 10^4$ pps, which is in great concordance with the information provided by the GANIL operators, who reported fluctuations from $1{\cdot}10^4$ to $3{\cdot}10^4$ pps.

6.4 Mass spectra construction

Once charge-sharing events on both sides of the DSSDs are cleaned, alpha calibration is applied and data is matched with the suitable front-back energy tolerance, mass spectra are built. Due to the low statistics and the good resolution, pixels are grouped within angular sectors. The scattering angles and solid angles are obtained from the ΔE-detector DSSD pixels. Multiplicity one is imposed on the ΔE and on its corresponding silicon pad. Strips 1 and 16 on both sides are removed in order to avoid divergence effects. The evolution of the mass spectrum is illustrated in Fig. 6.6.

In the first angular sector, shown in Fig. 6.6, the elastic ^{17}Ne spot is found at $\Delta E + E = 130$ MeV. Few counts of ^{15}O coming from a possible dissociation of the halo are already observed with a continuous energy distribution from $\sim 110 - 130$ MeV. As the scattering angle grows, the amount of ^{15}O quickly increases, slightly varying the range of energies at which it is found. More reaction channels are open, specially at $\theta_{LAB} > 40°$, where fragment of mass $A = 13 - 16$ can be distinguished. In the last angular interval of telescope F that is shown in Fig. 6.7 it can be seen how some pixels already have no counts. Notice that back strip number 14 is dead in the DSSD of telescope F. The solid angle of dead or removed strips (1 and 16 on both sides) is not taken into account. However, the solid angle of alive pixels measuring zero counts due to statistics is crucial in the calculation of cross sections.

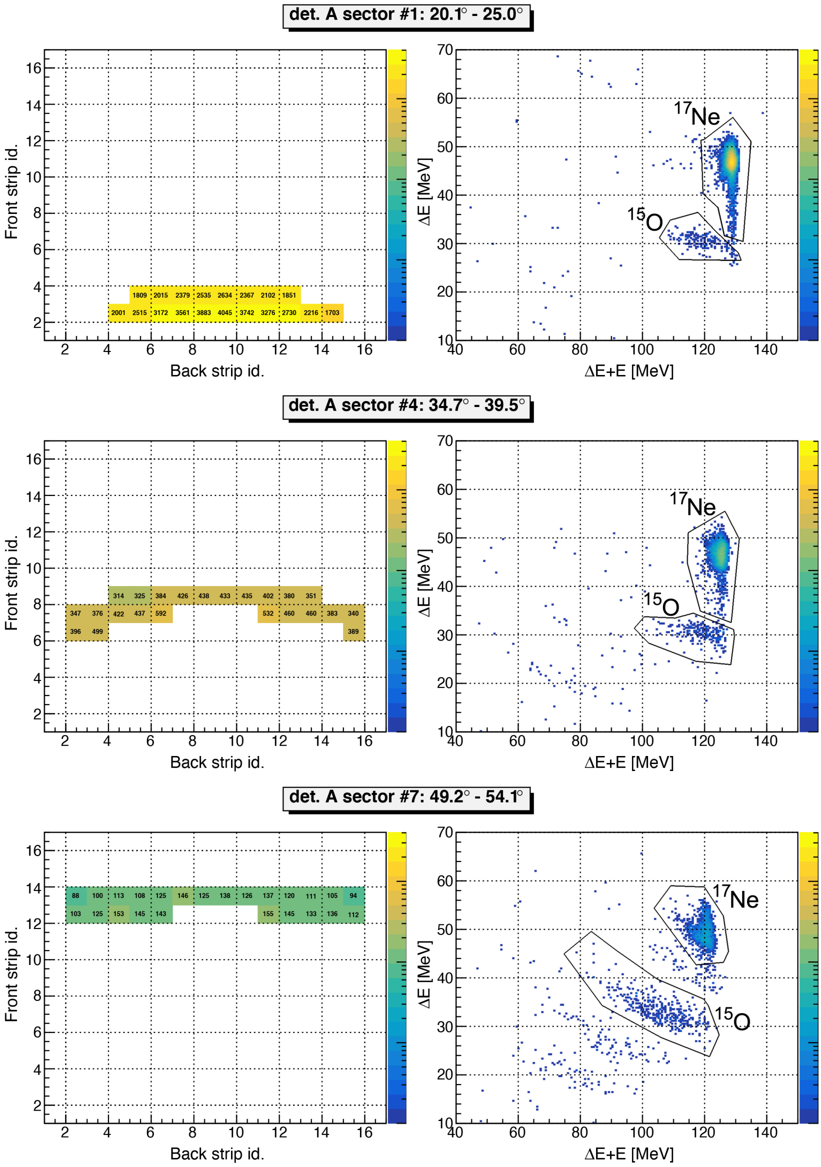

Figure 6.6: Hit patterns and mass spectra for 3 of the 8 angular sectors in which telescope A is divided. All statistics with the ^{17}Ne on 1 mg/cm^2 ^{208}Pb target at 8 MeV/u. Charge-sharing events have been removed, alpha calibration applied and matching tolerance set to 2 MeV on ΔE detector. Multiplicity 1 in both DSSD and pad of the telescope. Optimized angles are used.

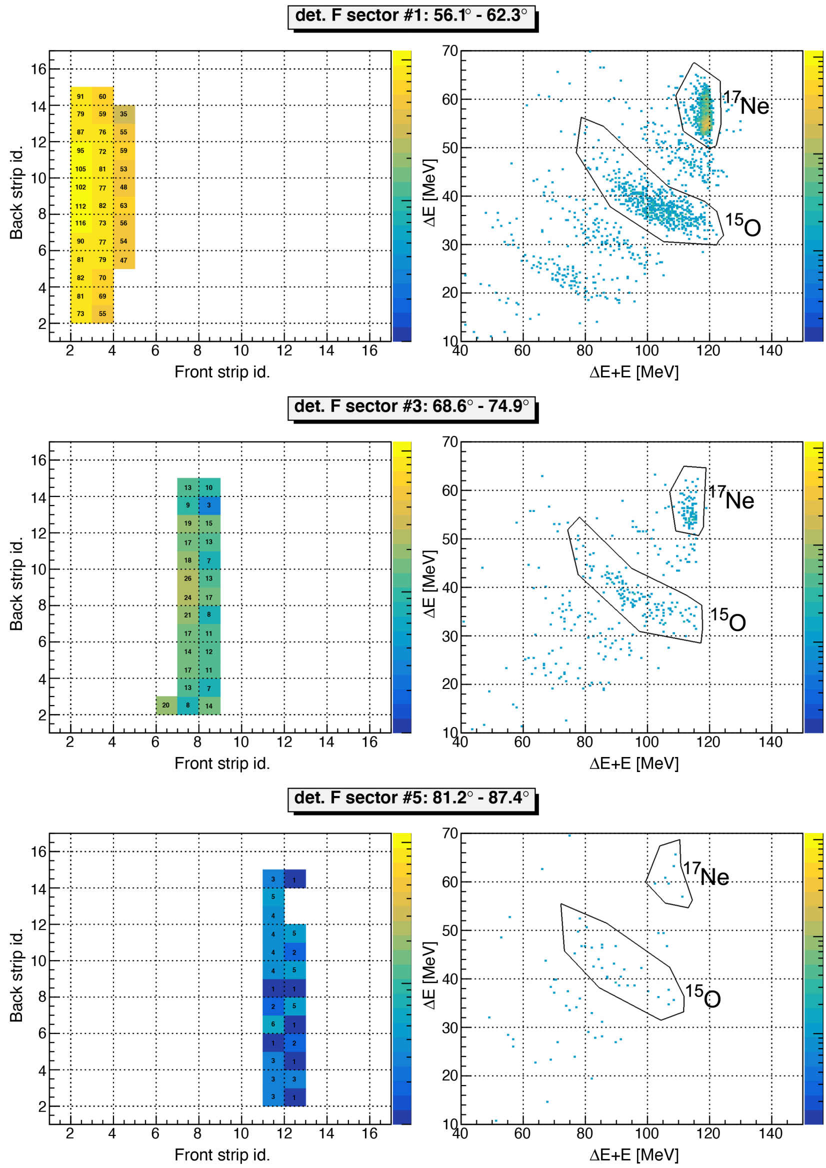

Figure 6.7: Hit patterns and mass spectra for 3 angular sectors in telescope F2. All statistics with the ^{17}Ne on 1 mg/cm^2 ^{208}Pb target at 8 MeV/u. Alpha calibration applied and matching tolerance set to 2 MeV on ΔE detector. Multiplicity 1 in both DSSD and pad of the telescope. Optimized angles are used.

The experimental spectra is compared to the Monte Carlo simulations performed with `geant4`. Little deviations are expected due to the large extrapolation of the energy calibrations so, experimental data is slightly corrected in order to make coincide the elastic channel and the position of ^{15}O, this way being able to identify the other reaction channels. Two angular sectors, one for telescope A and another for telescope F are shown in Fig. 6.8. Besides ^{17}Ne, also ^{15}O, ^{14}N and ^{13}C are simulated, all of them with a continuum energy distribution from the expected energy of the elastic ^{17}Ne to half this value. The trend of ^{15}O and ^{14}N is properly recreated, but the carbon shape disagrees more as it is further from the calibration region. Note the important presence of fluorine which might come from p-removal together with n-pickup. The energy losses occurring in the target and dead layers for ^{17}Ne have a mean value of 1.93 MeV according to the Monte Carlo simulations developed in Chap. 4.

It is observed, specially at the most forward angles in Fig. 6.6, that the channeling tail from the ^{17}Ne elastic spot reaches the most energetic region of the ^{15}O banana. This overlap might cause a mixture of channels during the integration. It is then worth to emphasize that the conflictive overlap region has been excluded from the integration of the elastic, what has a negligible effect over its cross section. In the ^{15}O channel, however, this might result in a slight overestimation, which should always be below a 1% and only in the most forward points, where the channeling is relevant.

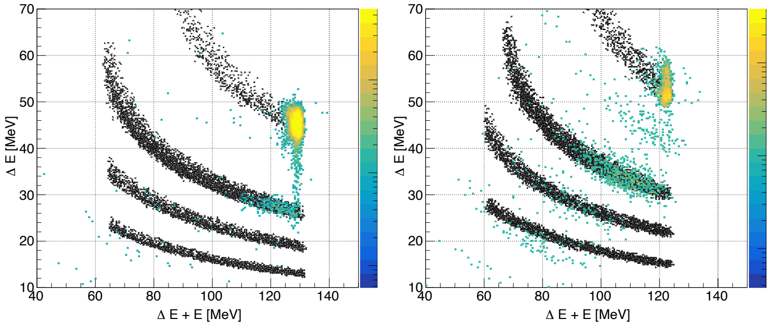

Figure 6.8: Experimental (color) versus simulated (black) mass spectra for one angular sector in telescope A centered at 32.3° (left) and another one in telescope F centered at 59.0° (right). Experimental data have been slightly scaled to get a proper recreation of the simulated ^{17}Ne and ^{15}O.

6.5 Angular distribution

The counts of ^{17}Ne and ^{15}O are integrated from the mass spectra for every angular sector in which telescopes A, B and F are divided. The scattering angle assigned to each sector is estimated as the average of all the pixel angles that comprise it. On the other hand, the solid angle of the sector is calculated as the sum of all pixel solid angles. These two values are then converted from LAB to CM frame according to the relationships described in chapter 2. For each sector, its corresponding number of counts is firstly corrected by the solid angle and then this value is plotted versus the scattering angle in order to get a proper angular distribution. These values are shown in Tabs. 6.1 6.2 6.3.

Table 6.1: ^{17}Ne and ^{15}O production from ^{17}Ne on ^{208}Pb at 8 MeV/u for 8 angular sectors in telescope A.

Telescope	Sector θ_{LAB}	Sector Ω_{LAB}	^{17}Ne counts	^{15}O counts
A	22.6°	39.8 msr	49793	170
	27.4°	55.6 msr	32447	251
	32.3°	58.2 msr	17537	231
	37.0°	52.4 msr	9094	227
	42.0°	59.8 msr	6369	274
	47.0°	53.6 msr	3720	305
	51.6°	52.2 msr	2351	370
	56.4°	54.3 msr	1527	398

Table 6.2: ^{17}Ne and ^{15}O production from ^{17}Ne on ^{208}Pb at 8 MeV/u for 8 angular sectors in telescope B.

Telescope	Sector θ_{LAB}	Sector Ω_{LAB}	^{17}Ne counts	^{15}O counts
B	20.9°	36.2 msr	60784	241
	25.9°	60.6 msr	43996	286
	31.0°	59.6 msr	21411	268
	35.8°	54.0 msr	10870	231
	40.8°	62.1 msr	7406	266
	46.0°	60.7 msr	4604	399
	50.8°	48.8 msr	2488	363
	55.5°	57.1 msr	1759	461

Table 6.3: ^{17}Ne and ^{15}O production from ^{17}Ne scattering on ^{208}Pb at 8 MeV/u for 9 angular sectors in telescope F.

Telescope	Sector θ_{LAB}	Sector Ω_{LAB}	^{17}Ne counts	^{15}O counts
F	58.0°	52.4 msr	1253	446
	62.1°	30.7 msr	354	210
	66.3°	58.1 msr	328	256
	70.6°	33.0 msr	73	78
	75.1°	60.2 msr	41	92
	79.4°	33.1 msr	14	18
	83.5°	47.1 msr	5	27
	87.3°	42.0 msr	2	8
	92.2°	52.4 msr	0	3

7

Results & theoretical interpretation

7.1 Near-barrier scattering of ^{15}C on ^{208}Pb

The ^{15}C differential elastic cross section obtained from IS619 experiment (on a ^{208}Pb target at E_{LAB} = 4.37 MeV/u) is shown in Fig. 7.1. The selection of the mass spectra for the elastic channel has been performed separately for both targets (1.5 and 2.1 mg/cm^2) as the straggling is quite different in the two cases. Due to the poor achieved statistics, both data sets have been added later, aiming to reduce as much as possible the error bars. With the same purpose, telescopes A and B, which cover the same nominal angles, have been averaged. In these telescopes, all conflictive pixels with channeling factors greater than a 2% have been removed, ensuring that the remaining ones have a channeling background under the ^{15}C elastic channel lower than a tenth part of the amount of carbon. These clean pixels conform irregular angular sectors and this is why the separation between points in the plot is not regular. Selections over telescopes F, E and D have been done strip by strip, adding then statistics in groups of 3 strips. The normalization to Rutherford has been performed using ^{15}N in telescopes A and B and the theoretical Rutherford function from telescope F onwards, assuming a flat trend up to the end of telescope F. This choice is made based on the fact that ^{15}N stops in the ΔE detectors in telescopes F, E, C and D and it would imply the use of multiplicity 1 events, which show some unexplained deficit in energy in some regions.

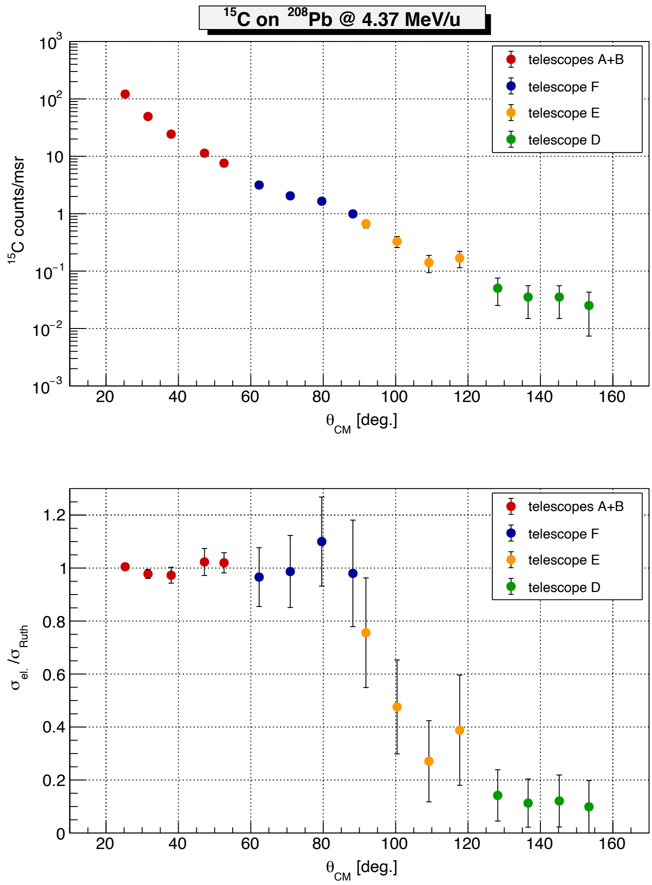

Figure 7.1: Angular distribution of the counts per steradian (top) and cross section normalized to Rutherford (bottom) for the elastic channel from the ^{15}C + ^{208}Pb at 4.37 MeV/u reaction.

The fact of having a grazing angle at such a large value ($\sim 100^{\circ}$) together with the lack of statistics lead to large error bars. Still, a hint of a Fresnel interference pattern in the elastic cross section is appreciated, despite the error bars include the case of a flat (Rutherford) behavior or even a slight absorption before 85°. It is clear, though, that an important absorption occurs from 90° onwards. Aware of the wide experimental resolution, it is not possible to identify reaction channels other than the elastic, although Monte Carlo simulations indicate that the breakup channel would not be clearly separable. If other channels were present and hence, integrated together, the cross section would be overestimated. With these conditions, being impossible to identify channels properly and with such reduced statistics, the estimation of any other cross section cannot be done.

7.2 Near-barrier scattering of ^{17}Ne on ^{208}Pb

The elastic ^{17}Ne and the ^{15}O channel from the ES788S experiment (on a ^{208}Pb target at E_{LAB}=8 MeV/u) have been integrated. The resulting number of counts are first normalized by solid angle and later by the corresponding Rutherford cross section ($\propto \sin^{-4}(\theta_{CM}/2)$). Due to the lack of any other beam to be compared with, the Rutherford proportionality factor is determined from averaging the first point of the telescope A with the first point of telescope B. The final angular distributions are shown in Figs. 7.2 and 7.3.

The differential cross section for the elastic ^{17}Ne is shown in Fig. 7.2. It starts from a pure Rutherford distribution, as it has been assumed in the normalization. Such classical trend is maintained for a short angular range until 35°, what makes the assumption consistent. A slight absorption is then observed between 35 and 55°, where the cross section remains constant somewhat below the Rutherford value. At 55° a fast suppression begins, until the cross section smoothly goes down until zero at about 90°. It is found that the cross section never exceeds the Rutherford limit; being the absence of rainbow the most remarkable feature of the dynamics of the system.

The ^{15}O fragments are observed through the whole angular range covered by the first three telescopes (from 20 to 95°). At the grazing angle $\sim$ 65°, where the rate change of the normalized elastic cross section is the largest and it takes a value of $\sigma_{Ruth}/2$, the amount of ^{15}O shows a maximum. There, the ^{15}O channel reaches a fourth part of the Rutherford cross section and from this point onwards it quickly decreases, as seen in Fig. 7.3.

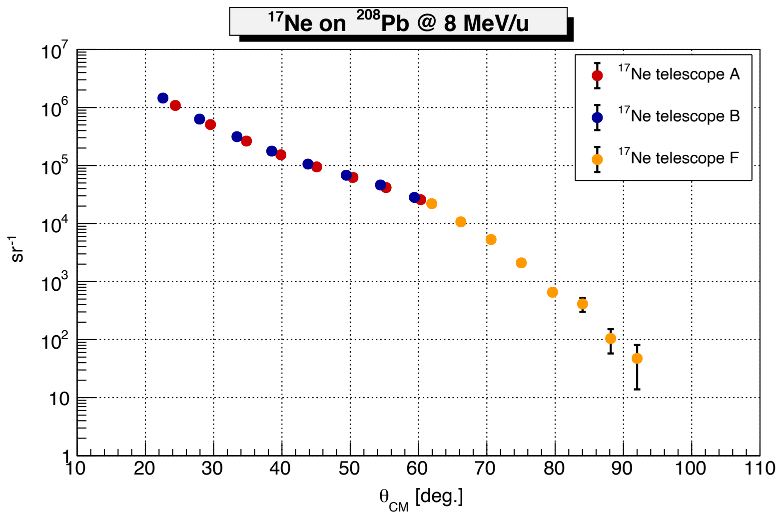

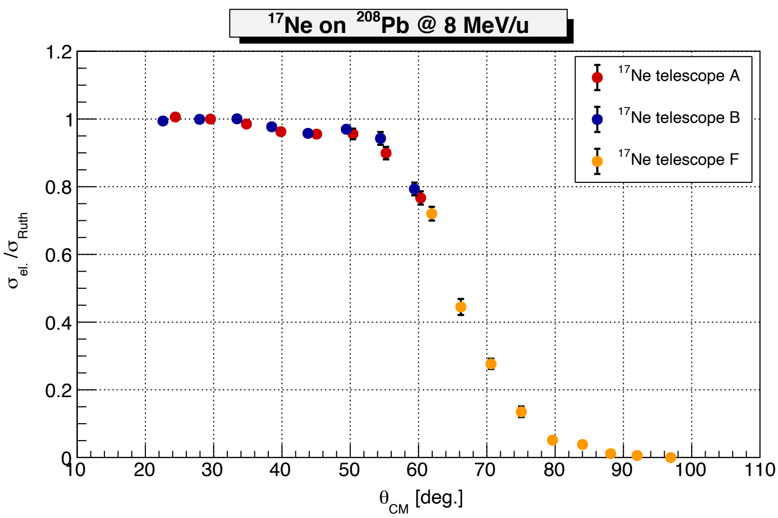

Figure 7.2: Angular distribution of the counts per steradian (top) and cross section normalized to Rutherford (bottom) for the elastic channel from the ^{17}Ne + ^{208}Pb at 8 MeV/u reaction.

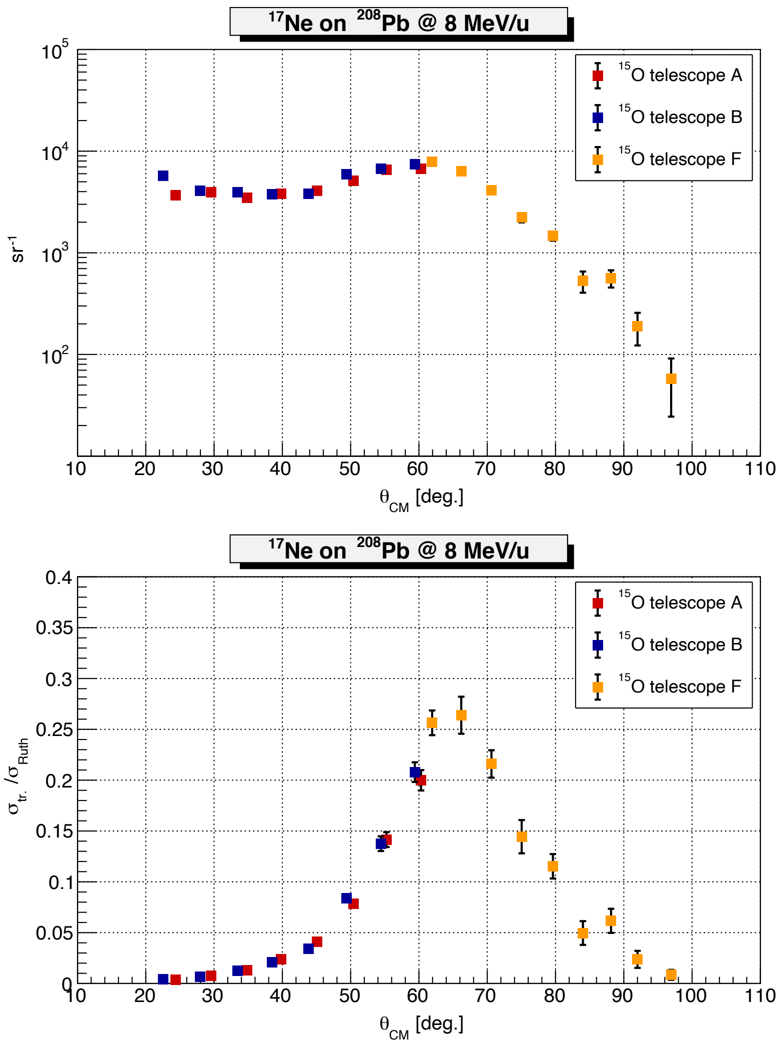

Figure 7.3: Angular distribution of the counts per steradian (top) and cross section normalized to Rutherford (bottom) for the ^{15}O channel from the ^{17}Ne + ^{208}Pb at 8 MeV/u reaction.

Regarding the error bars of Figs. 7.2 and 7.3, the uncertainty associated to a given number of counts N is estimated as $\sqrt{N}$, and, for the following normalizations, it is propagated. At low angles the statistics are large and having $6 \cdot 10^5$ accumulated particles in a given sector (point in the plot) means that the relative error is below the 0.5%, which is imperceptible in the figures. As the angle increases the relative error becomes larger due to the trend of the square root function and error bars start to be visible at $\sim 60°$. However, once the suppression of the elastic channel occurs, the number of counts quickly drops to zero, as well as the square root of it also does. In this region, the absolute error, which tends to zero, predominates over the relative one and errors get reduced again. It is remarkable to notice that in a representation of the counts per steradian the error bars will always increase with the angle as the statistics also do. However, in the a representation of the cross section normalized to Rutherford, the error bars might decrease with the angle due to the introduced $\sin^{-4}(\theta_{CM}/2)$ factor, which strongly drops with θ_{CM}, making then the absolute error more relevant in the visualization.

The kinematic curve, i.e. the energy profile evolution through the scattering angle of the elastic ^{17}Ne is shown in Fig. 7.4. Each bin in these plots indicates the number of particles measured for a given energy and angle range in telescopes A and F. The elastic channel shares some energy range for most angular sectors with other fragments from the reaction and would overlap in the plot, so it has to be properly integrated. The shape of the kinematic curves helps to understand the mechanism that originates each reaction channel, being ^{17}Ne a clear case of elastic scattering, showing a discrete energy profile through the angle (the observed narrow spread is only due to the experimental resolution). The analogous study is performed for the fragments of charge $Z = 9, 8, 7$ and 6 that can be separated in the mass spectra, which are shown in Fig. 7.5. All these channels show a wide continuum energy distribution peaked at $\approx 60°$. However, ^{15}O ($Z = 8$) also shows an extra component at low angles, with narrower energy distributions. In order to get meaningful results, these plots are projected for different angular ranges and normalized by solid angle, giving this way a proportional value to the differential cross section respect to energy.

For the ^{15}O case, the energy profile in different angular sectors is projected, see Fig. 7.6. The number of counts for each angle sector is corrected by the solid angle coverage (normalization of histograms), so this result is proportional to the differential cross section respect to the energy. Clear analogies are found respect to the breakup in the ^{11}Li+^{208}Pb near-barrier scattering [56].

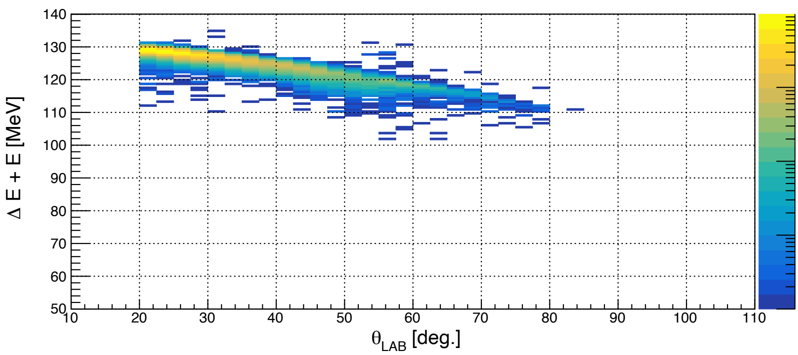

Figure 7.4: Kinematic curve for the elastic ^{17}Ne obtained from the integration of telescopes A and F mass spectra. The observed number of counts for given energy and angle intervals are shown in each bin.

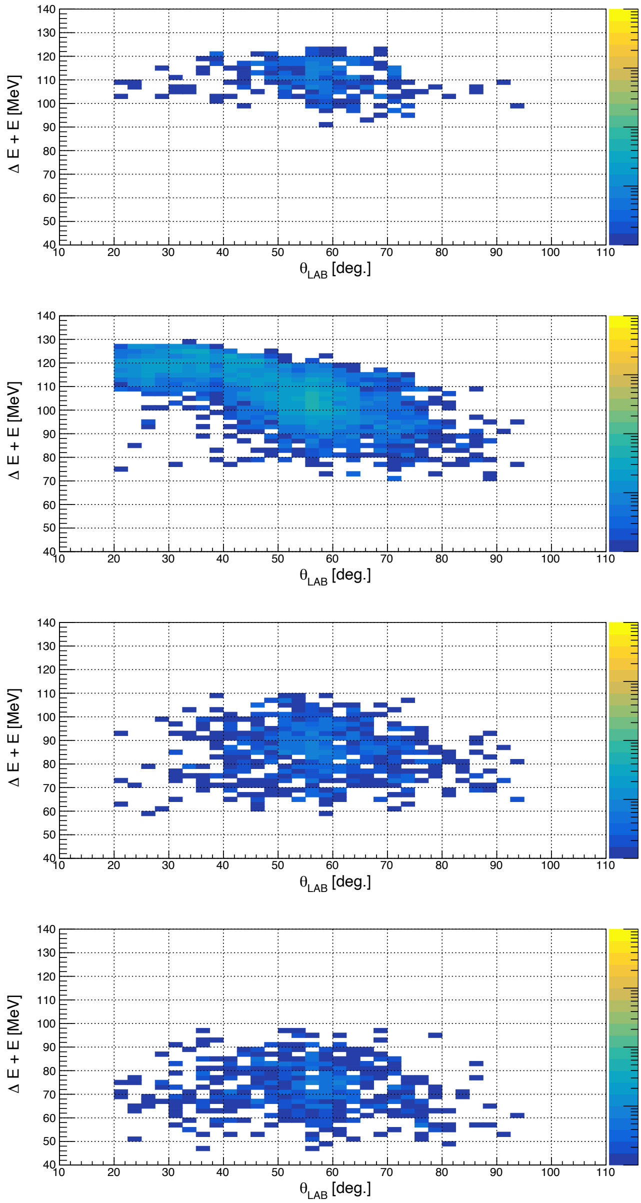

Figure 7.5: Kinematic curve for the fragments of charge $Z = 9, 8, 7$ and 6 (from top to bottom) obtained from the integration of telescopes A and F mass spectra. The observed number of counts for given energy and angle intervals are shown in each bin.

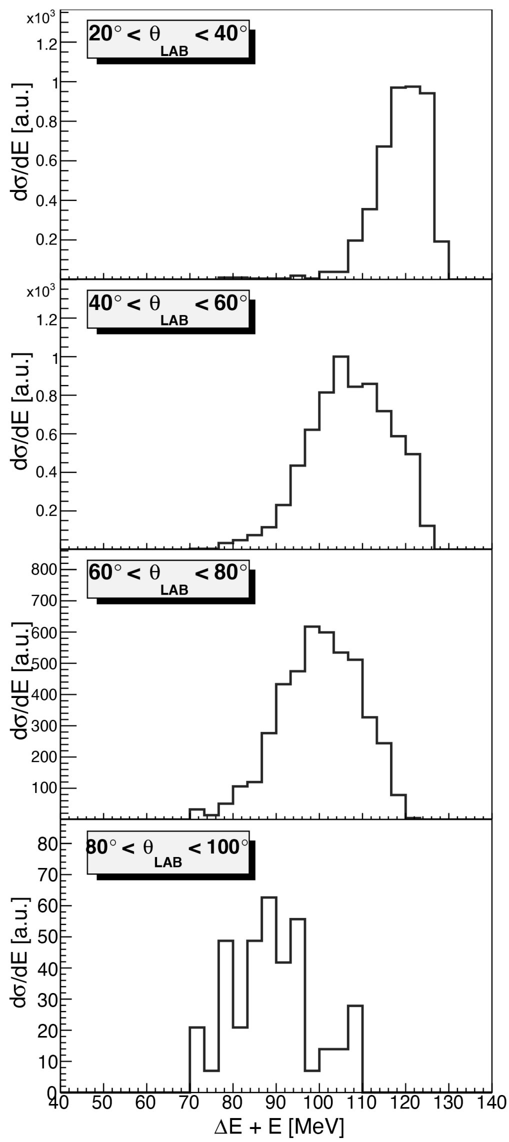

Figure 7.6: Energy distribution for the ^{15}O fragments in different angular sectors. Data from telescopes A and F, each histogram normalized by the covered solid angle.

7.3 Comparison between different halo nuclei

The reaction dynamics around the Coulomb barrier (V_C) of n-halo nuclei has extensively been studied previously (^{6}He, ^{11}Li, ^{11}Be) and most results can be summarized as dominating coupling effects to the continuum, as consequence of the weak binding energy of valence nucleons, leading to the suppression of the Coulomb-nuclear interference in the angular distribution of the elastic cross section. Large total reaction cross sections σ_R are observed, being a large fraction of it due to direct processes, e.g. breakup or transfer.

The proton halos remain, however, less studied, being ^{8}B ($S_p = 138$ keV) the only well investigated case. In spite of the centrifugal and Coulomb barriers due to the angular momentum and the positive charge of the valence nucleon in the p-state configuration of the ^{8}B ground state, which were thought to inhibit the occurrence of the halo, an extended matter distribution has been observed. Then, one might expect the same results than those found for n-halo nuclei. However, at low energies around the Coulomb barrier, for the system ^{8}B+^{12}C the continuum coupling effects are found to be negligible [57], and for ^{8}B+^{27}Al only a minor suppression of the Coulomb-nuclear interference is observed [58]. At higher energies (3-4 $\times V_C$), ^{8}B+^{208}Pb shows features similar to non-halo systems [59] [60] [61]. CDCC calculations for ^{8}B on ^{64}Zn and ^{208}Pb close to the barrier, show that the Coulomb and centrifugal barriers felt by the valence proton suppress the coupling effects and hence the results differ from the n-halo nuclei [62]. The ^{8}B+^{208}Pb near-barrier scattering [63] has, however, given a large σ_R value from an OM fit compared to weakly bound non halo nuclei.

Furthermore, there are remarkable results from the the most recently measured ^{8}B+^{64}Zn scattering around the Coulomb barrier [25], work which is closely related to this thesis. It was carried out in August 2018 in HIE-ISOLDE (during my international stay at CERN) with the GLORIA setup and happens to be the only ^{8}B study performed with a post-accelerated beam. It evidences that reaction dynamics barely show the effect of the continuum coupling, this time with $\sigma_R = 1.3$ b (from OM fit) 50% smaller than those obtained from n-halos, e.g. 2.7 b for ^{11}Be on same target and similar E_{CM}/V_C. The angular distribution of the elastic cross section is shown in Fig. 7.7, where a clear Coulomb-nuclear interference is seen. The total breakup cross-section, of the order of $\sigma_R/4$, indicates once more a different behavior from neutron-rich halos.

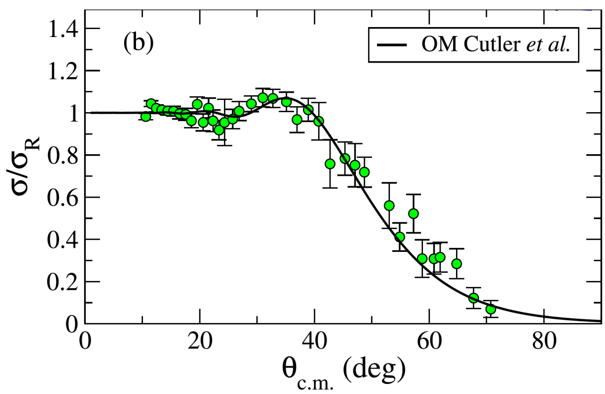

Figure 7.7: Angular distribution of the elastic cross section of the ^{8}B+^{64}Zn reaction at an energy 1.5 times the Coulomb barrier (E_{LAB}=38.5 MeV). Picture from [25].

It is specially interesting the comparison with the ^{17}Ne result of this work. Despite the use of a lighter ^{64}Zn target in the case of ^{8}B, what enhances the nuclear part of the interaction, the absence of rainbow is notorious in this case. Respect to the n-halo analogous cases, which show more gradual and never vanishing differential cross sections, the ^{17}Ne angular distribution quickly drops to zero, but also presents a plateau with a small reduction respect to Rutherford. The transfer of the two valence protons (2p-stripping) to the target could only be possible if it populates states at $E_{ex} \approx 27$ MeV in ^{210}Po according to the reaction Q-matching ($Q_{2p-strip} = 7.85$ MeV, $Q_{opt} \approx -19$ MeV). The ^{15}O cross section and the coupling effect on the elastic scattering must therefore come essentially from breakup.

On the same target ^{208}Pb and at similar energies (~ 135 MeV), the elastic angular distribution can be compared with the ^{20}Ne [64] and ^{22}Ne [65] cases (see Fig. 7.8), both stable nuclei measured decades ago. One can notice how a remarkable absorption is always present at pretty forward angles around 50° and how getting into the proton-rich zone implies a reduction of the Coulomb-nuclear interference, that completely vanishes in the most exotic case of ^{17}Ne. Such features can be interpreted in an Optical Model theoretical framework, as it was done for other halo nuclei, e.g. ^{11}Be+^{64}Zn [66]. A Woods-Saxon shaped volume potential (noted with a superscript 'V') plus a pure imaginary surface potential (a Woods-Saxon derivative, noted with a superscript 'S') is a common choice for reproducing the Coulomb polarization effect. Small amplitudes and large diffusenesses in this potential tend to create absorption patterns like those observed in the neon cases. Reference potential parameters are taken from [67], which uses a Woods-Saxon potential in Coupled Channels calculations. Identical radii and diffuseness are fixed for the three neon cases since, theoretically, they have almost the same radial dependence and collision energy [68]. As a constrain, the ratio between the amplitudes W^S for the ^{22}Ne and ^{20}Ne cases should be such that equals the ratio between the $B(E2)$ values to the first excited states $W^S_{^{22}Ne}/W^S_{^{20}Ne} \approx$ 0.023 e^{2}b^2/0.033 e^{2}b^2 [69], which are in principle the most favorable excitations. Once these parameters are obtained, the depth for the ^{17}Ne data is optimized with `sfresco`. This result does not fully explain the value of the transition $B(E2; 1/2^- \to 3/2^-) = 0.0066$ e^{2}b^2 [69] for ^{17}Ne, meaning that there might exist contributions from other states, such as the $5/2^-$, as it was observed in higher energy measurements of the reaction ^{17}Ne+^{208}Pb [70]. On the other hand, the volume potential depths lead to more or less pronounced interferences, being always free parameters during the fits. The obtained results are shown in Tab. 7.1 and Fig. 7.9. To the χ^2/N values from the resulting fits, somewhat off from unity, mainly contribute the limited recreation of the absorption patterns before the rainbows in ^{22,20}Ne at $\sim 50°$.

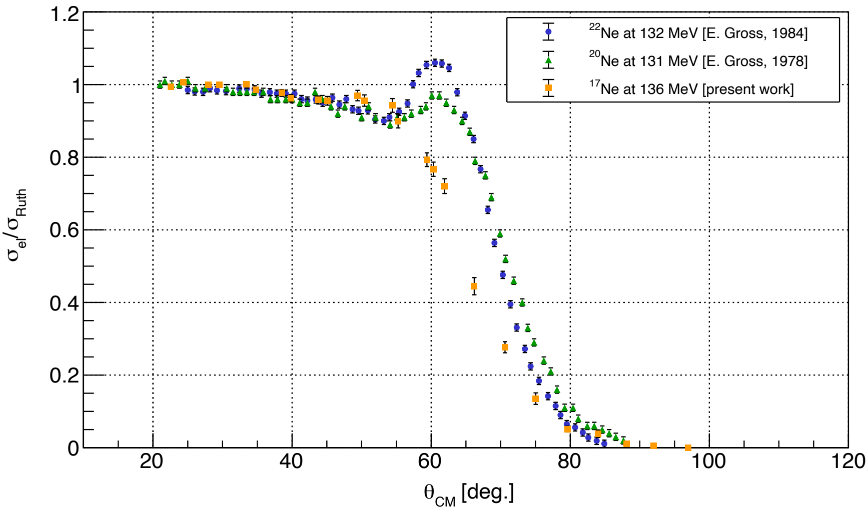

Figure 7.8: Comparison between the elastic cross sections for ^{22}Ne, ^{20}Ne and ^{17}Ne on ^{208}Pb at near-barrier energy.

Table 7.1: Optical potential parameters for the ^{22}Ne, ^{20}Ne and ^{17}Ne elastic scattering on ^{208}Pb at near-barrier energy. All depths in MeV, radii and diffusenesses in fm, integrated cross section in mb.

	V^V	r_V^V	a_V^V	W^V	r_W^V	a_W^V	W^S	r_W^S	a_W^S	R_C	σ_{reac}	χ^2/N
^{22}Ne	40.6	1.28	0.55	27.7	1.28	0.55	0.061	1.27	5.5	1.3	1952	2.5
^{20}Ne	29.8	1.28	0.55	33.5	1.28	0.55	0.087	1.27	5.5	1.3	2075	1.8
^{17}Ne	6.7	1.28	0.55	68.9	1.28	0.55	0.045	1.27	5.5	1.3	1953	2.4

On the other hand, the ^{15}C case shows interesting results as well. The apparent presence of a Coulomb-nuclear interference and the lack of dominant reaction channels other than elastic, which there might exists, though, makes one think of a non-halo behavior in the near-barrier dynamics. This would be understandable regarding the pretty large separation energy of its valence neutron S_n, above 1 MeV. Either way, breakup and 1n-stripping ($Q_{1n-strip} = 2.72$ MeV, $Q_{opt} \lesssim 0$) might be either absent due to scarce statistics or unresolved due to the energy resolution, calling for further investigations. The comparison with the equivalent elastic scattering of the well-bound carbon isotope ^{12}C on ^{208}Pb [71] is shown in Fig. 7.10. Such ^{12}C measurement is obtained at a 64.9 MeV bombarding energy and particles are detected using three silicon telescopes ($\Delta E - E$) in $\theta_{LAB} = 20 - 170°$ with an angular resolution of 0.5°. A similar trend is found, with a slightly shorter grazing angle but similar interference pattern, being the ^{15}C cross section always below the ^{12}C one.

The interpretation of the ^{12}C and ^{15}C elastic cross sections is pretty simple with only a Woods-Saxon volume nuclear potential in an optical model. Taking as reference the potential parameters from [71], the ^{12}C fit is recreated. Then, the potential depths are optimized with `sfresco`. Results are shown in Fig. 7.11 and Tab. 7.2. Note some unphysically large potential depths can be achieved with this method. A larger diffuseness with a less deep potential could lead to an equivalent fit (W/a_W ambiguity) and physical parameters.

The Coulomb barrier for the studied systems can be deduced from the potentials that have resulted from the Optical Model fits. The Coulomb barrier height is defined as the maximum value of the combined real potentials (see Eqs. 2.28 and 2.29) and the radius at which this occurs is then defined as the barrier radius. This is approximated by the evaluation of the potentials at a distance $R_C(A_p^{1/3} + A_t^{1/3})$, being R_C=1.3 fm in all cases and A_p, A_t the mass numbers of the projectile and target respectively. Results are shown in Tab. 7.3.

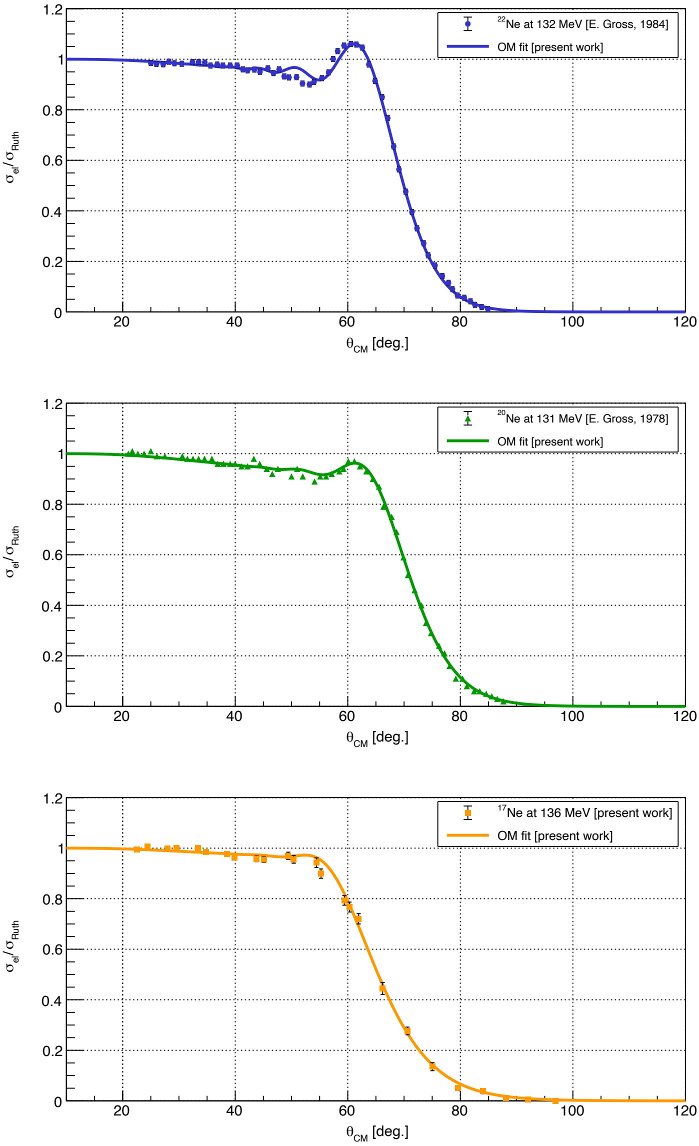

Figure 7.9: Optical model fits for the elastic scattering of ^{22}Ne, ^{20}Ne and ^{17}Ne on ^{208}Pb at near-barrier energy. Volume and surface potentials with Woods-Saxon shapes are used.

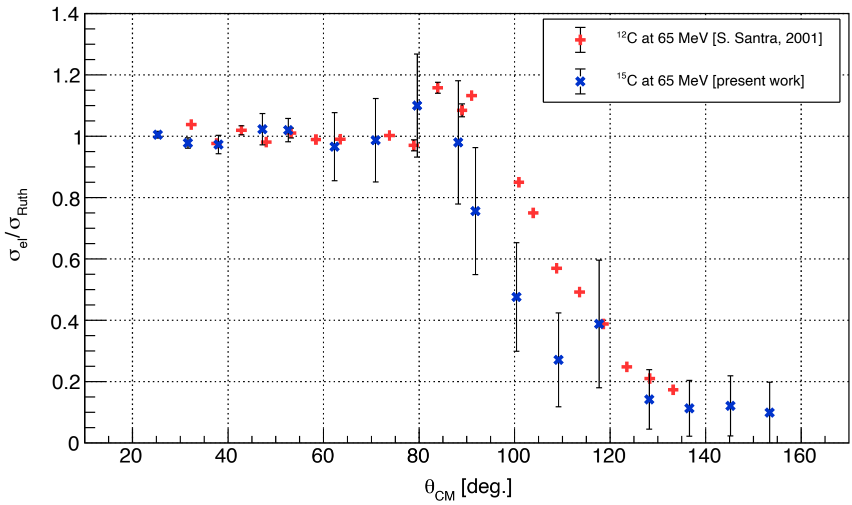

Figure 7.10: Comparison between the elastic cross sections for ^{12}C and ^{15}C on ^{208}Pb at near-barrier energy.

Table 7.2: Optical potential parameters for the ^{12}C and ^{15}C elastic scattering on ^{208}Pb at near-barrier energy. All depths in MeV, radii and diffusenesses in fm, integrated reaction cross section in mb.

	V^V	r_V^V	a_V^V	W^V	r_W^V	a_W^V	R_C	σ_{reac}	χ^2/N
^{12}C	66.6	1.28	0.46	120.3	1.27	0.37	1.3	426	7.4
^{15}C	18.2	1.28	0.46	829.7	1.27	0.37	1.3	682	0.3

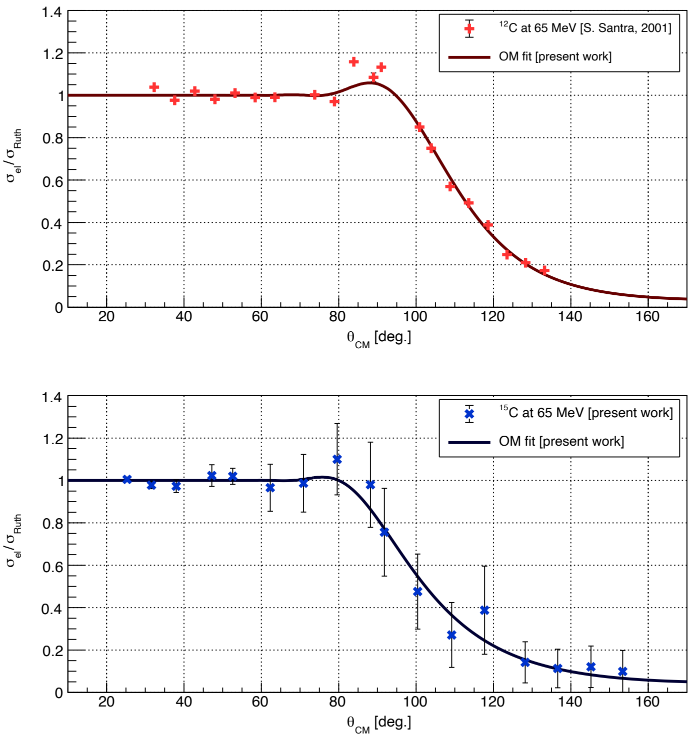

Figure 7.11: Optical model fits for the elastic scattering of ^{12}C and ^{15}C on ^{208}Pb at near-barrier energy. Volume potential with Woods-Saxon shape is used.

Table 7.3: Coulomb barrier deduced from the Optical potential fits for the ^{12,15}C and ^{17,20,22}Ne elastic scattering on ^{208}Pb data.

	^{12}C	^{15}C	^{17}Ne	^{20}Ne	^{22}Ne
V_C [MeV]	69.95	66.34	106.91	105.14	104.08

The total reaction cross sections σ_R obtained from the Optical Model fits can be normalized geometrically by πr_{sys}^2, being

$r_{sys} = R_C(A_p^{1/3} + A_t^{1/3})$. If these values are plotted versus the collision energy E_{CM} relative to the Coulomb barrier V_C (also deduced from OM), dependences on nuclear sizes and the reaction energies disappear. These points for the nuclei compared in this work are shown in Fig. 7.12. The ^{8}B value is taken from the OM calculations in [25] and all others are obtained from the fits previously described and calculated in this chapter. It is seen how, as the collision energy increases, the normalized reaction cross section also does. The relationship may look linear due to the scarce number of points, however, it has been shown that such trend for neutron halo and skin nuclei follows a Wong-type curve [72]. The measurement of reaction cross sections at different energies in future investigations might verify whether this behavior is also found in proton halo nuclei and whether they can be compared to the neutron-rich ones.

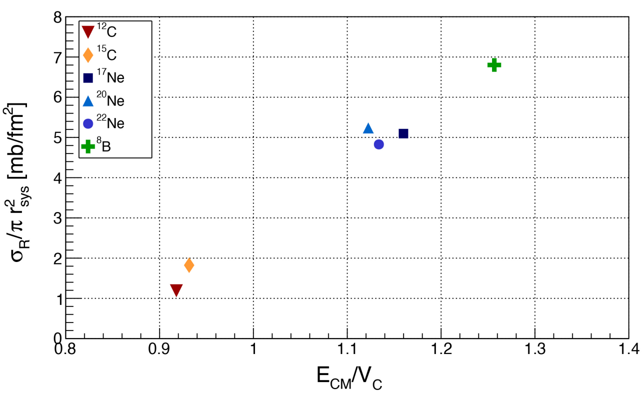

Figure 7.12: Reduced total reaction cross sections versus collision energies relative to the Coulomb barrier for the systems studied in this work within the Optical Model framework.

8
Conclusions

The near-barrier scattering on ^{208}Pb has been studied for ^{15}C (a disputed candidate of a 1n-halo) and ^{17}Ne (the only well established case of a 2p-halo), being the first studies of these two nuclei in this energy regime. The reactions have been measured in IS619 (ISOLDE, August 2017) and E788S (GANIL, February 2020) experiments respectively using the GLORIA detector and aiming to quantify the effects of the (suggested) halo structure of the two nuclei in their reaction dynamics. The conception, development and analysis of the two reaction experiments are presented in this thesis with the goal of getting a better understanding of the complexities of the atomic nucleus. The most remarkable points of this work are listed below.

- The six multi-segmented silicon telescopes that comprise the GLORIA detector allow for charged-particle spectroscopy around the reaction target with high granularity ($\sim 3°$) and solid angle coverage ($\sim 25\%$ of 4π) throughout a large angular range $\theta_{LAB} = 15 - 165°$ with no shadowing due to the target at any point. The configuration of the telescopes is such that it makes no shadowing of the reaction target at any angle. Asymmetries in the energy losses are introduced due to the geometry and position of the targets.

- The use of double-sided silicon strip detectors (DSSDs) has the advantage of providing information from many effective surface elements (16×16 pixels) with a reduced number of electronic channels (16+16), at the cost of a more sophisticated data analysis.

- Charge-sharing effect has been studied in detail in order to avoid misleading interpretations of the mass spectra. The condition of not having hits in adjacent strips and an energy tolerance in the matching process are imposed in order to get the best cleanup of such events.

- The energy calibration done with natural alpha emitters (energies between 3 and 6 MeV) turns out not to be reliable when it is extrapolated to the energies where the scattered beams and reaction fragments are found (20-40 MeV). This has to be taken into account when setting the matching tolerance between detector sides and when looking at the kinematic distributions of the observed particles.

- The large uncertainty ($\sim 20\%$) provided by the manufacturer in the thickness of ΔE detectors has been reduced down to a $\pm 1\mu$m error thanks the development of Monte Carlo simulations and the availability of two different beams (^{12}C and ^{15}N) that punch-through the ΔE detectors of the telescopes in IS619 experiment.

- The setup geometry has been optimized by searching the optimum position of the reaction point that best recreates a Rutherford distribution of a given beam. The minimization of a χ^2 fit by varying the reaction point position determines the angles and solid angles of all the pixels in the setup.

- ^{12}C and ^{15}N stable beams, measured during IS619, both at 4.37 MeV/u are used for this optimization. However, no other reference beam could be used in E788S, where only ^{17}Ne at 8 MeV/u was measured, fact that limits the optimization at very forward angles.

- High purity ^{208}Pb (>98%) targets have been used for the two experiments. For IS619 two different thicknesses of 2.1 mg/cm^2 and 1.5 mg/cm^2 were used. For E788S only a 1 mg/cm^2 ^{208}Pb target was used.

- The presence of ^{15}N in the radioactive beam of IS619 at the same energy as ^{15}C (with an abundance ratio ^{15}C/^{15}N$\sim$0.02) makes channeling to create an important overlap between the elastic channels of the two nuclei. This effect, caused by the lattice structure of the silicon detectors, has been quantified and considered in the analysis.

- The wide experimental resolution found in IS619 spectra prevent us from a clear distinction of the possible ^{14}C reaction fragments from ^{15}C. Hence, and despite no channel is enhanced respect to the elastic, some ^{14}C could be present in the integration of the elastic cross section.

- The angular distribution of the ^{15}C elastic cross section achieved with the final statistics ($\sim$2% of the initially expected) hints the presence of a Coulomb rainbow, although the large error bars cannot exclude its absence. Also, the possibility of having unresolved breakup and/or stripping counts integrated would make this a quasi-elastic result where the interference is actually the contribution of the other reaction channels.

- CC and CDCC theoretical models propose breakup and 1n-stripping as the most probable mechanisms for ^{15}C at near-barrier energies. 1n-stripping would contribute more at backward angles and breakup would be peaked at around $\sim 100°$. None of them are observed but this could be due to either the resolution limitation or a lack of statistics.

- OM calculations have been performed in order to describe the measured (quasi-)elastic scattering ^{15}C+^{208}Pb. With a Woods-Saxon volume potential and taking as reference the near-barrier ^{12}C+^{208}Pb case reported in literature, the angular distribution is satisfactorily reproduced.

- The case of ^{17}Ne scattering leads to very straightforward experimental results, where the elastic cross section is clearly characterized by the total suppression of the nuclear rainbow. Reaction fragments of charge Z=6-9 are found, being Z=8 (^{15}O) the dominating one and showing two components in its kinematic curve, probably due to two different reaction mechanisms of production (breakup and 2p-transfer leaving excited states in the resulting ^{210}Po). The abundance of all these fragments is peaked exactly at the grazing angle of the elastic channel $\theta_{CM} \approx 65°$.

- The absorption patterns found in the near-barrier elastic scattering of different neon isotopes on ^{208}Pb has been reproduced with an imaginary surface potential in the Optical Model framework, simulating the effect of a Coulomb polarization potential (CPP). This surface potential needs small amplitudes and large diffusenesses. The interference pattern, which is remarkable for the stable cases of ^{22}Ne and ^{20}Ne, but completely vanishes for the exotic ^{17}Ne, are recreated by varying the depths of the volume potential.

- At the moment, the publication of these results awaits more accurate CDCC calculations.

The study of nuclear reactions induced by halo systems at energies around the Coulomb barrier has proven to be a powerful tool to understand the dynamical behavior of atomic nuclei for a long time. It seems clear after this work that such research is still leading to new interesting phenomena and discoveries. Not only the progress in the understanding of our universe but also the technological advancements that this brings with it make the future of nuclear science look encouraging.

9
Conclusiones

Se ha estudiado la dispersión en torno a la barrera de Coulomb en un blanco de ^{208}Pb de los núcleos ^{15}C (un controvertido candidato de halo de un neutron) y ^{17}Ne (el único caso bien establecido de halo de dos protones), siendo estos los primeros estudios que realizan de estos núcleos en este régimen energético. Las reacciones se han medido en los experimentos IS619 (ISOLDE, agosto de 2017) y E788S (GANIL, febrero de 2020) respectivamente, usando el detector GLORIA, con el objetivo de cuantificar los efectos de su (sugerida) estructura de halo en su dinámica. El planteamiento, desarrollo y análisis de los dos experimentos se presenta en esta tesis doctoral, tratando de alcanzar una mejor comprensión de las complejidades del núcleo atómico. Los puntos más reseñables se listan a continuación.

- Los seis telescopios de silicio multi-segmentados que componen el detector GLORIA permiten hacer espectroscopia de partículas cargadas en torno al blanco de reacción con una alta granularidad ($\sim 3°$) y cobertura de ángulo sólido ($\sim 25\%$ of 4π) en un amplio rango angular $\theta_{LAB} = 15 - 165°$ y sin ningún tipo de sombra debido al blanco. No obstante, asimetrías en las pérdidas energéticas aparecen debido a esta geometría y posición de los detectores respecto al blanco.
- El uso de detectores de tiras de silicio de doble cara (DSSDs) tiene la ventaja de proporcionar información de un alto número

de elementos de superficie (16×16 pixels) con un número mucho menos de canales electrónicos (16+16), al precio de un análisis de datos más sofisticado.

- El efecto de compartición de carga entre tiras vecinas en los detectores se ha estudiado en detalle con el fin de evitar interpretaciones erróneas de los espectros de masa de los telescopios. La selección de sucesos con señal en tiras vecinas y la imposición de una tolerancia máxima durante el emparejamiento de señales entre ambas caras de un detector se impone para realizar esta limpieza.

- La calibración en energía realizada con fuentes alpha naturales (energías entre 3 y 6 MeV) resulta no ser fiable cuando se extrapola a los rangos energéticos en los que encontramos las partículas dispersadas (20-40 MeV). Esto se debe tener en cuenta al establecer la tolerancia de emparejamiento y al estudiar la evolución cinemática de las partículas medidas.

- La gran incertidumbre ($\sim$ 20%) proporcionada por el fabricante en los detectores se ha conseguido reducir hasta $\pm 1\mu$m gracias al desarrollo de simulaciones de Monte Carlo y a la disponibilidad de dos haces (^{12}C y ^{15}N) que atraviesan los detectores ΔE de los telescopios en el experimento IS619.

- La geometría del montaje experimental se ha optimizado buscando el punto de reacción que mejor reproduce una distribución de Rutherford en las medidas para un haz determinado. La minimización del χ^2 variando la posición del punto de reacción determina los ángulos y ángulos sólidos de todos los pixels de los detectores.

- Los haces estables de ^{12}C y ^{15}N, ambos a una energía de 4.37 MeV/u, son los empleados para dicha optimización en el experimento IS619. Sin embargo, el único haz disponible durante el experimento E778S fue el radioactivo de ^{17}Ne a 8 MeV/u, lo que limita la optimización a ángulos muy delanteros.

- Blancos de ^{208}Pb de alta pureza (>98%) se han usado para los dos experimentos. Para el IS619 dos blancos de distintos grosores (1.5 y 2.1 mg/cm^2) fueron utilizados. Para el E788S, sin embargo, solo se empleó un blanco de grosor 1 mg/cm^2.

- La presencia de ^{15}N como contaminante en el haz de ^{15}C en el experimento IS619 (en una presencia de $^{15}C/^{15}$N$\sim$0.02) crea un superposición en los canales elásticos de ambos núcleos debido al efecto de canalización en la red cristalina de los detectores de silicio. Este efecto ha sido cuantificado y considerado durante el análisis.

- La resolución experimental en el experimento IS619 impide una distinción clara entre el posible el elástico del ^{15}C y el posible ^{14}C procedente de su ruptura. Aunque ningún canal de reacción es relevante en comparación con el elástico, la presencia de ^{14}C de ruptura no puede ser descartada, aunque en una proporción muy pequeña. De ser así y habiendo integrado ^{14}C como ^{15}C elástico, la sección eficaz diferencial elástica resultante estaría sobrestimada.

- La distribución angular de la sección eficaz elástica del ^{15}C lograda con la estadística final ($\sim$2% de la esperada inicialmente) parece indicar la presencia de un patrón de interferencia, aunque las barras de error tan grandes no consiguen descartar su ausencia completamente. La posibilidad de tener cuentas procedentes de los canales de ruptura y/o transferencia en esta integración hace de este un resultado cuasi-elástico, donde la interferencia en realidad podría ser debida a la contribución de los otros canales de reacción.

- Modelos teóricos de canales acoplados proponen la ruptura y la transferencia de un neutrón como los mecanismos de reacción más probables para ^{15}C en torno a la barrera. La transferencia cobraría importancia en ángulos traseros y la ruptura mostraría su máximo en torno a $\sim 100°$. Ninguno de estos canales se observan pero esto podría ser debido bien a una falta de resolución energética o bien a una escasa estadística acumulada.

- Se han llevado a cabo cálculos de modelo óptico para describir la sección eficaz (cuasi-)elástica medida. Con un potencial nuclear de volumen con una forma de Woods-Saxon se han reproducido los resultados encontrados en la literatura para el núcleo de carbono estable y bien ligado ^{12}C. A partir de este, variando las profundidades del potencial se consiguen ajustar los resultados del ^{15}C satisfactoriamente.

- La dispersión de ^{17}Ne conduce a resultados experimentales claros y directos, donde la sección eficaz elástica se caracteriza por la completa supresión de la interferencia Coulomb-nuclear. Fragmentos de carga Z=6-9 se encuentran en una proporción relevante, siendo la Z=8 (^{15}O) el canal dominante, el cual muestra dos componentes bien diferenciadas en su curva cinemática, probablemente debido a dos mecanismos de producción distintos (como la ruptura directa y la transferencia de dos protones al blanco, poblando estados excitados del ^{210}Po).

- La absorción encontrada en la dispersión en torno a la barrera de los isótopos estables del neón ^{22}Ne y ^{20}Ne se ha recreado con un potencial de superficie en el contexto de también un modelo óptico, simulando los efectos de la polarizabilidad Coulombiana. Este potencial necesita profundidades pequeñas y difusividades altas. Los patrones de interferencia se ajustan principalmente mediante las profundidades del potencial de volumen.

- Por el momento la publicación de estos resultados aguarda el desarrollo de cálculos más sofisticados de canales acoplados.

El estudio de reacciones nucleares inducidas por núcleos halo a energías en torno a la barrera de Coulomb ha mostrado ser una potente herramienta para entender el comportamiento dinámico de dichos núcleos. Tras el trabajo mostrado en esta tesis, parece claro que todavía es una línea de investigación que está llevando a nuevos e interesantes descubrimientos. No solo el progreso que supone en el conocimiento de nuestro universo sino también los avances tecnológicos que conlleva hacen que el futuro de la investigación básica en física nuclear sea prometedor.

Outlook

Despite having shed light on ^{15}C and ^{17}Ne structure through the study of their near-barrier scattering process, some questions remain still open about these exotic nuclear systems. In this section, a possible continuation of this research is presented, where the proposed experiments and upgrades are based on the results of this work.

The measurement of the ^{15}C scattering on ^{208}Pb at a near-barrier energy needs to be repeated with a higher beam intensity to get more conclusive evidences of its structure. An order of magnitude higher in the production of ^{15}C is still being claimed by the ISOLDE facility, so hopefully this new experiment will not have to wait long. The use of another stripping foil will help to increase the abundance ratio ^{15}C/^{15}N in the beam and, hence, reduce the importance of the channeling overlap between the elastic channels of ^{15}N and ^{15}C in the mass spectra. This possibility existed but it was not considered due to the extremely low ^{15}C intensity, which would be even further reduced with this extra stripper. Furthermore, with a total beam energy 5 MeV higher, being then slightly above the Coulomb barrier, reaction channels other than elastic are expected to take more importance and be easily observed.

A new compact vacuum chamber has already been designed and built to arrange the GLORIA detector inside, drastically reducing the pumping time needed in case it is necessary to open during the beam time. Inside, detectors can be placed 2 cm closer to the reaction target (from 6 cm to 4 cm), improving the solid angle coverage in such region by a factor $(6/4)^2 = 2.25$ at the cost of worsening the granularity to $\sim 4^\circ$, which is not so crucial. Since the straggling in ^{208}Pb is the main responsible of the experimental resolution, a thinner 1 mg/cm^2 target will allow for a clearer particle identification, but this lower density of scattering centers needs to be compensated with a high enough beam intensity. Monte Carlo simulations have already been done considering the new beam energy, target thickness and position of the side telescopes. Since the simulation does not take into account channeling effects and the achievable ^{15}C/^{15}N ratio is not known yet, equally abundant carbon and nitrogen have been supposed. The expected mass spectra and kinematic curve for the elastic channel of both nuclei (assuming Rutherford cross section) are shown in Fig. 9.1. The larger beam energy will make ^{15}N to punch through ΔE detectors in a wider angular range. With the side telescopes closer to the target and due to the divergence of the outgoing particles, the two most extreme strips on each side will need to be removed for the identification by coincidences between ΔE- and E- detectors. Their global mass spectra are a slightly wider because of the larger angular coverage, but a pixel by pixel or strip by strip analysis can always be performed. The use of silicon pads instead of DSSD as E-detectors will ease the electronic setup and will avoid the presence of dead strips in such stage of the telescopes.

In longer term and regarding the uncertainty in the theoretical calculations, it would be interesting to measure, on the same target and at the same energy, the scattering of ^{14}C, which would be the core of the ^{15}C halo system. This will make it possible to accurately obtain the parameters for the potential of the core-target interaction and, then, the difference with the ^{15}C cross section will exclusively be due to the effects of the neutron halo.

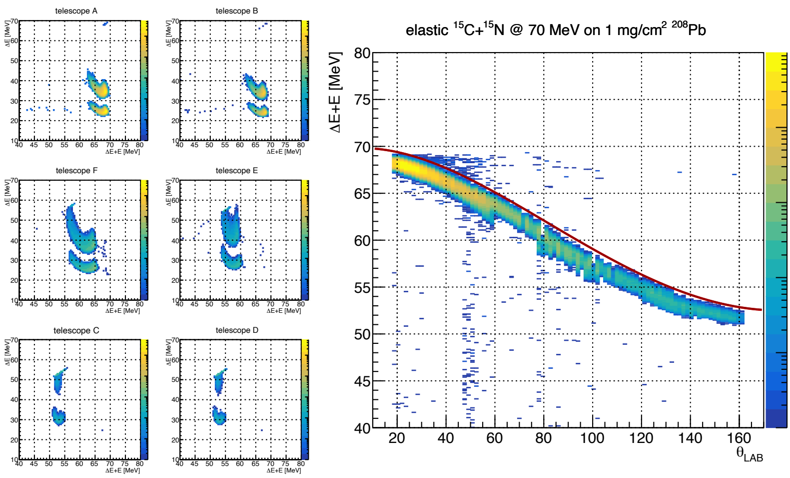

Figure 9.1: To the left: mass spectra of the six telescopes of the modified GLORIA detector for elastic ^{15}N and ^{15}C at E_{LAB} = 70 MeV on a 1 mg/cm^2 ^{208}Pb target. To the right: observed kinematic curve adding these telescopes.

On the other hand, the valence protons of ^{17}Ne are expected to occupy, in the ground state, a combination of $2s_{1/2}$ and $1d_{5/2}$ orbitals in a proportion yet unknown that has been ranged in an interval from 15% to 100% [70]. The reaction on ^{208}Pb analyzed in this thesis has concluded a strong two-proton transfer channel to the target, so it turned out to be mainly sensitive to the diproton component of the wave function. The still lack of consensus about the spectroscopic factors (SFs) could be solved by measuring the reaction ^{12}C(^{17}Ne,^{16}F)^{13}C at E$_{LAB}$ = 7.06 MeV/u in inverse kinematics. Preliminary DWBA calculations (see Fig. 9.2) predict a strong cross section for the stripping to ^{16}F, already observed in this work, so its decay from the three low-lying states will allow for a kinematical reconstruction of the proton angular distribution. Because of angular momentum conservation, if ^{17}Ne ground state has a pure $2s_{1/2}$ configuration, the proton stripping can only populate the pair of states 0^- (g.s.) and 1^- in ^{16}F. The same holds for the pair 2^- and 3^- in the case of a pure $1d_{5/2}$ configuration. In case of a mixture, the reproduction of the experimental angular distribution will unequivocally determine the strength of the SFs for ^{17}Ne ground state orbitals.

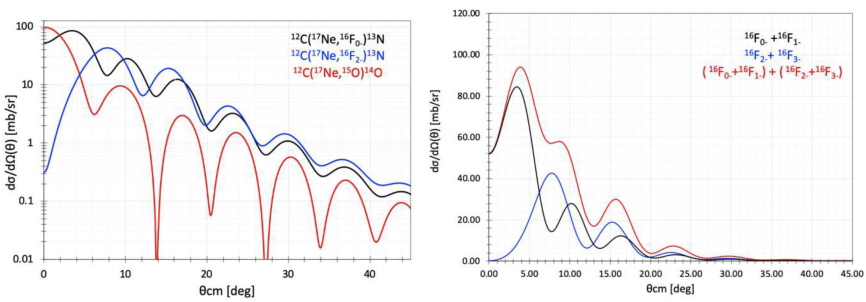

Figure 9.2: To the left: DWBA calculations for the ^{17}Ne stripping to ^{15}O (red), to ^{16}F ground state (black) and to ^{16}F first excited state (blue) at $E_{LAB} = 7.06$ MeV. To the right: same cross section assuming a pure $2s_{1/2}$ (black), pure $1d_{5/2}$ (blue) and a 50% mixture (red).

Bibliography

[1] I. Tanihata et al. Measurements of interaction cross sections and nuclear radii in the light p-shell region. *Physical Review Letters*, **55**(24):2676–2679, 1985.

[2] P. G. Hansen and B. Jonson. The neutron halo of extremely neutron-rich nuclei. *Europhysics Letters*, **4**(4):409–414, 1987.

[3] T. Kobayashi and O. Yamakawa. Projectile fragmentation of the extremely neutron-rich nucleus ^{11}Li at 0.79 GeV/nucleon. *Physical Review Letters*, **60**(25):2599–2602, June 1988.

[4] N. A. Orr et al. Momentum distributions of ^{9}Li fragments following the brealup of ^{11}Li. *Physical Review Letters*, **69**(14):2050–2053, October 1992.

[5] I. Mukha. Beta-decay studies of halo nuclei. *Nuclear Physics A*, 654:706–709, 1999.

[6] M. J. G. Borge et al. Elucidating halo structure by β decay: $\beta\gamma$ from the ^{11}Li decay. *Physical Review C*, 55(1):R8–11, 1997.

[7] B. Jonson. Light dripline nuclei. *Physics Reports*, 389:1–59, 2004.

[8] K. Riisager et al. First observation of beta-delayed deuteron emission. *Physics Letters B*, 235(1):30–34, 1990.

[9] M. J. G. Borge et al. Probing the ^{11}Li halo structure through β-decay into the ^{11}Be* (18 MeV) state. *Nuclear Physics A*, 613:199–208, 1997.

[10] M. V. Andrés and J. Gómez-Camacho. Dipole polarizability in the scattering of ^{11}Li below the Coulomb barrier. *Physical Review Letters*, **82**(7):1387–1390, February 1999.

[11] D. Escrig. *Estudio de reacciones de ^{6}He en Pb a energías próximas a la barrera coulombiana.* PhD thesis, IEM-CSIC, 2010.

[12] A. Sánchez-Benítez. *Estudio de la dispersión elástica de ^{6}He a energías en torno a la barrera de Coulomb.* PhD thesis, University of Huelva, 2005.

[13] L. Acosta. *Estudio de las reacciones inducidas por núcleos halo a energías cercanas a la barrera de Coulomb.* PhD thesis, University of Huelva, 2010.

[14] M. Cubero. *Estudio de la dispersión de ^{9}Li y ^{11}Li sobre un blanco de ^{208}Pb a energías en torno a la barrera coulombiana.* PhD thesis, IEM-CSIC, 2013.

[15] M. Cubero et al. Do halo nuclei follow Rutherford elastic scattering at energies below the barrier? The case of ^{11}Li. *Physical Review Letters*, 109(262701):1–5, 2012.

[16] G. Marquínez-Durán. *Near barrier scattering of ^{8}He from heavy targets.* PhD thesis, University of Huelva, 2016.

[17] G. Marquínez-Durán et al. Precise measurement of near-barrier ^{8}He+^{208}Pb elastic scattering: Comparison with ^{6}He. *Physical Review C*, 94(064618):1–5, 2016.

[18] V. Pesudo. *Analysis of the reaction of a one-neutron halo nucleus on a heavy target at energies around the Coulomb barrier: the case of ^{11}Be on ^{197}Au.* PhD thesis, IEM-CSIC, 2015.

[19] V. Pesudo et al. Scattering of the halo nucleus ^{11}Be on ^{197}Au at energies around the Coulomb barrier. *Physical Review Letters*, 118(152502):1–6, 2017.

[20] National Brookhaven Laboratory. National nuclear data center. `https://www.nndc.bnl.gov/`.

[21] A. Ozawa et al. Measurements of interaction cross sections for light neutron-rich nuclei at relativistic energies and determination of effective matter radii. *Nuclear Physics A*, **691**:599–617, 2001.

[22] A. Ozawa. Reaction cross-section for carbon isotopes. *Nuclear Physics A*, **738**:38–44, 2004.

[23] J. Terry et al. Absolute spectroscopic factors from neutron knock-out on the halo nucleus ^{15}C. *Physical Review C*, **69**(054306):1–5, 2004.

[24] N. Keeley and N. Alamanos. Single neutron transfer coupling effects on sub-barrier elastic scattering and near-barrier fusion of ^{15}C. *Physical Review C*, **75**(054610):1–6, 2007.

[25] R. Spartà et. al. Probing proton halo effects in the ^{8}b+^{64}zn collision around the Coulomb barrier. *Physics Letters B*, 820(136477), 2021.

[26] S. Viñals et al. The most accurate determination of the ^{8}B half-life. In *Acta Physica Polonica B*, volume 51, pages 717–723, 2020.

[27] A. Ozawa et al. Interaction cross sections and radii of the mass number A=17 isobar. *Physics Letters B*, **334**:18–22, August 1994.

[28] R. Kanungo et al. Possibility of a two-proton halo in ^{17}Ne. *Physics Letters B*, **571**:21–28, 2003.

[29] M. J. G. Borge et al. Beta-decay to the proton halo state in ^{17}F. *Physics Letters B*, **317**:25–30, 1993.

[30] N. K. Glendenning. *Direct Nuclear reactions.* Academic Press, Inc., 1983.

[31] H. Feshbach. The optical model and its justification. *Annu. Rev. Nucl. Sci*, 8:49–104, 1958.

[32] I. Thompson. Fresco - Coupled Reaction Channels Calculations. `http://www.fresco.org.uk/`, 2006.

[33] R. de Diego et al. Continuum-discretized coupled-channels calculations with core excitations. *Phys. Rev. C*, 89(064609), 2014.

[34] CERN webpage. ISOLDE facility. `https://isolde.cern/isolde-facility`.

[35] M. J. G. Borge. Highlights of the ISOLDE facility and the HIE-ISOLDE project. *Acta Physica Polonica B*, 47(3):591–605, 2016.

[36] SEC collaboration. Sec chamber. `https://isolde-sec.web.cern.ch/`.

[37] I. Martel et al. Effects of the neutron halo in ^{15}c scattering at energies around the coulomb barrier. *Proposal to the ISOLDE and Neutron Time-of-Flight Committee*, 2016.

[38] ISOLDE-CERN. Isolde yield database. `http://isoyields-classic.web.cern.ch/query_tgt.htm`.

[39] ACC. Villari. The accelerated ISOL technique and the SPIRAL project. *Nuclear Physics A*, 693:465–476, 2001.

[40] GANIL. Chart of beams. https://u.ganil-spiral2.eu/chartbeams/.

[41] G. Marquínez-Durán et al. GLORIA: A compact detector system for studying heavy ion reactions using radioactive beams. *Nuclear Instruments and Methods in Physics Research A*, 755:69–77, 2014.

[42] O. Tengblad et al. Novel thin window design for a large-area silicon strip detector. *Nuclear Instruments and Methods in Physics Research A*, 525:458–464, 2004.

[43] B. Löher and H. T. Törnqvist. Nustar Readout Library - Nurdlib. http://web-docs.gsi.de/~land/nurdlib/, 2017.

[44] N. Kurz and J. Adamczewski-Musch. GSI Data Acquisition System MBS Release Notes. https://www.gsi.de/en/work/research/experiment_electronics/data_processing/data_acquisition/mbs.htm.

[45] J. Adamczewski et al. Go4 on-line monitoring. *IEEE Transactions on Nuclear Science*, 51(3):565–570, 2004.

[46] O. Kirsebom. The Aarhus University Subatomic group library. https://git.kern.phys.au.dk/ausa/ausalib/wikis/home, 2016.

[47] H. T. Johansson. *The DAQ Always Runs*. PhD thesis, Chalmers University of Technology, 2006.

[48] Daresbury Multi Instance Data Acquisition System: MIDAS Documentation. http://npg.dl.ac.uk/MIDAS/.

[49] H. T. Johansson. The ucesb unpacker generator. http://fy.chalmers.se/~f96hajo/ucesb/ucesb_doc.pdf.

[50] S. Agostinelli et al. GEANT4 - a simulation toolkit. *Nuclear Instruments and Methods in Physics Research A*, 506(3):250–303, 2003.

[51] Two-body kinematics calculator. `http://skisickness.com/2010/04/relativistic-kinematics-calculator/`.

[52] D. Torresi et al. Influence of the interstrip gap on the response and the efficiency of Double Sided Silicon Strip Detectors. *Nuclear Instruments and Methods in Physics Research A*, (713):11–18, 2013.

[53] L. Grassi et al. Study of tghe inter-strip gap effects on the response of Double Sided Silicon Strip Detectors using proton micro-beams. *Nuclear Instruments and Methods in Physics Research A*, (767):99–111, 2014.

[54] J. A. Dueñas et al. Characterization of an NTD Double-Sided Silicon Strip Detector Employing a Pulsed Proton Microbeam. In *IEEE Transactions on nuclear science*, volume 64, pages 2551–2560, September 2017.

[55] A. Matta. *Study of the very neutron-rich* ^{10}He *by one-proton transfer reaction* $^{11}Li(d,^{3}He)$. PhD thesis, Université Paris-Sud, February 2012.

[56] J.P. Fernández-García. Simultaneous analysis of the elastic scattering and breakup channel for the reaction ^{11}Li+^{208}Pb at energies near the coulomb barrier. *Phys. Rev. C*, 92(044608), 2015.

[57] A. Barioni et al. Elastic scattering and total reaction cross sections for the ^{8}B, ^{7}Be and ^{6}Li+^{12}C systems. *Phys. Rev. C*, 84(014603), 2011.

[58] V. Morcelle et al. ^{8}B+^{27}Al scattering at low energies. *Phys. Rev. C*, 95(014615), 2017.

[59] Y. Yang et al. Elastic scattering of the proton drip-line nucleus ^{8}B off a ^{nat}Pb target at 180.3 MeV. *Phys. Rev. C*, 87(044613), 2013.

[60] Y. Yang et al. Elastic scattering of the proton drip line nuclei ^{7}Be, ^{8}B and ^{9}C on a lead target at energies around three times the coulomb barrier. *Phys. Rev. C*, 98(044608), 2018.

[61] K. Wang et al. Elastic scattering and breakup readctions of the proton drip-line nucleus ^{8}B on ^{208}Pb at 238 MeV. *Phys. Rev. C*, 103(024606), 2021.

[62] Y. Yang et al. Distinction between elastic scattering of weakly bound proton- and neutron-rich nuclei: the case of ^{8}B and ^{11}Be. *Phys. Rev. C*, 94(034614), 2016.

[63] M. Mazzocco et al. Elastic scattering for the ^{8}B and ^{7}Be+^{208}Pb systems at near-coulomb barrier energies. *Phys. Rev. C*, 100(024602), 2019.

[64] E. Gross et al. ^{20}Ne nuclear. moments from ^{20}Ne(131 MeV)+^{208}Pb scattering. *Phys. Rev. C*, 17(5):1665–1671, 1978.

[65] E. Gross et al. Nuclear moments of the first excited state of ^{22}Ne from ^{22}Ne(132 MeV)+^{208}Pb scattering. *Phys. Rev. C*, 29(2):459–463, 1984.

[66] A. Di Pietro et al. Elastic scattering and reaction mechanisms of the halo nucleus ^{11}Be around the Coulomb barrier. *Physical Review Letters*, 205(022701), 2010.

[67] S. Bottoni et al. Reaction dynamics and nuclear structure of moderately neutron-rich Ne isotopes by heavy-ion reactions. *Phys. Rev. C*, 85(064621), 2012.

[68] W. Love et al. Dynamic polarization potential for Coulomb excitation effects on heavy-ion scattering. *Physical Review Letters*, 39(1):6–8, 1977.

[69] S. Raman et al. *Atomic data and nuclear data tables*, volume 78. 2001.

[70] J. Marganiec et al. Coulomb and nuclear excitations of narrow resonances in ^{17}Ne. *Physics Letters B*, 759:200–205, 2016.

[71] S. Santra et al. Couples reaction channel analysis of elastic, inelastic, transfer and fusion cross sections for ^{12}C+^{208}Pb. *Phys. Rev. C*, 64(024602), 2001.

[72] EF. Aguilera et al. Systematics of reactions with ^{4,6}He: Static and dynamic halo effects and evidence for core-halo decoupling. *Phys. Rev. C*, 83(021601(R)), 2011.